

Backstepping control of H-L confinement transition in fusion plasma model

Master's thesis

Graduation project
ID 3NFA01

Student
T.J.A. Staps ²
ID 0676210

Supervisor
prof.dr. M.R. de Baar ^{1a/3b}

Mentors
dr. H.J. de Blank ^{2/3a}
dr.ir. F.A.A. Felici ^{1a}
prof.dr. H.J. Zwart ^{1b}

^{1a} CONTROL SYSTEMS TECHNOLOGY, ^{1b} DYNAMICS AND CONTROL
Department of Mechanical Engineering
University of Technology Eindhoven (TU/e)

² SCIENCE AND TECHNOLOGY OF NUCLEAR FUSION
Department of Applied Physics
University of Technology Eindhoven (TU/e)

^{3a} COMPUTATIONAL PLASMA PHYSICS, ^{3b} TOKAMAK PHYSICS
Department of Fusion Research
Dutch Institute for Fundamental Energy Research (DIFFER)

Eindhoven, February 10, 2017

Contents

1	Introduction	6
1.1	Nuclear fusion in a tokamak reactor	6
1.2	Plasma operation in the H-mode	6
1.3	Dynamics in the H-mode	7
1.4	Challenges for plasma edge control	7
1.5	Research objective	8
1.6	Methodology	9
2	Physics of the confinement transition and H-mode	10
2.1	Order of scales	10
2.2	Turbulence	11
2.2.1	Dynamics	11
2.2.2	Flow shear suppression of turbulence	12
2.3	Plasma momentum	12
2.4	Nonambipolar particle fluxes	13
2.5	L-H transition model	14
2.6	Radial electric field	16
2.6.1	Partial differential equation	16
2.6.2	Normalization	17
2.6.3	Coupling	18
2.6.4	Comparison	19
2.7	Hysteresis	21
2.8	Edge transport barrier	21
2.8.1	H-mode physics	21
2.8.2	Control of edge transport barrier	23
2.9	Discussion	23
3	Model analysis	24
3.1	Control problem	24
3.1.1	Objective	24
3.1.2	Physical context	25
3.2	Nonlinear p.d.e. system	26
3.2.1	Assumptions and definition	26
3.2.2	Nominal plant \mathcal{P}_1	28
3.3	Linear p.d.e. system	32
3.3.1	Linearization	32
3.3.2	Constraints	33
3.4	Reference p.d.e. system	35
3.4.1	State transformation	35
3.4.2	Constraints	36
3.5	Target p.d.e. system	38

3.5.1	Definition	38
3.5.2	Constraints	39
3.6	Discussion	39
4	Boundary control	42
4.1	Backstepping transformation	42
4.1.1	An elementary example	42
4.1.2	Description	44
4.1.3	Derivation	46
4.1.4	Formulation of the kernel p.d.e. system	47
4.2	Kernel p.d.e. system	49
4.2.1	Interpretation of the kernel conditions	49
4.2.2	Stability analysis of target system	51
4.3	Boundary feedback controller	56
4.3.1	Procedure for numerical solution	56
4.3.2	Solution of the kernel system	57
4.3.3	Feedback control law for the plasma model	60
4.4	Discussion	61
5	Conclusion and discussion	62
5.1	Conclusion	62
5.2	Discussion	64
Appendices		66
A	Nonambipolar particle fluxes	66
B	Linearization	73
C	Spatial derivatives of eigendecomposition	75
D	Characteristic o.d.e. for the kernel problem	77
E	First-order kernel problem	80
F	Numerical implementation of kernel problem	83

Preface

1982, the newly installed neutral beam injection system was used to push the ASDEX Upgrade tokamak into unknown territory. This allowed them to increase the performance and unraveled a new regime of operation. Their discovery is nowadays called the high confinement mode, which is achieved routinely at many tokamaks worldwide. Yet the physical mechanisms involved are still not completely known, but have proven to form a complex interplay. This has motivated many fusion scientists to develop models that describe these complex processes located in the small boundary layer of a tokamak plasma.

This study is inspired by one such model of Weymiens et al. [99], where the complex interplay of different processes is captured in a rather elegant model. Through the use of bifurcation analysis, a branch of mathematics that studies sudden transitions in system dynamics, the fusion community has gained increasing understanding of the macroscopic physics involved in the transition between the low and high confinement mode.

This study is also inspired by the control endeavour of van Gils et al. [81], whom studied the stabilization of unstable pool-boiling systems by actuating the boundary only. The analogy arises from the nonlinear behavior of boiling water, which involves an intermediate unstable boiling regime. Of course this provides a physical context and motivation to develop the control theory, but it also provides physicists the ability to conduct otherwise unattainable experiments.

A two-faced view on the plasma edge has been adopted at the beginning of this study. The idea to relate the model and well-known H-mode physics has originated from my urge to substantiate the credibility of the control-related work. This revealed the numerous assumptions and uncertainties underlying the transition and H-mode physics. Nevertheless it also proved the need to simplify the governing dynamics such that the essence is unraveled from the lengthy expressions and relations. Frequently I encountered that almost every simplification or assumption can be understood and substantiated by attaining the right physical viewpoint, i.e., talking to my fusion physics go to expert Hugo de Blank. Of course, the literature of the transition and H-mode physics have told me a lot, but it has been a pleasure to discuss the relevant and related physics from time to time. This provided me the ever important overview I needed to focus my physics-related endeavours.

Although the L-H transition model was already central to this study from the start, it was difficult to get started with the control design. There are not many courses that focus on p.d.e. control, while the use of o.d.e. methods are plentiful and well-developed. Through the fruitful talks with Federico Felici, I hope to have managed to really think through the control objective and approach. This allowed me to leave the physics and make the transition myself into the area of control.

Driven by stubbornness and the urge to learn new things, I still tried to force my way through the literature on p.d.e. control. There I got exposed to the motivation and promises of p.d.e. backstepping. A background in p.d.e. control and functional analysis are not required for the backstepping method as mentioned by Krstic and Smyshlyaev [57] in their book on boundary control of p.d.e.s. I beg to differ by saying this is indeed true, when one considers well-studied systems such as the heat equation, the wave equation or the beam model. However, a model originating from a physical application prescribes several limitations that do not always go well together with the method. This has proven to be painful at times. Luckily the meetings with Hans Zwart kept me on the right track or steered me back to it. Without all the over time discussions, I would not have gotten to solving the kernel problem.

The thesis in front of you would not have existed without the supervision of Marco de Baar. The

early analogy between the developments of the transition model and pool-boiling control planted the seed idea for this study during our first meeting. This inspired and showed me the absolute necessity of gaining more control on the heat flux out of the plasma. During the process of research, I gained lots of motivation and inspiration to keep on going, even when I realized that I would not be able to validate the control law in closed-loop before the project deadline.

The work on controlling the plasma edge should be continued as it entails an essential step to the ultimate goal of fusion power. I hope this work contributes to and inspires further endeavours of fellow fusion scientists, who will have the privilege of working with a team of true experts in the fields of fusion physics, plasma operation and control and p.d.e. control. This I can say from hands-on experience.

The short-hand notations listed in Table 1 could be useful for clarity of the abbreviations used throughout this thesis. Moreover, it should be noted that the abbreviations are used for both singular and plural nouns.

Table 1: List of abbreviations.

Abbreviation	Meaning
p.d.e.	partial differential equation(s)
o.d.e.	ordinary differential equation(s)
s.o.l.	scrape-off layer
d.o.f.	degree(s) of freedom
b.c.	boundary condition
m.h.d.	magnetohydrodynamics
e.l.m.	edge localized mode(s)
e.t.b.	edge transport barrier

Chapter 1

Introduction

1.1 Nuclear fusion in a tokamak reactor

Nuclear fusion is the process that powers the stars providing one of the conditions for life on earth. The gravitational pull pressurizes the sun, which holds an equilibrium at estimated temperatures $\sim 10^7$ [K]. Given the volume of the sun compared to its energy emitting surface, the conditions are sufficient to sustain fusion reactions for millions of years. The drawbacks of our present-day fuels cannot be sustained and motivate the development of alternative energy options. Nuclear fusion power is one sustainable alternative, for which a deuterium-tritium plasma yields the easiest fusion reaction:



Fusion research aims to gain understanding and control of fusion plasma, which should ultimately be self-sustained by fusion reactions (i.e., ignition). We owe the figure of merit for fusion power to Lawson, whom stated that the (triple) product of plasma density n , plasma temperature T and energy confinement time τ_E must be in excess of a critical value to reach ignition,

$$nT\tau_E \gtrsim 3 \cdot 10^{21} \left[\frac{\text{keV s}}{\text{m}^3} \right].$$

This means that the effective self-heating by 4He exceeds the power losses due to radiation, convection and conduction. Present-day fusion experiments do not meet the criterion and ignition is not yet achieved, although the tokamak reactor holds first-place of the triple product among the various confinement schemes.

Tokamak is actually an acronym, which means that fusion plasma is contained inside a torus-shaped vessel using magnetic coils. Through the induction of a plasma current, the magnetic field becomes helical and provides a stable macroscopic equilibrium. The closed magnetic field lines are diverted at the separatrix, where the magnetic field lines open up. Heat and particles flow across the separatrix into the scrape-off layer (s.o.l.), where the open magnetic field structure changes the plasma behavior considerably. The scrape-off layer connects the plasma edge to the divertor, which provides an exhaust for the plasma core. Below the ignition point, plasma temperature and density must be sustained by external heating and particle beams.

1.2 Plasma operation in the H-mode

A fusion plasma can be operated in the low and high confinement mode, which are abbreviated to L-mode and H-mode, respectively. The transition from low to high confinement occurs dynamically, when the heating power meets the (transition) power threshold. The H-mode was found by the ASDEX team [24], for the plasma was heated with sufficient heating power. Transport of particles and energy

is governed by turbulence. The turbulent transport increases initially in the L-mode, which lowers the energy confinement time,

$$\tau_E = \frac{U}{P_{\text{loss}}},$$

with plasma energy density U and power loss P_{loss} . When the heating power is increased further, the plasma makes the transition to H-mode.

The H-mode features improved energy and particle confinement, which is due to the suppression of turbulent transport at the plasma edge. The plasma edge is a thin boundary layer of the plasma, located just inside the separatrix. Reduced transport steepens the temperature and density gradient in the plasma edge, which is a thin boundary layer located on the plasma core side of the separatrix. This manifestation of the H-mode is called the edge transport barrier, which improves confinement of energy and particles across the plasma column. However, the significant temperature and density gradient at the plasma edge are prone to edge localized modes (e.l.m.) that may lead to an intermittent heat load ~ 1 [GW/m²] on the plasma-facing components (e.g., divertor). Due to the impact of such instabilities, there has been significant development within the area of edge localized modes (e.l.m.) control [21, 3, 75].

1.3 Dynamics in the H-mode

Suppression of turbulent transport in the H-mode is caused by a sheared plasma flow. The shear stress decorrelates small turbulent structures such that their energy is transferred to flows on a larger scale. Continuous turbulent suppression in the H-mode has been appointed to the radial electric field. The electric field induces an $\mathbf{E} \times \mathbf{B}$ -flow, the gradient of which determines the decorrelation (suppression) rate.

The mechanism that initiates the L-H transition is yet to be determined [43]. This has amounted to the development of many models aiming to describe the physics of the L-H transition. Recent studies on transition dynamics have developed a better understanding of the micro- and macroscopic physics [62][97]. The macroscopic dynamics should capture the interplay of density, temperature and radial electric field and their relation through turbulent dynamics. One such model has been subjected to a bifurcation analysis by Weymiers et al. [101], whom extended the original model of Zohm [28].

The extended plasma model of Zohm describes the edge of a fusion plasma, which includes a transport model and edge processes that generate the L-H and H-L bifurcations. This plasma model mimics the smooth, oscillatory and sharp transitions that are observed experimentally. A self-consistent description of the radial electric field allows to include the paradigm of flow shear suppression, which reduces the turbulence level. A simplified transport model describes the dynamics of plasma density and energy, the diffusivities of which depend on the turbulence level. This provides closure of the transition model, because the density and temperature gradient are partly responsible for the generation of radial currents.

1.4 Challenges for plasma edge control

The tokamak reactor faces the major challenge of demonstrating feasibility of fusion power [19]. One of the key engineering challenges is to cope with steady state ~ 10 [MW/m²] and intermittent heat fluxes up to $\sim 10^3$ [MW/m²] onto the divertor. The lifetime and reliability of the tokamak inner-vessel components are at risk for large heat loads, which scale with reactor size. Hence, the heat flux must be mitigated or reduced to ensure feasibility of the tokamak reactor.

H-mode operation enhances radiation due to the steepened edge gradient, which already lowers the heat flux across the separatrix. Furthermore, there have been developments to increase the effective divertor surface (e.g., snowflake configuration) and enhance the radiative flux (e.g., plasma detachment). However, the m.h.d. instability boundaries are part of the equation as well. Assessments of e.l.m. control shows that the frequency and size can be controlled [21], although the behavior of e.l.m. on future reactors is uncertain.

Another operational strategy can be defined on the basis of hysteresis. The sharp transitions exhibit hysteresis in the power threshold, which implies that the heat flux can be lowered after the H-mode is obtained. Therefore, the practical aim is to operate the plasma state¹ close to the H-L transition such that the heat flux across the separatrix is minimized. Meanwhile, the heating power must be sufficiently large such that the H-L transition is avoided. This constitutes a trade-off in the operational space of the plasma edge. Also, the operational space is tightened for future reactors, where cost reduction of the reactor requires small operational margins [104].

1.5 Research objective

Reactor-relevant plasma is preferably operated in the H-mode with adequate heat flux across the separatrix. This operational objective is addressed from a model-based perspective, where the idea is to apply control engineering to stabilize the plasma (model) state near the H-L bifurcation. Therefore, we use a model-based description of the L-H and H-L transition [99], which contains the main constituents of transition behavior and H-mode dynamics.

The research objective aims to *develop a feedback control for operation in the high confinement mode near the H-L bifurcation using standard actuating systems*. Despite important outstanding questions and uncertainties, we attempt to address the feasibility of stabilizing the plasma in H-mode close to the transition of H- to L-mode. This is complicated by inaccurate and noisy measurements due to the strong local variation of the plasma state. Due to the lack of sound measurements, we focus specifically on dealing with model uncertainty in this thesis. Therefore, the model nonlinearity² giving rise to the bifurcation behavior is investigated in light of its physical origin, which amounts to the first research question:

How does the radial electric field equation relate to the L-H/H-L confinement transition physics?

With a deepened understanding of the bifurcation behavior, the focus is shifted to identifying the model dynamics that exhibit hysteresis. Hysteresis is found sometimes experimentally in the power threshold, which allows a decrease of heating power after the transition. Owing to the bifurcation analyses of [32, 15, 99], it can be seen that the model also contains a hysteresis-like regime with sudden confinement transitions. Their results are exploited to study the model dynamics and frame the parameter space with respect to our purpose. Though their analyses have thoroughly explored the nonlinearity parameters, the other parameters are often unavailable to the reader. The investigation boils down to finding a model equilibrium that can be used for control design.

H-mode plasma operation is routinely achieved nowadays using plasma heating methods, which are available to most tokamak operators. After the L-H transition, the plasma state may be attracted to various modes that are termed L-, transient-, H- or quiescent H-mode, or even limit cycle oscillations (LCOs) [61]. There is intensive research on manipulating the edge plasma such that the operating space is broadened [6][39][46][54]. The difficulty of achieving the desired operating point resides in the fact that plasma state, dynamic topology and stability properties change dynamically. Also, the initial conditions and system trajectory are essential to the hysteresis behavior. As a consequence, the goal is to design a feedback control that stabilizes the plasma state near the H-L bifurcation. This constitutes the main idea behind the research question:

How close to the H-L bifurcation can the plasma model state be stabilized?

Any feedback controller for a tokamak necessarily includes observation of measurements of the plasma state. This often implies that the state has to be derived from diagnostic measurements using, e.g.,

¹For the plasma model considered, the plasma state represents the plasma temperature, density and radial electric field at a specific location in time and space within the plasma edge.

²The term model nonlinearity is used to denote the polynomial function $G(Z)$ in the radial electric field equation Z_t , which is introduced in Chapter 2.

spectroscopy, induction coils, probes and so forth. Furthermore, real measurements come with a certain spatio-temporal resolution and signal-to-noise ratio, which essentially produces a finite grid of disturbed measurements in space-time. Such observer or sensor dynamics should be included in the control design to examine feasibility of the controller properties. However, we limit the work in this thesis to the design of a feedback controller, where we assume that observations or measurements are available.

1.6 Methodology

The approach to assess the research objective describes the theory, methods and tools used throughout this thesis. The control goal is stabilization of the plasma model near the H-L bifurcation. The status quo of the L-H transition model invites further analysis of the physical origin of the bifurcation behavior.

Relevant parts of L-H transition and H-mode theory are explored in Chapter 2. The underlying processes that amount to the electric field bifurcation are sorted out and analyzed, which establishes a link between the plasma model nonlinearity and the theoretical background. Several model parameters gain a physical basis that among others relate to hysteresis and actuation inputs.

Examination of the underlying processes reveals that the parametric dependencies and model assumptions are plentiful. This insight is used in Chapter 3 to focus the control objective on model uncertainty. Hereafter, the nonlinear plasma model is analyzed to find a set of parameters that comply with the control goal. A linearization of the plasma edge model is used for p.d.e. control design. Not only does p.d.e. control facilitate the discussion between the physicist and the control engineer, it also allows to use physical insight into the desired system behavior.

We reason that the physical context at the plasma edge motivates the use of boundary feedback control, which is central to Chapter 4. Backstepping p.d.e. control is deployed for control design. This procedure formulates the design problem as an integral transformation that aims to map the plasma model into an equivalent system with desired dynamic behavior. As a result, a boundary feedback control manipulates the dynamic properties of the plasma model.

The intermediate results are discussed at the end of each chapter. Chapter 5 answers the research questions within the frame of validity of the results. We review the approach to, and results of, the physics- and control-related excercises and state the strengths and weaknesses thereof. Furthermore, we present ideas for future research on modeling and control of the plasma edge.

Chapter 2

Physics of the confinement transition and H-mode

This chapter reviews literature on the L-H/H-L transition and H-mode describing the relevant physics during and after a confinement transition. The spatio-temporal context of the L-H transition is clarified in § 2.1 to frame the context of the plasma model. § 2.2 treats plasma edge turbulence and its suppression in H-mode in view of this model. The interplay of plasma flow and radial electric field is examined in § 2.3 to understand the mechanism of $\mathbf{E}_r \times \mathbf{B}$ -flow shear suppression. This examination identifies the need to consider the radial electric field dynamics, the underlying processes of which are subject of § 2.4.

As it is an integral part of this study, the L-H transition model of Weymiens et al. [99] is described thoroughly in § 2.5. The plasma model enables us to mimic different types of L-H transitions, which are mainly expressed by various electric field bifurcations. We investigate the physical relation with the nonambipolar particle fluxes, which are analyzed in Appendix A, and thereof the electric field equation is derived in § 2.6. Hysteresis is discussed in more detail in § 2.7 in view of the model and physical understanding, because it is vital to the control objective. Hereafter, the edge transport barrier (e.t.b.) is discussed from an operational and control-related viewpoint in § 2.8. This chapter is concluded by a brief discussion of the results in § 2.9.

2.1 Order of scales

Processes in a fusion plasma occur on a wide variety of scales in space and time. On the largest length scale, the toroidal magnetic field \mathbf{B}_t and poloidal magnetic field \mathbf{B}_p (generated by the plasma current \mathbf{I}_p) are responsible for plasma confinement in a tokamak. A tokamak plasma establishes an equilibrium to the helical magnetic field, which can be described in radial \mathbf{e}_R , toroidal \mathbf{e}_t and vertical \mathbf{e}_z coordinates in the global coordinate system (depicted on the left of Figure 2.1). The magnetic field generates surfaces of constant magnetic flux, which are centred about a common magnetic axis. Plasma transport occurs along (parallel to) and across (perpendicular to) magnetic field lines, where cross-field transport is responsible for particle and energy loss. Fast parallel transport leads to nested surfaces with constant magnetic flux, temperature and density, which are centred about a common magnetic axis.

The transport problem contains a rotational (axi)symmetry in \mathbf{e}_t about the vertical axis \mathbf{e}_z . Hence, we may consider an arbitrary poloidal cross section, which is shown on the right of Figure 2.1. Magnetic flux surfaces normally assure that plasma variables vary in the radial direction \mathbf{e}_r only. Note, however, that this dimensional reduction only holds for plasma confined to closed magnetic field lines. Across the separatrix, the magnetic field lines open up to the divertor.

Anisotropic transport greatly simplifies the local description, which is deployed to study the transport bifurcation upon the transition from L- to H-mode. The transition dynamics are observable near the separatrix, but within the closed flux surfaces, due to changes in confined plasma transport. As a result, the transport problem can be further reduced to describe only a narrow boundary layer, i.e., $a \gg d$,

with a the plasma minor radius and d the boundary layer thickness. Hence, the toroidal geometry is condensed to a plasma slab due to negligible (geometric) curvature. Furthermore, the dimensionality can be reduced to only the radial direction \mathbf{e}_r (i.e., \mathbf{e}_x for slab coordinates), because it is assumed that the dynamics can be averaged over the poloidal direction \mathbf{e}_p .

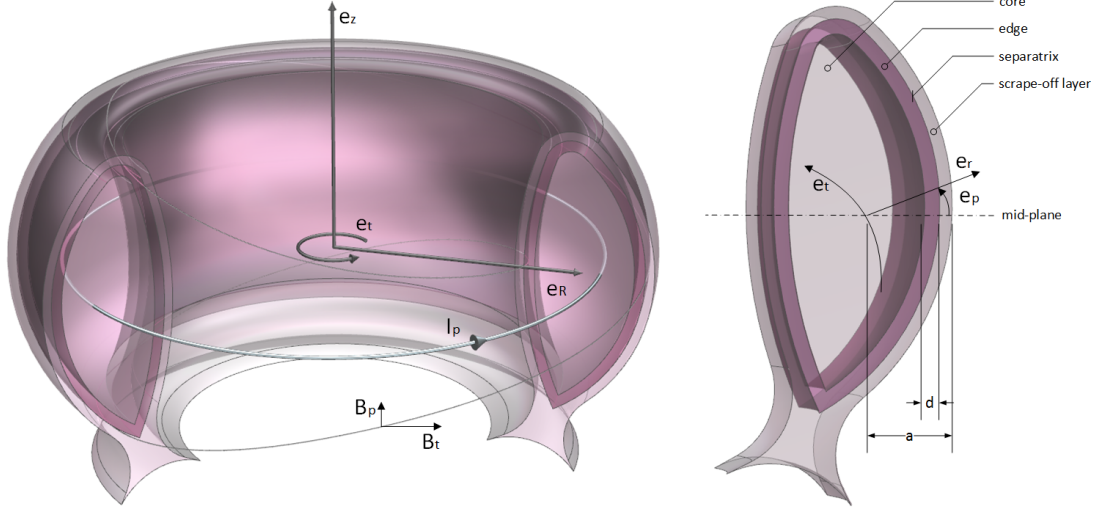


Figure 2.1: A tokamak plasma column with global coordinate system ($\mathbf{e}_R, \mathbf{e}_t, \mathbf{e}_z$) (left) and poloidal cross section with local coordinates ($\mathbf{e}_r, \mathbf{e}_p, \mathbf{e}_t$) (right).

Transport of magnetic flux, related to the plasma current density, is the slowest process within a tokamak plasma. Therefore, the magnetic field can be treated as a constant background field around the time of a transition. However, magnetic reconnection (e.g., sawtooth instabilities) occurs on a fast time-scale, but is not considered in this study. Across the frozen magnetic flux surfaces, temperature and density gradients extend radially from the core to the scrape-off layer.

Plasma density, temperature and momentum constitute the kinetic quantities in a thermonuclear experiment such as the tokamak. The pressure gradients drive turbulent modes, causing an anomalous cross-field transport of particles, energy and momentum. Changes of plasma transport occur much faster than changes in magnetic flux, but are still sufficiently slow for present-day control systems to be observed and regulated.

Changes in turbulence occur on the smallest of time scales. Turbulence is often inferred from fluctuations in density and electric field, of which the electric field varies on a similar time scale. The effect of electric field variations is felt immediately elsewhere in the plasma, which usually leads to shielding by plasma particles. At greater length scales, a toroidal electric field generates the Ohmic plasma current. A sheared radial electric field at the plasma edge induces a sheared flow across the flux surfaces, which leads to a reduction of turbulence in H-mode.

2.2 Turbulence

This section treats the dynamics of plasma turbulence in § 2.2.1 and the approach to model suppression in § 2.2.2.

2.2.1 Dynamics

Turbulent transport in a fusion plasma is mainly driven by the temperature and density gradients (of ions and electrons), which are amplified by increasing the input power. Contributing to the turbulent transport are various instabilities, of which the ion temperature gradient mode and trapped electron

mode are dominant in a collisionless plasma [102]. The micro-instabilities give rise to drift waves, because electrons neutralize fluctuations in finite time. Coupling of the drift waves to other plasma modes yields various types of drift-wave turbulence such as the drift resistive ballooning mode [10] or drift Alfvén turbulence [8].

Drift waves are the only type of turbulence able to drive a radial flux and thus, drift wave turbulence determines the level of edge turbulence and associated transport. As stressed by Scott et al. [9], the theory is yet to be further developed. Therefore, this study adopts a basic turbulence model used in [99]:

$$\frac{d\mathcal{E}}{dt} = \gamma_l \mathcal{E} - \alpha_{\text{sat}} \mathcal{E}^2, \quad (2.1)$$

with \mathcal{E} the turbulence level, γ_l the growth rate and α_{sat} the saturation rate. This turbulence model is described by an ordinary differential equation (o.d.e.), which contains a linear growth term (fluctuation instability) and a nonlinear saturation term (damping).

2.2.2 Flow shear suppression of turbulence

During past decades, many theories on the L-H transition have been developed from the perspective of stabilization or suppression of turbulence [38]. Although stabilization of a turbulent mode may occur, the present consensus states that turbulent edge transport is rather suppressed by a radial shear in plasma flow [76]. A radial shear in plasma flow decorrelates turbulent eddies, which are small structures compared to the flow length scale. As eddies are extended by the sheared plasma flow, their wave energy is transferred to larger flow structures at the expense of small turbulent structures. Although this paradigm is supported by experimental evidence, it is not yet fully understood how the plasma flow shear (2.2) is initially generated.

$$\frac{\partial V_{\mathbf{E} \times \mathbf{B}}}{\partial x} = \frac{\partial(E_r/B)}{\partial x} \approx \frac{1}{B_t} \frac{\partial E_r}{\partial x} \quad (2.2)$$

Recent modelling efforts have shown that both zonal $\mathbf{E} \times \mathbf{B}$ flow and mean $\mathbf{E} \times \mathbf{B}$ flow are involved in the transition dynamics [72], a picture supported by experimental evidence [25][105]. Zonal flows are produced by the shear of Reynolds stress arising from correlated radial and poloidal fluctuations. The zonal flow shear suppresses the drift-wave turbulence, but the mechanism is damped by ion-ion collisions or flow instabilities [71]. Hence, zonal flows provide a temporary sink of energy, which show their signature already before the L-H transition. At present, the role of zonal flows in the L-H transition is widely accepted [72].

The mean $\mathbf{E} \times \mathbf{B}$ flow remains in the H-mode, while the zonal $\mathbf{E} \times \mathbf{B}$ flow vanishes. Shear flow suppression of turbulence has been modeled by many authors such as [95]. This led to the paradigm that the sheared flow amplifies the saturation mechanism in H-mode, which is called the nonlinear suppression model in [99]:

$$\frac{d\mathcal{E}}{dt} = \gamma_l \mathcal{E} - \alpha_{\text{sup}} \left(1 + \alpha_{\text{sup}} \left(\frac{\partial Z}{\partial x} \right)^2 \right) \mathcal{E}^2, \quad (2.3)$$

with the suppression rate coefficient α_{sup} and the normalized radial electric field Z , the introduction of which is delayed until § 2.5. Note that two different suppression models have been analyzed in [99]. One model includes the reduction of linear growth rate γ_l by the radial electric field shear, while the flow shear in the nonlinear (turbulence) model results in additional suppression on top of the self-induced saturation $\alpha_{\text{sat}} \mathcal{E}^2$. The nonlinear suppression model (2.3) is used throughout this thesis, because it is most robust to parameter changes [101].

2.3 Plasma momentum

Plasma flow may consists of components in the $\mathbf{E} \times \mathbf{B}$, diamagnetic, poloidal and toroidal direction and reduces to an intrinsic rotation without external input [33]. Any plasma flow carries momentum, which

is driven, damped and transported by various processes [40]. Internal drivers of momentum are the nonambipolar fluxes (due to, e.g. pressure gradient or ion orbit losses), while an external momentum input can be, for example, neutral beam injection (NBI). Viscous stress damps the plasma flow across flux surfaces, but also charge exchange friction with neutrals at the edge adds to the damping.

Momentum is a conserved state variables that can be transported across flux surfaces to add a radial component to the plasma current. In steady state, the radial ion force balance [103] can be written as

$$E_r = \frac{1}{n_i q_i} \nabla p_i + v_t B_p - v_p B_t, \quad (2.4)$$

with E_r the radial electric field, $n_i q_i$ ion charge density, p_i ion pressure, $v_{t,p}$ toroidal or poloidal ion flow velocity and $B_{t,p}$ toroidal or poloidal magnetic field. Often, the radial electric field is determined experimentally by measuring the three contributions separately. The poloidal and toroidal flow velocity can be measured using, for example, spectroscopy on a radiating impurity assuming it represents the plasma flow velocity. The pressure gradient can be measured from density and temperature measurements, but the error is amplified near the edge due to steep gradients. Hence, it is difficult to determine the radial electric field accurately during experiments. This motivates at least partially the development of edge diagnostics with higher accuracy and better resolution.

Another approach to determine the radial electric field requires knowledge of the particle fluxes across magnetic flux surfaces. The radial particle fluxes from mechanisms driving, damping and transporting momentum can be classified as ambipolar and nonambipolar. Ambipolar particle fluxes are equal for electrons and ions and hence, result in zero radial current. By contrast, nonambipolar particle fluxes Γ^{na} are different for various plasma species and may violate the ambipolarity constraint (2.5) [34]. As a result, the radial electric field generates a return current such that the (flux surface-averaged) divergence of the plasma current vanishes again.

$$\langle \mathbf{J} \cdot \nabla \rho \rangle = \sum_s q_s \Gamma_s^{\text{na}} = 0 \quad (2.5)$$

Nonambipolar particle fluxes thus depend on the radial electric field such that their interplay must be considered self-consistently. Furthermore, nonambipolar particle fluxes are also generated by kinetic (e.g. ion orbit loss) and atomic processes (neutral-plasma interaction) in addition to the aforementioned fluid picture. We follow the approach of many L-H transition theories [38] by focusing on a self-consistent description of the radial electric field and nonambipolar particle fluxes.

2.4 Nonambipolar particle fluxes

Nonambipolar particle fluxes have been derived by Callen [33] in a framework that relates the plasma momentum to the radial electric field. However, this framework considers the plasma momentum and radial electric field for the bulk plasma, where boundary effects do not play a role per se. Therefore, the total nonambipolar particle flux Γ^{na} (2.6) is split into contributions from volumetric, Γ_V^{na} , and edge, Γ_E^{na} , processes.

$$\Gamma^{\text{na}} := \Gamma_V^{\text{na}} + \Gamma_E^{\text{na}} \quad (2.6)$$

The volumetric components also play a role at the plasma edge, whereas the edge contributions are limited to that region (due to their physical nature). The volumetric components can be found in [33], which are summed to yield the nonambipolar volumetric particle flux,

$$\Gamma_V^{\text{na}} = \frac{\Gamma^{\pi\parallel}_{\text{bulk}}}{\text{viscosity}} + \frac{\Gamma^{\pi\perp}_{\text{viscosity}}}{\text{viscosity}} + \frac{\Gamma^{\text{pol}}_{\text{polarization}}}{\text{stress}} + \frac{\Gamma^{\text{Rey}}_{\text{Reynolds}}}{\text{stress}} + \frac{\Gamma^{\text{Max}}_{\text{Maxwell}}}{\text{stress}} + \frac{\Gamma^{\mathbf{J} \times \mathbf{B}}_{\text{resonant magn.}}}{\text{perturbations}} + \frac{\Gamma^{\dot{\psi}_p}_{\text{poloidal flux}}}{\text{transient}} + \frac{\Gamma^S_{\text{external source(s)}}}{\text{source(s)}}, \quad (2.7)$$

with superscripts indicating a radial particle flux: $\Gamma^{\pi\parallel,\pi\perp}$ from viscous torque (parallel and perpendicular to a flux surface), Γ^{pol} from plasma polarization, $\Gamma^{\text{Rey},\text{Max}}$ from fluctuation-induced Reynolds and

Maxwell stress, $\Gamma^{\mathbf{J} \times \mathbf{B}}$ non-axisymmetric resonant magnetic perturbations, Γ^{ψ_p} from momentum transport due to poloidal flux transients and Γ^S from external momentum sources and sinks. Gyroviscosity (viscosity in diamagnetic direction) is not taken into account, since its particle flux is negligible in a tokamak [74]. Also, the fluctuation-induced stresses, Reynolds and Maxwell stress, are left out, because we consider (averaged) plasma state variables in the model. Furthermore, the poloidal flux transient is neglected, because the magnetic field is assumed quasi-stationary around the transition time. The effect of neutral beam injection, (axisymmetric) resonant magnetic perturbations or electron cyclotron heating may be added to the equation via the external source term. Hence, control inputs can be captured in the external source term Γ^S , whereas the particle flux caused by non-axisymmetric resonant magnetic perturbations goes into $\Gamma^{\mathbf{J} \times \mathbf{B}}$.

At the plasma edge, nonambipolar processes can be active due to the transition of closed to open magnetic field lines, the finite number of coils or atomic processes due to the presence of neutral particles. The edge processes are captured in the nonambipolar edge particle flux,

$$\Gamma_E^{\text{na}} = \frac{\Gamma^{\text{an}}}{\text{anomalous diffusion}} + \frac{\Gamma^{\text{ol}}}{\text{orbit loss}} + \frac{\Gamma^{\text{cx}}}{\text{charge exchange}} + \frac{\Gamma^{\text{rl}}}{\text{ripple loss}}, \quad (2.8)$$

with superscripts indicating a radial particle flux: Γ^{an} from anomalous cross-field diffusion (due to drift-waves), Γ^{ol} from direct orbit loss (ion versus electron Larmor radius), Γ^{cx} from charge exchange friction with neutral particles and Γ^{rl} from ripple losses due to magnetic field inhomogeneities. The effect of ripple losses is left out of further discussion, because we assume a low collisionality ($T_{\text{ped}} \sim 1$ [keV]). The physical background of the relevant nonambipolar particle fluxes contained in equation (2.7) and (2.8) can be found in Appendix A, including their physical background and expression in terms of plasma parameters and variables. Eliminating the nonambipolar particle fluxes that are not considered in this thesis leads to the definition of the total nonambipolar particle flux,

$$\Gamma^{\text{na}} = \Gamma^{\pi\parallel} + \Gamma^{\pi\perp} + \Gamma^{\text{pol}} + \Gamma^{\text{an}} + \Gamma^{\text{ol}} + \Gamma^{\text{cx}}. \quad (2.9)$$

Using the ambipolarity condition (2.5), the self-consistent dynamics of the radial electric field can be derived from the total nonambipolar particle flux (2.9). The next section § 2.5 describes the plasma model that is central to this thesis, which includes such a self-consistent description of the radial electric field. However, we revisit the nonambipolar particle fluxes to investigate the origin of the partial differential equation (p.d.e.) for the radial electric field in § 2.6.

2.5 L-H transition model

This section describes the L-H transition model introduced in [99, §5.2], which is an adapted version of the original model of Zohm [28]. The partial differential equations, boundary conditions and functional relations are restated to clarify our use of the model. This is because various modeling choices have been explored for bifurcation analysis by [99, 85, 15].

Plasma transport is modeled by conservation of mass ($\sim n$) and energy ($\sim nT$) leading to p.d.e. for plasma density n (2.10) and plasma energy U (2.11). The transport equations are considered in a slab geometry, with spatial coordinate x and time t ,

$$\frac{\partial n}{\partial t} = \frac{\partial}{\partial x} \left(D(\mathcal{E}) \frac{\partial n}{\partial x} \right) \quad (2.10)$$

$$\frac{\partial U}{\partial t} = \frac{\partial}{\partial x} \left(\chi(\mathcal{E}) n \frac{\partial T}{\partial x} + \frac{D(\mathcal{E}) T}{\gamma - 1} \frac{\partial n}{\partial x} \right) \quad (2.11)$$

with particle and heat diffusivities $D(\mathcal{E})$ and $\chi(\mathcal{E})$, respectively, and γ the ratio of ion-electron heat capacity (i.e., adiabatic index). Note that the diffusivities are functions of the turbulence level \mathcal{E} (2.3). The particle and heat diffusivity functions are simplified in [15, 99] due to the belief that different

diffusivities do not alter the bifurcation behavior qualitatively. We adopt the same simplification for our purpose:

$$\chi = \frac{D}{\zeta(\gamma - 1)}, \quad (2.12)$$

which introduces an additional parameter ζ to adapt the ratio between χ and D . Moreover, it is assumed that the particle diffusivity scales linearly to the turbulence level \mathcal{E} [99, §5.2],

$$D(\mathcal{E}) = D_{\min} + (D_{\max} - D_{\min}) \frac{\mathcal{E}}{\mathcal{E}_{\max}}, \quad (2.13)$$

with the lower limit D_{\min} , maximum diffusivity D_{\max} and $\mathcal{E}_{\max} = \gamma_1 \alpha_{\text{sat}}^{-1}$, the maximum turbulence level. The anomalous particle diffusivity $D(\mathcal{E})$ (2.13) includes both neoclassical and turbulent transport contributions.

The plasma energy p.d.e. contains two states in the time derivative, which is inconvenient for control analysis and design. Hence, (2.11) is rephrased using the definition of plasma energy,

$$U = \frac{nT}{\gamma - 1}, \quad (2.14)$$

such that only the temperature time derivative remains in (2.11). Therefore, we introduce (2.14) and the simplified expression for χ (2.12) such that (2.11) gives us

$$n \frac{\partial T}{\partial t} + T \frac{\partial n}{\partial t} = \frac{\partial}{\partial x} \left(\frac{D(\mathcal{E}) n}{\zeta} \frac{\partial T}{\partial x} \right) + T \frac{\partial}{\partial x} \left(D(\mathcal{E}) \frac{\partial n}{\partial x} \right) + D(\mathcal{E}) \frac{\partial n}{\partial x} \frac{\partial T}{\partial x}, \quad (2.15)$$

from which the density p.d.e. (2.10) can be subtracted to yield a p.d.e. involving plasma temperature only:

$$\frac{\partial T}{\partial t} = \frac{\partial}{\partial x} \left(\frac{D(\mathcal{E})}{\zeta} \frac{\partial T}{\partial x} \right) + \left(\frac{\zeta + 1}{\zeta} \right) \frac{D(\mathcal{E})}{n} \frac{\partial n}{\partial x} \frac{\partial T}{\partial x}. \quad (2.16)$$

The radial electric field p.d.e. (2.17) contains radial currents due to polarization and shear viscosity explicitly. The other nonambipolar processes are partly affected by the density and temperature gradient (i.e., thermodynamic forces), which couples the respective differential equations. The cubic polynomial function $G(Z)$ approximates the remaining electric field-induced (Z) contributions, which has an inflection point in Z -space denoted by Z_S . Hence, the radial currents form a partial differential equation for the radial electric field [99]:

$$\varepsilon \frac{\partial Z}{\partial t} = \mu \frac{\partial^2 Z}{\partial x^2} + \frac{c_n T}{n^2} \frac{\partial n}{\partial x} + \frac{c_T}{n} \frac{\partial T}{\partial x} + G(Z), \quad (2.17)$$

where Z denotes the normalized electric field obtained through the normalization of E_r with respect to space (ion Larmor radius ρ_{pi}) and energy (temperature T):

$$Z = \frac{\rho_{pi} e E_r}{T} \text{ with } \rho_{pi} = \frac{m_i v_{ti}}{e B_p} \quad (2.18)$$

It can be seen that (2.17) is not only nonlinear in Z , but also includes a nonlinear coupling through the density and temperature gradient.

The set of partial differential equations describe the plasma edge dynamics on the domain Ω ,

$$\Omega = \{(x, t) \in \mathbb{R}^2 \mid (0 \leq x \leq L) \wedge (t \geq 0)\} \quad (2.19)$$

with boundary conditions of the Robin-type at the separatrix (or scrape-off layer side of the domain), for $x = 0$:

$$\left. \frac{\partial n}{\partial x} \right|_{x=0} = \frac{n}{\lambda_n}, \quad \left. \frac{\partial T}{\partial x} \right|_{x=0} = \frac{T}{\lambda_T}, \quad \left. \frac{\partial Z}{\partial x} \right|_{x=0} = \frac{Z}{\lambda_Z}. \quad (2.20)$$

The scrape-off layer (s.o.l.) boundary conditions force the plasma variables to zero along a typical length scale λ . The Neumann-type boundary conditions at the plasma core (side of the domain) are given in terms of the particle and heat fluxes at $x = L$, while the radial electric field shear vanishes,

$$-\left[D(\mathcal{E})\frac{\partial n}{\partial x}\right]_{x=L} = \Gamma_c, \quad -\left[\frac{D(\mathcal{E})}{\zeta}\frac{\partial T}{\partial x}\right]_{x=L} = \left[\frac{(\gamma-1)q_c - T\Gamma_c}{n}\right]_{x=L}, \quad \left[\frac{\partial Z}{\partial x}\right]_{x=L} = 0. \quad (2.21)$$

So, the (negative) fluxes flow towards the scrape-off layer, at $x = 0$, for (positive) gradients that increase towards the plasma core, at $x = L$.

The model shows qualitatively different transitions that are smooth, sharp or oscillatory depending on the coefficients of the polynomial function:

$$G(Z) = a + b(Z - Z_S) + c(Z - Z_S)^3, \quad (2.22)$$

with a, b and c polynomial coefficients and Z_S the inflection point of the polynome. Especially, the sharp and oscillatory transitions are often observed in experimental discharges, the transitions of which may exhibit an hysteresis. Hysteresis is expressed in the model by a different heat flux threshold for the L-H and H-L bifurcation, which is equivalent to its experimental manifestation.

The nonambipolar particle fluxes described in § 2.4 are used to derive a physics-based p.d.e. for the radial electric field in the next section. This is to deepen our understanding of the relation between model parameters and physical parameters. Also, the aim is to see how the hysteresis is affected by the plasma variables and parameters.

2.6 Radial electric field

The partial differential equation (2.17) for the normalized electric field (Z) of the L-H transition model is derived from Ampère's law in § 2.6.1, whereafter we apply a normalization in § 2.6.2 to E_r such that the physics-based p.d.e. is also defined in terms of Z . Relevant nonambipolar particle fluxes that are outlined throughout Appendices A.2–A.9 are used to introduce the physical processes into the equation. Hereafter, our derivation and the model p.d.e. are compared in § 2.6.4 to conclude on its physical background and its use to manipulate the hysteresis.

2.6.1 Partial differential equation

We start the derivation of the radial electric field p.d.e. by Ampère's law with Maxwell's displacement (2.23). The rate of change of the electric field (displacement current) is related to the electric current (charged particle fluxes) as

$$\nabla \times \mathbf{B} = \mu_0 \mathbf{J} + \mu_0 \varepsilon_0 \frac{\partial \mathbf{E}}{\partial t}, \quad (2.23)$$

with the magnetic field \mathbf{B} , plasma current \mathbf{J} and electric field \mathbf{E} . Taking the inner product with the radial component of the gradient operator, ∇_r , the curl of the magnetic field vanishes. This is because the curl of any vector field is divergence-free,

$$\nabla_r \cdot (\nabla \times \mathbf{B}) = \nabla \cdot (\mathbf{B} \times \nabla_r) = -\nabla \cdot (\nabla_r \times \mathbf{B}) = 0, \quad (2.24)$$

which also reveals that the divergence of the (radial) plasma and displacement current must vanish. Hence, we obtain an equation for the radial electric field and radial current,

$$\varepsilon_0 \frac{\partial E_r}{\partial t} = -J_r = \sum_k (q_{e,i} \Gamma_{e,i}^k), \quad (2.25)$$

where the radial current is composed from various nonambipolar currents $q_{e,i} \Gamma_{e,i}^k$ due to some nonambipolar process k . We assume an ion-electron plasma such that $q_{e,i} = \pm e$ depending on the dominant

species for each process, of which a brief explanation and corresponding expression can be found in Appendix A. Substituting the various processes (2.9) into (2.25) yields a partial differential equation for the radial electric field,

$$\varepsilon_0 \frac{\partial E_r}{\partial t} = - \frac{e\Gamma_i^{\pi\parallel}}{\text{bulk viscosity}} + \frac{\partial}{\partial x} \left(\frac{m_i n_i \mu_i}{B_p^2} \frac{\partial E_r}{\partial x} \right) - \frac{m_i n_i}{B^2} \frac{\partial E_r}{\partial t} + \frac{e\Gamma_e^{\text{an}}}{\text{shear viscosity}} - \frac{e\Gamma_i^{\text{ol}}}{\text{polarization}} - \frac{e\Gamma_i^{\text{cx}}}{\text{anomalous diffusion}} - \frac{e\Gamma_i^{\text{ol}}}{\text{orbit loss}} - \frac{e\Gamma_i^{\text{cx}}}{\text{charge exchange}}, \quad (2.26)$$

where the polarization current is replaced by equation (A.11) (see Appendix A.2) and the shear viscosity by equation (A.16) (see Appendix § A.3). Rearranging the terms and adding the polarization current to the displacement current yields

$$\varepsilon_0 \left(1 + \frac{m_i n_i}{\varepsilon_0 B^2} \right) \frac{\partial E_r}{\partial t} = \frac{\partial}{\partial x} \left(\frac{m_i n_i \mu_i}{B_p^2} \frac{\partial E_r}{\partial x} \right) + e \left(-\Gamma_i^{\pi\parallel} + \Gamma_e^{\text{an}} - \Gamma_i^{\text{ol}} - \Gamma_i^{\text{cx}} \right). \quad (2.27)$$

The pre-factor of the time derivative in (2.27) can be rewritten in terms of the Alfvén velocity, v_A :

$$\varepsilon_0 \left(1 + \frac{m_i n_i}{\varepsilon_0 B^2} \right) = \varepsilon_0 \left(1 + \frac{m_i n_i c_0^2 \mu_0}{B^2} \right) = \varepsilon_0 \left(1 + \frac{c_0^2}{v_A^2} \right), \quad v_A \approx \frac{B}{\sqrt{\mu_0 m_i n_i}}. \quad (2.28)$$

It is safe to assume that $v_A \ll c_0$ at the plasma edge, because $n \sim 10^{19}$ and we consider the low-field side of the tokamak for our case (§ A.1) such that $c_0^2 v_A^{-2} \sim 10^2$. Therefore, the partial differential equation can be simplified to

$$m_i n_i \left(\frac{B_p}{B} \right)^2 \frac{\partial E_r}{\partial t} = m_i n_i \mu_i \frac{\partial^2 E_r}{\partial x^2} + e B_p^2 \left(-\Gamma_i^{\pi\parallel} + \Gamma_e^{\text{an}} - \Gamma_i^{\text{ol}} - \Gamma_i^{\text{cx}} \right). \quad (2.29)$$

For the purpose of derivation and model comparison, we assume a constant viscosity coefficient such that $m_i n_i \mu_i$ can be excluded from the partial derivative. The radial electric field p.d.e. (2.29) is normalized in the next section § 2.6.2 to proceed the derivation.

2.6.2 Normalization

The radial electric field p.d.e. (2.29) is normalized to the ion temperature and ion Larmor radius using the normalization (2.18), i.e., $Z = \rho_{pi} e E_r T_i^{-1}$. For brevity, we use the term ‘electric field’ from here on to refer to the normalized radial component of the electric field. The time derivative of the electric field Z simply becomes

$$\frac{\partial Z}{\partial t} = \frac{\rho_{pi} e}{T_i} \frac{\partial E_r}{\partial t} + \frac{e E_r}{T_i} \frac{\partial \rho_{pi}}{\partial t} + \rho_{pi} e E_r \frac{\partial (T_i)^{-1}}{\partial t} \approx \frac{\rho_{pi} e}{T_i} \frac{\partial E_r}{\partial t}, \quad (2.30)$$

where the rate of change of the electric field is assumed large around the L-H transition, while the temperature (and density) time derivatives are approximately constant. This is especially true when the sharp or oscillatory transitions are considered. However, the electric field curvature is more involved because of the temperature dependence of the electric field, which is not necessarily smaller than the second spatial derivative of temperature,

$$\begin{aligned} \frac{\partial^2 Z}{\partial x^2} &= e \left(\frac{\rho_{pi}}{T_i} \frac{\partial^2 E_r}{\partial x^2} + \frac{E_r}{T_i} \frac{\partial^2 \rho_{pi}}{\partial x^2} + \rho_{pi} E_r \frac{\partial^2 (T_i)^{-1}}{\partial x^2} \right) \\ &= e \left(\frac{\rho_{pi}}{T_i} \frac{\partial^2 E_r}{\partial x^2} + \frac{E_r}{T_i} \frac{m_i}{e B_p} \sqrt{\frac{2e}{m_i}} \frac{\partial^2}{\partial x^2} (T_i)^{1/2} + \rho_{pi} E_r \frac{\partial^2}{\partial x^2} (T_i)^{-1} \right) \end{aligned} \quad (2.31)$$

where it is assumed that the ion shear viscosity coefficient μ_i is constant. So, the curvature of the radial electric field E_r multiplied by the normalization factor can be expressed in terms of the electric field Z

and the ion temperature T_i ,

$$\begin{aligned} \frac{\rho_{pi}e}{T_i} \frac{\partial^2 E_r}{\partial x^2} &= \frac{\partial^2 Z}{\partial x^2} - \sqrt{2em_i} \frac{E_r}{B_p T_i} \frac{\partial^2}{\partial x^2} (T_i)^{1/2} - \rho_{pi}e E_r \frac{\partial^2}{\partial x^2} (T_i)^{-1} \\ &= \frac{\partial^2 Z}{\partial x^2} - \left(\sqrt{\frac{m_i}{2eT_i}} \frac{Z}{\rho_{pi}B_p} - \frac{Z}{T_i} \right) \frac{\partial^2 T_i}{\partial x^2} + \frac{1}{2T_i} \left(\sqrt{\frac{m_i}{2eT_i}} \frac{Z}{\rho_{pi}B_p} - \frac{4Z}{T_i} \right) \left(\frac{\partial T_i}{\partial x} \right)^2 \\ &= \frac{\partial^2 Z}{\partial x^2} + \left(\frac{Z}{2T_i} \right) \frac{\partial^2 T_i}{\partial x^2} - \left(\frac{7Z}{4T_i^2} \right) \left(\frac{\partial T_i}{\partial x} \right)^2 \approx \frac{\partial^2 Z}{\partial x^2} \end{aligned} \quad (2.32)$$

where in the forelast step, the ion Larmor radius ρ_{pi} and ion thermal speed v_{ti} have been used such that

$$\sqrt{\frac{m_i}{2eT_i}} \frac{1}{\rho_{pi}B_p} = \frac{1}{2T_i} \quad \text{with} \quad \rho_{pi} = \frac{m_i v_{ti}}{eB_p}, \quad v_{ti} = \sqrt{\frac{2eT_i}{m_i}}. \quad (2.33)$$

As for example in [83], the dependence of the electric field derivatives on the temperature derivatives is neglected. In fact, in most papers, the authors do not spend much attention on the details of the normalization procedure. We follow a similar approach by assuming $T_x \approx T_{xx} \approx 0$ such that the temperature dependent terms can be neglected in (2.30) and (2.32), again for the purpose of comparison and conciseness.

Substituting the time derivative (2.30) and curvature (2.32) of the electric field into (2.29) yields its partial differential equation (2.34).

$$\frac{m_i n_i T_i}{e \rho_{pi}} \left(\frac{B_p}{B} \right)^2 \frac{\partial Z}{\partial t} = \frac{m_i n_i \mu_i T_i}{e \rho_{pi}} \frac{\partial^2 Z}{\partial x^2} + e B_p^2 \left(-\Gamma_i^{\pi\parallel} + \Gamma_e^{\text{an}} - \Gamma_i^{\text{ol}} - \Gamma_i^{\text{cx}} \right), \quad (2.34)$$

Note that in the L-H transition model described in § 2.5, it is also assumed that the effect of $\frac{\partial T_i}{\partial x}$ and $\frac{\partial^2 T_i}{\partial x^2}$ on the shear viscosity current is negligible. The nonambipolar particle fluxes enter the derivation in the next section, which have been addressed in § 2.4.

2.6.3 Coupling

The relevant nonambipolar particle fluxes in (2.34) have been analyzed in Appendix A, for their dependence and scaling with plasma variables. In that section, the effect of the plasma variables v on each nonambipolar process k can be seen from the functions g_v^k for $v \in \{n, T, Z\}$,

$$J^k = e \Gamma^k = \sum_v g_v^k f(n, T, Z), \quad (2.35)$$

with f some function or operator. Substituting the expressions for the different nonambipolar particle fluxes in (2.34) couples the normalized electric field p.d.e. with those for the density and temperature. Note that the density and temperature for electrons and ions are presumably equal such that the subscript of the plasma variables (n, T) may be dropped for a two-fluid plasma.

$$\begin{aligned} \frac{m_i n T}{e \rho_{pi}} \left(\frac{B_p}{B} \right)^2 \frac{\partial Z}{\partial t} &= \frac{m_i n \mu_i T}{e \rho_{pi}} \frac{\partial^2 Z}{\partial x^2} + B_p^2 \left[\left(g_n^{\text{an}} - g_n^{\text{cx}} - g_n^{\pi\parallel} \right) \frac{1}{n} \frac{\partial n}{\partial x} \right. \\ &\quad \left. + \left(g_T^{\text{an}} - g_T^{\text{cx}} - g_T^{\pi\parallel} \right) \frac{1}{T} \frac{\partial T}{\partial x} + \left(g_Z^{\text{an}} - g_Z^{\text{cx}} - g_Z^{\pi\parallel} \right) Z - f^{\text{ol}}(Z) \right], \end{aligned} \quad (2.36)$$

$$f^{\text{ol}}(Z) = g^{\text{ol}} \frac{\exp \left(-(\nu_{*i} + Z^4)^{1/2} \right)}{(\nu_{*i} + Z^4)^{1/2}} \quad (2.37)$$

There are some key differences that complicate a comparison of (2.36) to the model equation (2.17). The thermodynamic forces are multiplied by $\frac{T}{n}$ in the original model, which influences the coefficient

definition, and the terms affecting Z must be approximated to reveal a polynomial function. Therefore, the next section aims to couple the parameters of the model equation (2.17) to the expressions that are found in (2.36), i.e., the partial differential equation containing the nonambipolar process contributions.

2.6.4 Comparison

The equivalence of the model p.d.e. (2.17) and physics-based p.d.e. (2.36) for the electric field can be seen from the last step of the derivation. The physics-based electric field p.d.e. (2.36) can be phrased into a form that is equivalent to the model p.d.e. (2.17):

$$\hat{\varepsilon} \frac{\partial Z}{\partial t} = \hat{\mu} \frac{\partial^2 Z}{\partial x^2} + \frac{\hat{c}_n T}{n^2} \frac{\partial n}{\partial x} + \frac{\hat{c}_T T}{n} \frac{\partial T}{\partial x} + \frac{T g(Z)}{n}. \quad (2.38)$$

Note that this electric field p.d.e. format is multiplied by $\frac{T}{n}$ similar to the model electric field p.d.e. (2.17). In (2.38), we defined the derived coefficients $\hat{\varepsilon}, \hat{\mu}, \hat{c}_n, \hat{c}_T$ and function $g(Z)$ according to the naming of the model equation (2.17). Now, we express the physics-based coefficients and approximation in terms of the nonambipolar current contributions and evaluate these for the case study parameters denoted in Appendix § A.1.

The electric field time scale is determined by $\hat{\varepsilon}$, whereas $\hat{\mu}$ governs the layer thickness in which the electric field curvature is significant. Therefore, $\hat{\varepsilon}$ and $\hat{\mu}$ can be seen as a time and ‘length’ (i.e., size of transport barrier) scale, respectively, defined by:

$$\hat{\varepsilon} = \frac{m_i T^2}{e \rho_{pi}} \left(\frac{B_p}{B} \right)^2, \quad \hat{\mu} = \frac{m_i \mu_i T^2}{e \rho_{pi}}. \quad (2.39)$$

The time scale and shear viscosity coefficients are set to $\varepsilon \sim \mu \sim 10^{-2}$ in [15, 85, 99]. Important to note is that both values should be significantly smaller than unity such that the transition is localized in space and time. The viscosity coefficient $\hat{\mu}$ is about an order of magnitude larger, whereas the time scale $\hat{\varepsilon}$ is comparable,

$$\hat{\varepsilon} \approx 9.6 \cdot 10^{-3} \quad \text{and} \quad \hat{\mu} \approx 8.5 \cdot 10^{-1}, \quad (2.40)$$

for $T = 10^3$ [eV], $n = 10^{19}$ and $D \sim \mu_i := 1$. The other parameters used for computation are given in Appendix § A.1.

The thermodynamic coefficients \hat{c}_n and \hat{c}_T can be expressed in terms of the nonambipolar contributions affected by the density and temperature gradient, respectively:

$$\hat{c}_n = B_p^2 \left(g_n^{\text{an}} - g_n^{\text{cx}} - g_n^{\pi\parallel} \right), \quad \hat{c}_T = B_p^2 \left(g_T^{\text{an}} - g_T^{\text{cx}} - g_T^{\pi\parallel} \right). \quad (2.41)$$

The coefficients corresponding to the thermodynamic forces, i.e., \hat{c}_n and \hat{c}_T , are depicted for a range of plasma temperatures in Figure 2.2. It can be seen that the thermodynamic coefficients vary significantly with temperature, whereas the model parameters $c_{n,T}$ are constants. However, their order of magnitude is comparable to the model parameters (i.e., $c_n \sim c_T \sim 1$ [85, 15]).

The polynomial coefficients are derived from a function fit to the normalized electric field terms, i.e., the contributions included in $g(Z)$:

$$g(Z) = \hat{b}Z - \hat{f}^{\text{ol}}(Z) \\ \hat{b} = B_p^2 \left(g_Z^{\text{an}} - g_Z^{\text{cx}} - g_Z^{\pi\parallel} \right), \quad \hat{f}^{\text{ol}} = B_p^2 f^{\text{ol}}(Z) \quad (2.42)$$

This function fit provides the polynomial coefficients, for $T = 10^2$ [eV]:

$$a = -7.00, \quad b = 8.00, \quad c = -4.00, \quad Z_S = 0.90 \quad (2.43)$$

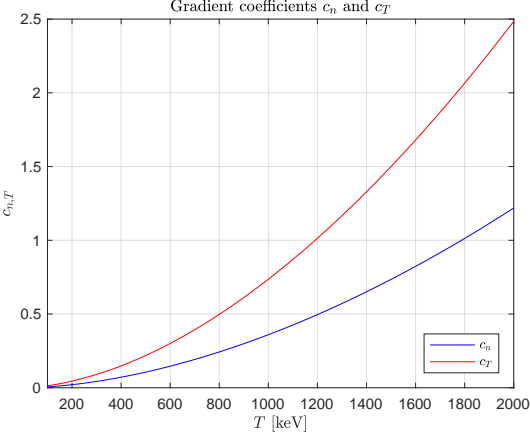


Figure 2.2: Thermodynamic coefficients c_n and c_T for the temperature range $T \in [0.1, 2.0]$ [keV].

We applied the scaling by $\frac{T}{n}$, since this section aims at a comparison to the model equation (2.17). However, we state that this scaling greatly reduces the contribution of $g(Z)$ in the physics-based electric field p.d.e. (2.38). Therefore, the factor is not taken into account for computation of $g(Z)$.

The physics-based function $g(Z)$ is shown for the temperature range relevant to the transport barrier region in Figure 2.3, where the function is inverted for clarity (i.e., $-g(Z)$ depicted). It can be seen that the polynomial inflection increases with plasma temperature and shows an exponential dependency on electric field. The asymmetric dependence on the electric field is hardly emphasized due to $|g(Z)|$ for low and high temperature. Therefore, the physics-based approximation $g(Z)$ and a function fit thereof are shown for $T_{\text{ped}} = 10^2$ [eV] in Figure 2.4.

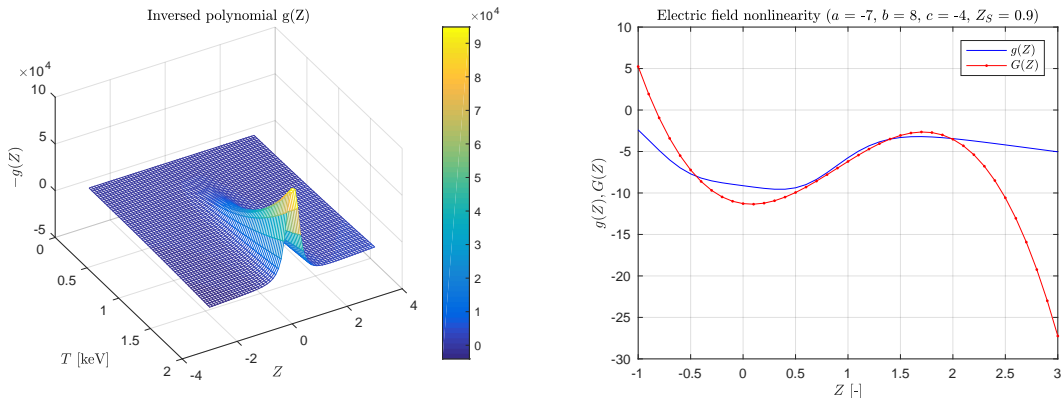


Figure 2.3: $-g(Z)$ in the T, Z space.

Figure 2.4: Functions $g(Z)$ and $G(Z)$.

As can be seen from Figure 2.3, the amount of inflection near Z_S of $g(Z)$ becomes larger with increasing plasma temperature. Because the orbit losses dominate the polynomial contribution to the equation, the polynomial value scales locally as,

$$g(Z) \sim g^{\text{ol}} \sim \nu_{\text{eff}} \rho_{pi} \sim (\nu_{ii} + \alpha_{\text{ino}} \omega_{bi}) \rho_{pi} \propto T_i, \quad (2.44)$$

which explains the trend. However, this means that for other choices of the constants, α_{an} , α_{cx} and α_{ino} , the ratio between the contributions differs significantly. Furthermore, this leads to different transition behavior, for example, when the transition occurs from a state of low or high temperature. Also, the various contributions will be different for another tokamak than JET or plasma regime (e.g., higher collisionality).

2.7 Hysteresis

Future plasma scenarios are considered that rely on hysteresis [20], for the power threshold scales with density as $P_{\text{thr}} \propto n^{0.8}$. The necessity of low heating power arises from the limited power capability of heating systems and an irregular heat flux from edge localized modes (e.l.m.). Therefore, there have been many experimental campaigns devoted to understanding the hysteresis and determining control parameters (e.g., [12][16]). The hysteresis is often visualized by a gradient-flux relation, e.g., electron pressure gradient versus separatrix heat flux: $\nabla p_e(P_{\text{sep}})$. This reveals the asymmetry in the forward and back transitions.

According to the attempted definition of Morris [51], *hysteresis is a property of dynamic systems that have multiple (meta)stable equilibria and dynamics on a time scale much faster than the variations of input (rate-independence)*. Hysteresis arises naturally in L-H transition models using a nonlinearity such as $G(Z)$ with certain parameters. This gives a hysteresis in the forward and backward transition, whereas the transitions occur on the electric field (or turbulence) time scale and intermediate evolution on the transport time scale.

Bifurcation analyses have shown the existence of hysteresis in transition models of Diamond and co-workers [61], Toda and co-workers [87] and Ball [77]. Toda and co-workers [86] observed the existence of both a smaller and larger hysteresis curve, depending on the relative strength of ion orbit, anomalous electron and bulk viscosity fluxes (details can be found in Appendix A). This indicates that the hysteresis in such models depends on the nonambipolar fluxes considered. But even for fixed parameters, the hysteresis size may still depend on exogeneous control parameters such as heating power rate in the model of Malkov [61].

In the model described in § 2.5, the existence and size of the hysteresis are governed by two different parameters: b and c . Changing these parameters, the sharp transitions may be retained while hysteresis disappears, or the sharp transitions change to smooth transitions without hysteresis [99]. In the physics-based derivation, the dependence of parameters \hat{c}_n , \hat{c}_T , \hat{a} , \hat{b} and \hat{c} on temperature T and density n can be seen from the radial currents. Despite the variation of these parameters with temperature, their behavior appears linear around the nominal temperature used for evaluation. Furthermore, the density dependence drops out of the equations due to the scaling by density and temperature.

We conclude the derivation by stating that the parametric dependence on the plasma variables n and T is left out of further discussion and the parameters are assumed to be constant. However, we do use the gained insight in the definition of the control objective, which is focused on dealing with model uncertainty. The edge transport barrier is described in the next section, which relates to the steady state H-mode behavior of the plasma model after the L-H transition.

2.8 Edge transport barrier

The edge transport barrier (e.t.b.) is one of the key manifestations of the H-mode physics, which is treated shortly from an experimental viewpoint in § 2.8.1. This allows to substantiate the modeling choices for control analysis and design. The implications of plasma operation on the transport barrier are discussed in § 2.8.2 to reveal important observations that are not captured in the model nor the control-related efforts in this study.

2.8.1 H-mode physics

The reduction of transport coefficients at the plasma edge causes a local increase of temperature and density gradients [66, 12], consistent with the energy and particle fluxes from the plasma core. Meanwhile, the core transport retains its turbulent character. The plasma density and temperature profiles in H-mode are thus effectively biased, compared to the L-mode profiles [65]. This profile bias can be seen from Figure 2.5, where the profiles of electron density (n_e), ion temperature (T_i) and radial electric field (E_r) have been obtained from Maggi et al. [13] for a typical H-mode discharge: JET#75828. Also, the normalized electric field is computed and depicted in Figure 2.5 according to our definition (2.18).

Bifurcation at the transition leads to a radial electric field well, which generates a sheared $\mathbf{E} \times \mathbf{B}$ flow. It can be seen in Figure 2.5 that the radial electric field decreases sharply towards the separatrix, where the bottom of the well-like structure is located for the JET H-mode. However, the electric field well is often observed just inside the last closed flux surface during plasma discharges on, e.g., JET [12, 103], DIII-D [66] and Alcator C-Mod [80]. Due to the generation of poloidal and toroidal flow, the energy confinement of the plasma is usually doubled for a given heat flux.

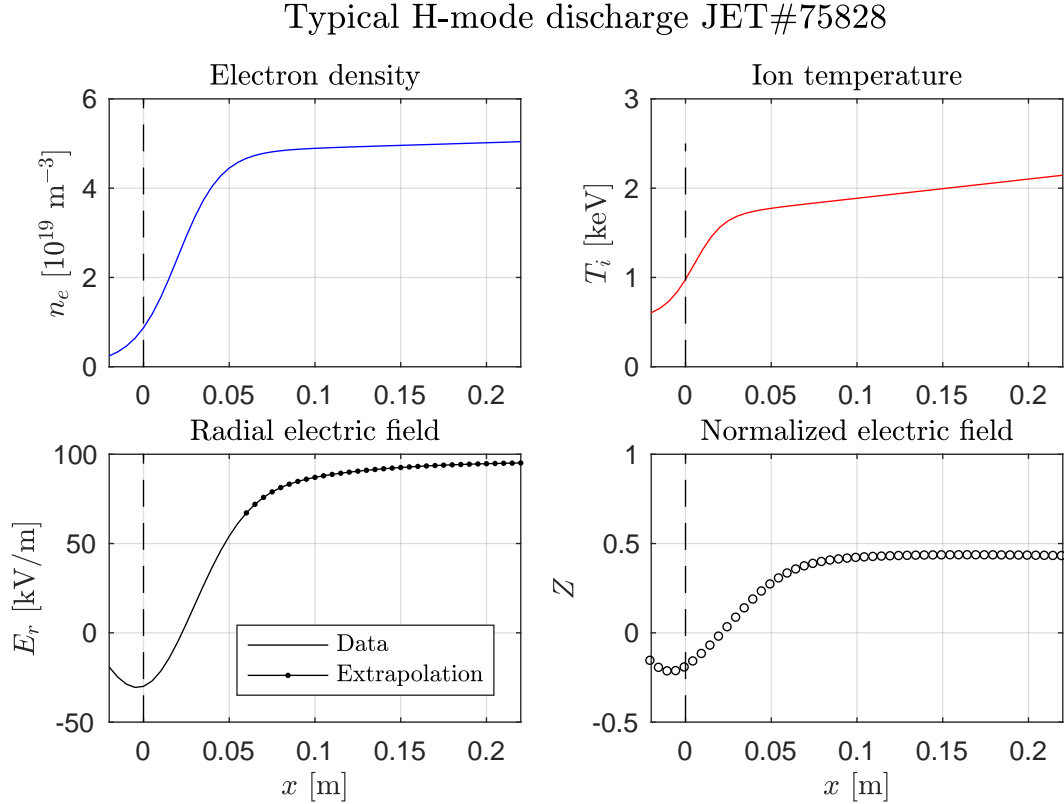


Figure 2.5: Experimental profiles of n_e , T_i and E_r from JET#75828 discharge [13] are depicted along the distance to the separatrix, i.e., $x = R_{\text{sep}} - R$. The normalized electric field Z profile has been computed using the T_i and E_r data. Note that the radial electric field E_r is extrapolated for $x \geq 0.055$ [m].

A suppressed transport region can be initiated also in the plasma core, so the suppressed edge region is referred to in literature as the edge transport barrier (e.t.b.) [65]. After the L-H transition, the edge transport barrier is characterized by a pedestal height (maximum edge pressure) and width (radial extent of edge gradient). The pedestal height arises from the width in combination with the gradient magnitude. Therefore, the pedestal width is an additional degree of freedom (d.o.f.) determining the (time-averaged) pedestal pressure, which is key to fusion performance.

The pressure gradient, however, may reach various instability boundaries, when the heating power is further increased after the transition. The most detrimental limit is set by edge localized modes (e.l.m.), a type of magnetohydrodynamic (m.h.d.) instability, which periodically degrade the transport barrier and profile gradients [92]. e.l.m. are not taken into account here, because we focus on operation near the H-L bifurcation. This means that the pressure gradient is presumably far from m.h.d. instability boundaries. However, there are several control techniques that deal with operational issues during the H-mode, which are reviewed shortly in § 2.8.2.

2.8.2 Control of edge transport barrier

Edge transport barriers are generated usually with heating power as main control parameter, whereafter the L-H transition seems to occur 'spontaneously'. Additionally, there are reports of 'stimulated' e.t.b. induced by suprathermal molecular beam injection [82] and pellet injection [75]. Interestingly, the Reynolds stress and radial electric field coincide in time during the SMTBI-induced transitions, indicating a distinct path to the H-mode without zonal flow generation [48]. Pellet ablation increases the density locally, while the plasma temperature is lowered by the interaction with frozen neutrals. Therefore, the radiative power is decreased, while the plasma self-heating is raised. The enlarged heat flux across the separatrix then may lead to a transition to H-mode, even below the power threshold [67].

Although e.l.m. are not considered, the related control strategies are definitely relevant to the L-H transition. Resonant magnetic perturbations (r.m.p.) are the main experimental tool to control the e.l.m. frequency [59], which may even completely suppress the e.l.m. instability [54]. However, the impact of r.m.p. on the transition behavior is fierce, for the power threshold increases with perturbation amplitude and hysteresis is decreased [60]. Both resonant magnetic perturbations, external momentum input and particle injection could be considered when a control strategy is devised. However, we first focus on the heat flux as it is the main experimental control parameter.

2.9 Discussion

The derivation of the electric field p.d.e. involves a large set of assumptions, which are motivated by the purpose of obtaining the model p.d.e. described in § 2.5. For example, the assumption that the spatial derivatives of temperature are negligible is not valid per se such that small errors are introduced along the derivation. However, the most important assumption lies in the basis of nonambipolar particle fluxes that are used for the derivation in § 2.6. It is known that the fluctuation-induced processes also play a (possibly important) role during the L-H transition and H-mode. We are able to neglect the fluctuation-induced contributions within frame of the time and length scales considered. However, the fluctuating contributions, e.g., Reynolds and Maxwell stress, may significantly influence the electric field dynamics and alter the bifurcation landscape.

The model hysteresis had already been coupled to the parameters b, c in [99], which is the subject of § 2.7. By deriving the p.d.e. for electric field, we have shown that these model parameters are physically linked to the plasma variables. The model parameters assume approximately a constant value for a fixed parameter regime, but this assumption is invalid when there are large changes in the plasma variables.

To cope with the complexity, we choose fixed parameters in the H-mode for modeling along the lines of [15, 100, 101, 85] and do not include the gained insight on the state-dependencies. This is because the model already belongs to the (general) class of distributed parameter systems, in which model coefficients are functions of space (i.e., through $D(\mathcal{E}(x))$). We believe that dealing with this type of domain-dependency sufficiently substantiates the control problem. Yet, the obtained knowledge of the model parameters' origin motivates us to focus the control objective on model uncertainty.

Chapter 3

Model analysis

This thesis aims to investigate the possibility of stabilizing the L-H transition model described in § 2.5 near the H-L bifurcation. The current section attempts to bridge the gap between the L-H transition and H-mode physics that are central to Chapter 2 and design of the boundary feedback control treated in Chapter 4. In § 3.1, we specify the control problem in terms of the objective and physical context. We reason that a boundary feedback control is suitable to tackle the control problem. The nonlinear p.d.e. model is analyzed in § 3.2 to obtain insight in its dynamical behavior and substantiate the control objective. The result hereof is used to specify the linearized p.d.e. model, which is described § 3.3. The control design procedure is facilitated by the transformation into the reference p.d.e. system in § 3.4. Hereafter, we formulate the so-called target system in § 3.5 based on the reference p.d.e. system, which defines the objective for control design.

3.1 Control problem

3.1.1 Objective

The incentive for low heating power is at least twofold. The heat flux out of the plasma column determines the external heating power for a non-burning plasma (without alpha heating). Eventually the heat flux must be exhausted by the divertor, which is preferably as low as possible for lifetime and reliability. Secondly, the energy expelled by edge localized modes scales with heating power. This makes it desirable to get the plasma state near the H- to L-transition by exploiting the hysteresis in power threshold.

The nonlinear p.d.e. model yields the L- and H-mode as a locally stable equilibrium, at least for the parameter range that exhibits hysteresis with sharp transitions [99]. This transition behavior is schematically depicted in Figure 3.1, where the L-H and H-L transition are indicated by a double arrow. Because this plasma behavior is of major interest to our purpose, the model parameter range considered is bounded to the part of parameter space that gives rise to hysteresis. The hysteresis is expressed also in Figure 3.1, where the power threshold for the H-L transition P_{HL} is clearly smaller than that to obtain H-mode P_{LH} . Using any (stable or unstable) equilibrium for this parameter subset, we can obtain the linearization of the nonlinear p.d.e. system that yields the linear p.d.e. system. However, we are restricted to the set of (meta-)stable equilibria, because there are no analytical solutions of the plasma model known [100, 101, 15, 85, 32]¹. As a result, it is difficult to find the properties of an unstable equilibrium, because such solutions diverge immediately using numerical methods.

The set of stable equilibria in H-mode can easily be found by numerical computation. An approach is to compute such a stable equilibrium rather close to the H-L bifurcation point (in state space for fixed parameters). Then, the linear p.d.e. system obtained around that equilibrium can be used to design the feedback control. Along similar lines of thought, the bifurcation analyses of [15, 32, 99] have strived to

¹Note that an approximate analytical solution has been found by Veldman [15] for $D(Z)$, i.e., diffusivity depending on electric field value. Hence, we can not use this result.

explore and organize the parameter space of the nonlinear p.d.e. model and succeeded. Their results, approach and estimates enable us to determine critical values for the boundary conditions (b.c.) at the plasma core, which constitute the control inputs for our purpose. We can for example quite easily determine the parameter space with hysteresis, fix a set of parameters and estimate the corresponding heat flux threshold for the L-H and H-L transition.

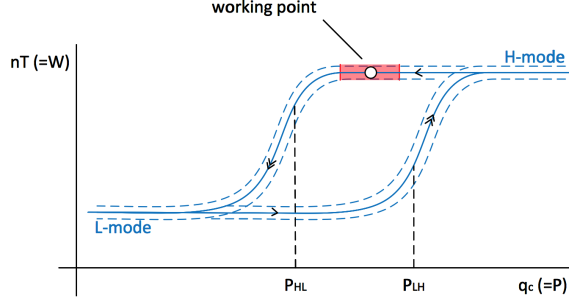


Figure 3.1: Schematic of the control objective in (q_c, nT) -space.

In summary, we can define an approach to investigate our research question. Let \mathcal{P}_1 denote the nonlinear p.d.e. system with nominal parameter set and equilibrium $\bar{\mathbf{v}}_1$ near the H-L bifurcation. This equilibrium is depicted in Figure 3.1 as the working point. The approach is initiated as to obtain a linear p.d.e. description \mathcal{L}_1 about the stable equilibrium $\bar{\mathbf{v}}_1$. This linear p.d.e. system is used to design the feedback control.

The eventual feedback controller should handle an uncertainty in the parameter set. We call the equilibrium of the nonlinear p.d.e. model with the mismatched parameters \mathcal{P}_2 , which has a different equilibrium $\bar{\mathbf{v}}_2$. The model mismatch is shown schematically by the red frame surrounding the working point in Figure 3.1. The control objective can be used to formulate the following control question: *Can we design a feedback control for \mathcal{P}_1 based on \mathcal{L}_1 that also stabilizes \mathcal{P}_2 for a fixed model mismatch, $\Delta\mathcal{P} = \mathcal{P}_2 - \mathcal{P}_1$?* The research question then formulates that we are interested in the allowed model mismatch in parameter space, and whether \mathcal{P}_2 may be an unstable equilibrium across the H-L bifurcation point for \mathcal{P}_1 .

3.1.2 Physical context

The nonlinear p.d.e. model has been treated extensively in Chapter 2. Here, we consider the implications of the physical context for feedback control. The control issue of state-reconstruction or output-based feedback is not discussed, because we focus on full-state feedback control. The actuation inputs are constituted by the boundary conditions of the nonlinear p.d.e. model as can be seen from Figure 3.2, i.e., the heat and particle flux, respectively: $q_c(t), \Gamma_c(t)$. This means that the system is underactuated, since there are two degrees of freedom compared to three infinite-dimensional state variables. Without domain sources as actuation input, we require a feedback control that uses the boundary conditions as control inputs and accounts for the spatial distribution of the model parameters. Hence, we search for a full-state boundary feedback control that acts on the plasma core boundary only.

Full-state knowledge means that the state may be inquired at any spatial point. This enables the use of a wide-spread variety of state-feedback control procedures. State-feedback control exists for both linear and nonlinear systems, whereas not necessarily, but often, the models are discretized in space to obtain an equivalent o.d.e. system. Note that such o.d.e. descriptions are extremely useful for real-time control, when a small o.d.e. system can be used as a model. However, for off-line applications, the spatial discretization is also clearly motivated by the availability of many linear control methods. There are various linear control theories specialized in handling specific control objectives. For instance, robust control is especially suitable to account for model-plant mismatches, whereas model predictive control takes actual account of state and control input constraints. However, our purpose is not restricted by

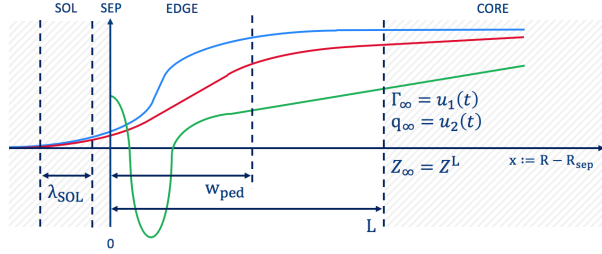


Figure 3.2: Control-relevant physical context of the plasma model.

engineering requirements and constraints. By contrast, we are mainly motivated by the quest to clarify the possibilities and identify challenges. This allows to retain the system definition close to the nonlinear p.d.e. system such that we can use whatever physical insight for a deepened analysis of the control problem. Also, it facilitates the discussion between the physicist and control engineer as the original model extends far into the design procedure.

Yet we reasoned that the control procedure should account for spatial distribution of parameters and full-state feedback. The linear p.d.e. system itself may be used for the design of a boundary feedback control. Although the bifurcation behavior is lost, the linear p.d.e. system still constitutes a domain-dependent problem involving diffusion, advection and reaction terms equivalent to the nonlinear p.d.e. model. We are motivated to explore the backstepping boundary control procedure derived in [78], because this represents the state-of-the-art in backstepping for p.d.e. systems. It is supposed to yield a systematic manner of defining a target system based on the original model. This design procedure is detailed to a coupled system of linear partial differential equations that contain spatially-varying diffusion, advection and reaction coefficients. Since we are not specifically focusing on disturbance rejection or output feedback, the application of this method resembles a well-defined first attempt to answer the control question.

3.2 Nonlinear p.d.e. system

The L-H transition model introduced in § 2.5 is phrased into a nonlinear p.d.e. system description in § 3.2.1 for numerical implementation. In parallel, we state specific modeling choices used in this thesis in view of control design. We investigate the parameter space of the nonlinear p.d.e. system, where we define the nominal parameter set for \mathcal{P}_1 . Throughout this analysis, the s.o.l. equilibrium solution is determined analytically for the nominal parameter set. A numerical solution is obtained for the nonlinear p.d.e. system in open-loop that yields the corresponding equilibria in L- and H-mode.

3.2.1 Assumptions and definition

This section denotes the assumptions used to translate the L-H transition model into the nonlinear p.d.e. system, which forms the basis for control analysis and design. The L-H transition model is introduced in § 2.5, which contains an o.d.e. for turbulence, three nonlinear p.d.e. and a set of boundary conditions to define the plasma edge behavior on the domain Ω (3.1).

$$\Omega = \{x, t \in \mathbb{R}^2 \mid (0 \leq x \leq L) \wedge (t \geq 0)\} \quad (3.1)$$

The turbulence o.d.e. can be simplified through time scale separation. We assume that the time scale of turbulence level \mathcal{E} is small compared to other plasma processes. Hence, the turbulence o.d.e. (2.3) can be evaluated to determine its stable equilibrium:

$$\bar{\mathcal{E}}_1 = \frac{\gamma_1}{\alpha_{\text{sat}}} \frac{1}{1 + \alpha_{\text{sup}} (Z_x)^2} \quad (3.2)$$

where the solution $\bar{\mathcal{E}}_2 = 0$ is unstable. Note that we introduced the subscript notation of partial derivatives for readability, which is often used in p.d.e. literature. Whenever it improves the readability, the partial derivatives of, e.g., \mathbf{v} with respect to time and space are denoted \mathbf{v}_t and \mathbf{v}_x , respectively. The diffusivity function $D(\mathcal{E})$ (2.13) reduces to a function of electric field shear directly:

$$D(Z_x) = D_{\min} + \frac{D_{\max} - D_{\min}}{1 + \alpha_{\sup}(Z_x)^2}, \quad (3.3)$$

which is independent of the rates of growth γ_1 and saturation α_{sat} by definition of \mathcal{E}_{\max} (2.13).

The derivation of the electric field p.d.e. in § 2.6 assumes a constant viscosity coefficient μ for the purpose of derivation. However, the control design is greatly assisted by a functional similarity in the diffusion coefficients. This motivates the redefinition of the shear viscosity current defined in (2.17) for the L-H transition model into:

$$\frac{\partial}{\partial x} \left(\mu D(Z_x) \frac{\partial Z}{\partial x} \right), \quad (3.4)$$

where $\mu \ll 1$ to remain locality of Z_{xx} in Z_t . Physically, a spatially-dependent viscosity coefficient is more realistic [83, 45, 64] and Itoh [42] state even that the (cross-field momentum) transport coefficient μ actually depends on the radial electric field shear. This can be seen from the idea that if the viscosity becomes smaller, also the

It is often assumed that the inclusion of viscosity does not alter the bifurcation behavior qualitatively for sufficiently small μ [99]. Yet the viscosity term enables the existence of a smooth solution, when there is a spatial transition from L-mode (core) confinement to H-mode (edge) confinement. We also assume that including the diffusivity coefficient amounts only to a local smoothening effect.

Through the introduction of the p.d.e. for temperature, we can define the nonlinear system state $\mathbf{v}(x, t)$ by the infinite-dimensional vector:

$$\mathbf{v}(x, t) = [n(x, t), T(x, t), Z(x, t)]^\top. \quad (3.5)$$

The set of p.d.e. (2.10), (2.16) and (2.17) are included in the coupled nonlinear p.d.e. system for brevity, where we use the new diffusivity function (3.3) and assumed shear viscosity contribution (3.4):

$$\mathbf{v}_t = \partial_x F(x, t, \mathbf{v}, \mathbf{v}_x) + S(x, t, \mathbf{v}, \mathbf{v}_x) \quad (3.6)$$

where the flux and source function, F and S , respectively, are defined as:

$$F = \begin{bmatrix} D(Z_x) \frac{\partial n}{\partial x} \\ \frac{D(Z_x) \partial T}{\zeta} \\ \frac{\mu D(Z_x) \partial Z}{\varepsilon} \end{bmatrix}, \quad S = \begin{bmatrix} 0 \\ \left(\frac{\zeta+1}{\zeta} \right) \frac{D(\mathcal{E})}{n} \frac{\partial n}{\partial x} \frac{\partial T}{\partial x} \\ \frac{c_n T}{\varepsilon n^2} \frac{\partial n}{\partial x} + \frac{c_T}{\varepsilon n} \frac{\partial T}{\partial x} + \frac{G(Z)}{\varepsilon} \end{bmatrix} \quad (3.7)$$

For clarity, the domain boundary is defined as a subset of Ω (3.1),

$$\delta\Omega = \{x, t \in \Omega \mid x = 0 \wedge x = L\}, \quad (3.8)$$

such that the boundary conditions of Robin- and Neumann-type can be phrased into the general format:

$$p(x, t, \mathbf{v}) + F(x, t, \mathbf{v}, \mathbf{v}_x) = 0, \quad \text{for } (x, t) \in \delta\Omega \quad (3.9)$$

By definition of flux function f , the set of b.c. can be described concisely by $p(x, t)$ where $x \in \delta\Omega$:

$$p(0, t) = - \begin{bmatrix} D(Z_x) & \frac{n}{\lambda_n} \\ \frac{D(Z_x)}{\zeta} & \frac{T}{\lambda_T} \\ \frac{\mu D(Z_x)}{\varepsilon} & \frac{Z}{\lambda_Z} \end{bmatrix}_{x=0} \quad \text{and} \quad p(L, t) = \begin{bmatrix} \Gamma_c(t) \\ \frac{(\gamma - 1)q_c(t) - T\Gamma_c(t)}{n} \\ 0 \end{bmatrix}_{x=L} \quad (3.10)$$

with $\Gamma_c(t)$ and $q_c(t)$ actuation parameters. Note that we used the short-hand notation \mathbf{v} for the plasma variables, which depend on both space and time $\mathbf{v}(x, t)$. The nonlinear p.d.e. system is now ready for numerical implementation in the MATLAB PDE toolbox, which enables us to simulate the nonlinear p.d.e. system on a non-uniform grid.

3.2.2 Nominal plant \mathcal{P}_1

The influence of model parameters on the equilibria of the nonlinear p.d.e. system is analyzed in this section. This analysis substantiates the nominal plant definition \mathcal{P}_1 for control design, which is listed in Table 3.1. The nominal plant features an equilibrium solution in H-mode that is qualitatively comparable to experimental observations. An example of experimental profiles is depicted in Figure 2.5.

Table 3.1: Parameter set \mathcal{P}_1 contains the basic parameters adopted from [85].

Γ_c	γ	λ_n	λ_T	λ_Z	D_{\min}	D_{\max}	ζ	c_n	c_T	q_c	a	b	c	Z_S	α_{\sup}	μ	ε
$-\frac{4}{5}$	$\frac{5}{3}$	$\frac{5}{4}$	$\frac{3}{2}$	$\frac{5}{4}$	$\frac{2}{5}$	2	$\frac{1}{2}$	-1.1	-0.9	-4	$\frac{3}{2}$	2	-1	$-\frac{3}{2}$	$\frac{1}{2}$	$\frac{1}{20}$	$\frac{1}{25}$

Transport

A subset of the model parameters is not used explicitly for bifurcation analysis, the values of which can be obtained from Paquay [85] or Veldman [15]. Most often, the heat flux q_c constitutes the primary actuation parameter and the particle flux Γ_c is constant. The adiabatic index γ relates to the three degrees of freedom. Furthermore, the decay length scales (of plasma variables) into the scrape-off layer $\lambda_{n,T}$ are also default. However, it should be noted that the s.o.l. boundary conditions may affect the solution significantly.

The maximum (effective) particle diffusivity is set to the order of magnitude usually observed in L-mode discharges, see for example [36, 35]. Therefore, the nominal plant agrees with the following observations:

- Heat and particle diffusivity are reduced by approximately the same ratio upon a transition into H-mode [36]. Hence, the use of the simplified relation for χ is legitimate and we set $\zeta = \frac{1}{2}$ to imply $\chi \sim 3D$.
- Heat diffusivity χ reduces by a factor five across the L-H transition [36], which implies that: $D_{\min} \sim \frac{1}{5}D_{\max}$.

Thermodynamic currents are accounted for in the electric field p.d.e. through the coefficients $c_{n,T}$ affecting n_x and T_x . After analysis of nonambipolar particle fluxes, it has been noted that the thermodynamic coefficients vary significantly with plasma temperature. However, we adopt usual values due to the discrepancy in scaling of $g(z)$ in that analysis and derivation. Though their contribution maintains magnitude, we define negative thermodynamic currents for positive gradients $n_x, T_x > 0$. This is motivated by the spatial domain $-L \leq x \leq 0$ used in Weymiens et al. [100], where the thermodynamic coefficients are positive for $n_x, T_x < 0$ and the polynome as $-G(Z)$. Hence, the thermodynamic coefficients are defined negative due to $n_x, T_x > 0$ and we set the values for $G(Z)$ accordingly.

Bifurcation behavior

Ceteris paribus, the polynomial coefficients determine the electric field solution at the scrape-off layer. The s.o.l. equilibrium for Z can be computed analytically due to the Robin-type boundary condition, i.e., $Z_x(0, t) = Z(0, t)\lambda_Z^{-1}$. However, it should be noted that this requires to assume $\mu \ll 1$, which is accounted for further on. The steady state solutions $\bar{n}(x)$, $\bar{T}(x)$ and $\bar{Z}(x)$ are restated directly from [85, 15] or [99, §4.4], which for constant fluxes Γ_c and q_c can be denoted:

$$\bar{n}(x) = \bar{n}(0) - \int_0^x \frac{\Gamma_c}{D(\bar{Z}_x(x))} dx, \quad \bar{n}(0) = -\frac{\Gamma_c \lambda_n}{D(\bar{Z}_x(0))} \quad (3.11)$$

$$\bar{T}(x) = \frac{(\gamma - 1) q_c}{\Gamma_c} \left(1 - \lambda_g \left(\frac{\bar{n}(x)}{\bar{n}(0)} \right)^{-\zeta} \right), \quad \lambda_g = \frac{\frac{\lambda_n}{\zeta \lambda_T}}{1 + \frac{\lambda_n}{\zeta \lambda_T}} \quad (3.12)$$

$$G(\bar{Z}(x)) = \theta D(\bar{Z}(x)), \quad \theta = \frac{(\gamma - 1) q_c}{\Gamma_c^2 \lambda_n^2} (c_n + c_g), \quad c_g = \frac{\zeta c_T - c_n}{1 + \zeta \frac{\lambda_T}{\lambda_n}} \quad (3.13)$$

where the bar refers to an equilibrium solution. Note that the density and temperature solution are functions of diffusivity only, which is governed by the electric field (shear). This reveals the importance of the s.o.l. length scale λ_Z , the influence of which has been assessed in [85].

We adopt a set of polynomial parameters that corresponds to sharp transitions exhibiting hysteresis, for which the absolute values are based on previous bifurcation studies [85, 15, 101]. This is motivated by their mathematical background, whereas the parameter signs are defined by physical reasoning. First, define the steady state criterion for Z (3.13) by $S(Z)$:

$$S(Z) = G(Z) - \theta D(Z \lambda_Z^{-1}). \quad (3.14)$$

As can be seen from Figure 3.3 for $q_c = -2$, the steady state criterion $S(Z)$ and its derivative $S_Z(Z)$ with respect to Z indicate the existence of three solutions. There are two stable equilibria and one unstable solution, which are denoted \times (attracting) and \circ (repelling), respectively. We denote the solutions by the L-mode, intermediate (I) and H-mode equilibrium:

$$Z_H = -2.64, \quad Z_I = -1.80, \quad Z_L = -0.18. \quad (3.15)$$

Note that $G(Z)$ must be convex for $Z < Z_S$ and concave otherwise, because it leads to the existence of two stable solutions: the L- and H-mode equilibria.

Actuation

The influence of heat flux q_c cannot be easily assessed by inspection of Figure 3.3, because the heat flux is included in the system curve. However, the criterion $S(Z)$ (3.14) can be parameterized to obtain an equivalent system curve independent of θ . This allows to observe the influence of heat flux on the allowed equilibrium solution(s). The parameterization of $S(Z)$ is denoted by virtue of [100]:

$$G(Z_e) D(Z_e \lambda_Z^{-1}) = \theta(q_c) D(Z_e \lambda_Z^{-1})^2. \quad (3.16)$$

Figure 3.4 reveals the parameterization of $S(Z)$ as an inversed S-curve for $Z_e = [-4, 4]$. It effectively shows the values of the polynomial and diffusivity function (times $D(Z_x)$) corresponding to the same Z_e . Furthermore, there are three linear curves that relate to different heat fluxes. As can be seen from Figure 3.4, low heat flux yields L-mode confinement $D(Z_x)^2 \rightarrow D_{\max}^2$ (left y-axis) for $Z \rightarrow \infty$. There are three solutions for medium heat flux, which correspond to the L-, I- and H-mode equilibria. This implies that the L- and H-mode are meta-stable solutions, between which the system may transit. Further increasing the heat flux, H-mode represents the single equilibrium for sufficiently large values where $D(Z_x)^2 \rightarrow D_{\min}^2$.

The turbulence suppression rate α_{sup} determines the electric field shear that allows to enter H-mode. Two values for $\alpha_{\text{sup}} = \{0.1, 1.0\}$ have been compared by Weymiens et al. [101], which shows that the heat flux increases greatly for a small suppression coefficient. A turbulence suppression rate of order unity

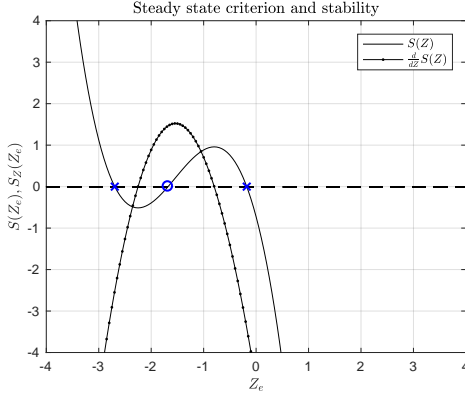


Figure 3.3: $S(Z)$ and $S_Z(Z)$ are evaluated at the s.o.l. for $Z = Z_e$ and $q_c = -2$.

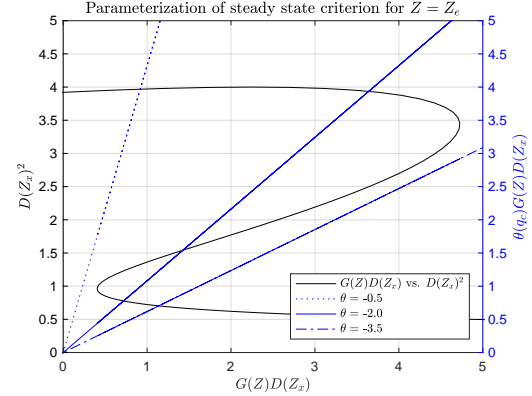


Figure 3.4: Parameterization of $S(Z)$ reveals the equilibrium solution(s) for different q_c .

conserves the bifurcation structure found for diffusivity function $D(Z)$ [100]. Furthermore, it should be noted that we have set α_{sup} to accomodate the difference in sharpness of L- and H-mode branches (of the S^{-1} -like system curve). Due to other parameters, an unity suppression coefficient results in a sharp turn towards the lower branch, which leads to large heat flux required for the L-H transition.

This concludes the motivation of nominal parameter set \mathcal{P}_1 , which is used for numerical computation. The equilibrium profile in L-mode and H-mode are depicted in Figure 3.5 and Figure 3.6, respectively. The L-mode profiles are monotonously increasing functions of x . H-mode profiles are qualitatively comparable to experiment, which features an edge transport barrier mostly expressed by steepened n_x around $x \approx 1$. Also, an electric field well can be seen near the scrape-off layer. This is because Z declines sharply around $x \approx 1$, flattens out at large $Z < 0$ and then increases again just before the separatrix. However, it can be seen that the electric field profile is flat for most of the domain. Hereto, it should be noted that the domain length is set as $L \gg 1$ only for justifying the boundary layer approximation, where $L = 10$ suffices numerically.

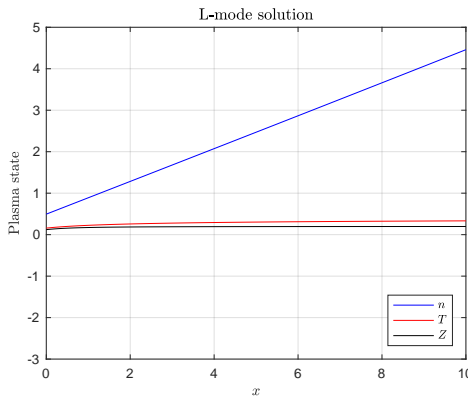


Figure 3.5: L-mode solution for the nominal plant \mathcal{P}_1 with monotonic gradients along the domain.

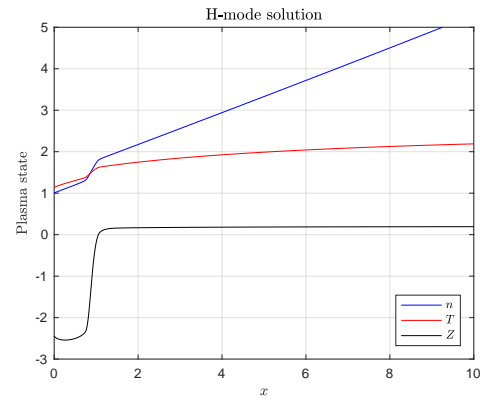


Figure 3.6: H-mode solution for the nominal plant \mathcal{P}_1 featuring electric field well and e.t.b.

Direct continuation

The nominal plant \mathcal{P}_1 is simulated with a time-varying heat flux to determine the heat fluxes at the L-H and H-L bifurcation, i.e., q_{LH} and q_{HL} . The approach is similar to the direct (1-parameter) continuation of equilibria for bifurcation studies [15, 85, 99]. This means that the heat flux is continuously changed to evolve the plasma model along a branch of equilibria that are qualitatively comparable. The goal is

to determine accurately the critical parameter value that yields a qualitative change of model dynamics, i.e., the L-H or H-L bifurcation.

The initial solution at $t = 0$ is constructed by roughly approximating the electric field:

$$Z(x, 0) = Z_S \left(1 - \tanh \left(\frac{L}{2} (x - 1) \right) \right) \quad (3.17)$$

such that density and temperature follow from (3.11) and (3.12). The heat flux directly actuates the temperature, while the electric field changes accordingly via the thermodynamic current caused by T_x . Plasma density changes only due to flow shear suppression of particle diffusivity. Therefore, the density response to heat flux is rather slow compared to plasma temperature. This implies that the heat flux must be slowly increased such that the system is allowed to settle at the next equilibrium.

As can be seen in Figure 3.7, the heat flux is ramped up and down to initiate the L-H and H-L bifurcations, which are marked by the sudden changes of $v(0, t)$ at time instants t_{LH} and t_{HL} , respectively. On the left of Figure 3.8, plasma profiles are shown before and after the L-H (left) and H-L (right) transition for $\Delta t = \pm 5$ to $t_{LH/HL}$, respectively.

At $t_{LH} \approx 1942$, the L-H transition in Figure 3.7 corresponds to the sudden jump of $Z(0)$ to the H-mode root Z_H for $q_{LH} \approx -4.88$. The density adapts to the reduced diffusivity, but the temperature decays just after the jump. This shows that the temperature dynamics are not critically damped like the density, which is due to advection. Also, it can be seen in Figure 3.8 that the electric field profile changes greatly across the L-H transition. The transport barrier has moved inward to about $x = 2$, already right after the transition.

After the q_c flat-top in Figure 3.7, the H-L bifurcation occurs at $t_{HL} \approx 2977$ for $q_{HL} \approx -3.15$ indicated by the sudden jump $Z_H \rightarrow Z_L$. Again, the density and temperature at the s.o.l. show similar behavior, whereas the electric field jump is slightly greater compared to L-H bifurcation. The plasma profiles right before and after the H-L bifurcation are shown in Figure 3.8. It can be seen that the profiles directly transit to the monotonic solution corresponding to the L-mode, see Figure 3.5.

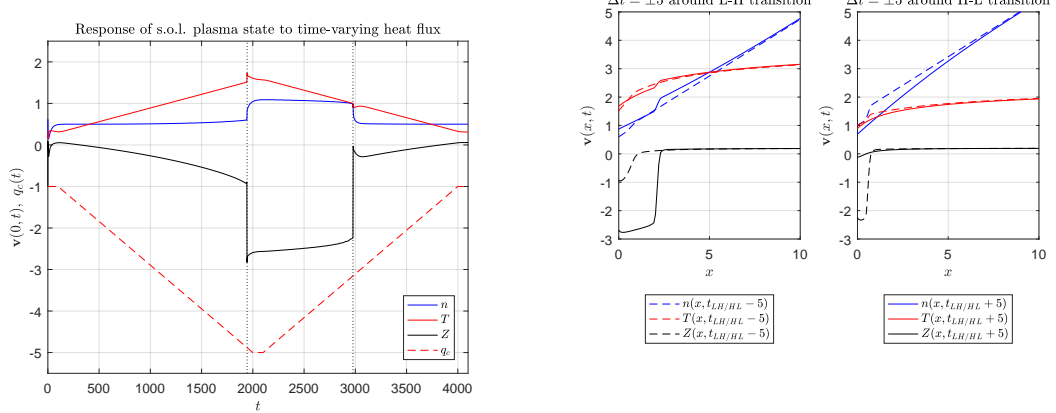


Figure 3.7: The heat flux is slowly ramped up and down for $-q_c = [\frac{1}{2}, \frac{7}{2}]$, which induces an electric field jump around $t_{LH} \approx 1942$. After the flat-top, the back (H-L) transition occurs at $t_{HL} \approx 2977$ for a heat flux about $2/3$ of q_{LH} .

Figure 3.8: The electric field profile after the forward/L-H (solid Z-profile in left plot) transition shows that the transport barrier immediately grows inward (towards the plasma core) due to the edge bifurcation, while it is much closer to the separatrix just before the back/H-L (dashed Z-profile in right plot) transition.

3.3 Linear p.d.e. system

3.3.1 Linearization

The linearization of the nonlinear p.d.e. system describes the local dynamics of the L-H transition model around the H-mode equilibrium solution of \mathcal{P}_1 (depicted in Figure 3.6) on the same domain:

$$\Omega = \{x, t \in \mathbb{R}^2 \mid 0 \leq x \leq L \wedge t \geq 0\} \quad (3.18)$$

The linearized version of the nonlinear system has been derived in Appendix B and belongs to the class of linear spatially-varying reaction-advection-diffusion systems.

Description 1. Let $x, t \in \Omega$. The term *linear p.d.e. system* is used to denote the linearization of (3.19) with state vector $\tilde{\mathbf{v}}(x, t)$ and boundary conditions $\tilde{\mathbf{v}}(0, t)$ and $\tilde{\mathbf{v}}(L, t)$. The coefficient matrices and functions of the linear p.d.e. system are denoted with a bar to indicate that it originates from the linearization.

The dynamics are described by a linear combination of the state, its gradient and curvature, including the coefficients that vary spatially,

$$\tilde{\mathbf{v}}_t = \partial_x (\bar{\Sigma}(x)\tilde{\mathbf{v}}_x) + \bar{\Phi}(x)\tilde{\mathbf{v}}_x + \bar{\Lambda}(x)\tilde{\mathbf{v}} \quad (3.19)$$

with linear state vector $\tilde{\mathbf{v}} = \tilde{\mathbf{v}}(x, t)$

$$\tilde{\mathbf{v}}(x, t) = \begin{bmatrix} \tilde{n}(x, t) \\ \tilde{T}(x, t) \\ \tilde{Z}(x, t) \end{bmatrix}. \quad (3.20)$$

The 3×3 matrices contain the spatially-varying coefficients, which are diffusion coefficients $\bar{\sigma}_{ij}(x)$ in $\bar{\Sigma}(x)$, advection coefficients $\bar{\phi}_{ij}(x)$ in $\bar{\Phi}(x)$ and reaction coefficients $\bar{\lambda}_{ij}(x)$ in $\bar{\Lambda}(x)$ for $1 \leq i, j \leq 3$,

$$\bar{\Sigma}(x) = \begin{bmatrix} \bar{\sigma}_{11}(x) & \bar{\sigma}_{12}(x) & \bar{\sigma}_{13}(x) \\ \bar{\sigma}_{21}(x) & \bar{\sigma}_{22}(x) & \bar{\sigma}_{23}(x) \\ \bar{\sigma}_{31}(x) & \bar{\sigma}_{32}(x) & \bar{\sigma}_{33}(x) \end{bmatrix} = \begin{bmatrix} D(\bar{Z}_x) & 0 & F(\bar{Z}_x)\bar{n}_x \\ 0 & \frac{D(\bar{Z}_x)}{\zeta} & \frac{F(\bar{Z}_x)\bar{T}_x}{\zeta} \\ 0 & 0 & \frac{\mu(D(\bar{Z}_x) + F(\bar{Z}_x)\bar{Z}_x)}{\varepsilon} \end{bmatrix} \quad (3.21)$$

$$\bar{\Phi}(x) = \begin{bmatrix} \bar{\phi}_{11}(x) & \bar{\phi}_{12}(x) & \bar{\phi}_{13}(x) \\ \bar{\phi}_{21}(x) & \bar{\phi}_{22}(x) & \bar{\phi}_{23}(x) \\ \bar{\phi}_{31}(x) & \bar{\phi}_{32}(x) & \bar{\phi}_{33}(x) \end{bmatrix} = \begin{bmatrix} 0 & 0 & 0 \\ \left(\frac{\zeta+1}{\zeta}\right)\frac{D(\bar{Z}_x)\bar{T}_x}{\bar{n}} & \left(\frac{\zeta+1}{\zeta}\right)\frac{D(\bar{Z}_x)\bar{n}_x}{\bar{n}} & \left(\frac{\zeta+1}{\zeta}\right)\frac{F(\bar{Z}_x)\bar{n}_x\bar{T}_x}{\bar{n}} \\ \frac{c_n\bar{T}}{\varepsilon\bar{n}^2} & \frac{c_T}{\varepsilon\bar{n}} & 0 \end{bmatrix} \quad (3.22)$$

$$\bar{\Lambda}(x) = \begin{bmatrix} \bar{\lambda}_{11}(x) & \bar{\lambda}_{12}(x) & \bar{\lambda}_{13}(x) \\ \bar{\lambda}_{21}(x) & \bar{\lambda}_{22}(x) & \bar{\lambda}_{23}(x) \\ \bar{\lambda}_{31}(x) & \bar{\lambda}_{32}(x) & \bar{\lambda}_{33}(x) \end{bmatrix} = \begin{bmatrix} 0 & 0 & 0 \\ -\left(\frac{\zeta+1}{\zeta}\right)\frac{D(\bar{Z}_x)\bar{n}_x\bar{T}_x}{\bar{n}^2} & 0 & 0 \\ -\left(\frac{c_T\bar{T}_x}{\varepsilon\bar{n}^2} + \frac{2c_n\bar{n}_x\bar{T}}{\varepsilon\bar{n}^3}\right) & \frac{c_n\bar{n}_x}{\varepsilon\bar{n}^2} & \frac{b-3(Z_S-\bar{Z})^2}{\varepsilon} \end{bmatrix} \quad (3.23)$$

Note that the matrices are defined for an arbitrary solution of the nonlinear p.d.e. system. The functions $D(\bar{Z}_x)$ and $F(\bar{Z}_x)$ specify the diffusivity function and its derivative with respect to the argument \bar{Z}_x ,

which are denoted in (3.24) and (3.25), respectively.

$$D(\bar{Z}_x) = D_{\min} + \frac{D_{\max} - D_{\min}}{1 + \alpha (\bar{Z}_x)^2}, \quad (3.24)$$

$$F(\bar{Z}_x) = -\frac{2\alpha (D_{\max} - D_{\min}) \bar{Z}_x}{(1 + \alpha (\bar{Z}_x)^2)^2}. \quad (3.25)$$

The boundary conditions are obtained from equations (B.10) and (B.11) derived in Appendix B. In (3.26), the model parameters \bar{e}_i represent the s.o.l. decay lengths of the plasma variables. This notation is used to distinguish between the length scales and the reaction coefficients λ_{ij} in $\Lambda(x)$.

$$\tilde{\mathbf{v}}_x(0, t) = \bar{E}\tilde{\mathbf{v}}(0, t) \quad (3.26)$$

$$\bar{E} = \begin{bmatrix} \bar{e}_1 & 0 & 0 \\ 0 & \bar{e}_2 & 0 \\ 0 & 0 & \bar{e}_3 \end{bmatrix} := \begin{bmatrix} \frac{1}{\lambda_n} & 0 & 0 \\ 0 & \frac{1}{\lambda_T} & 0 \\ 0 & 0 & \frac{1}{\lambda_Z} \end{bmatrix} \quad (3.27)$$

The boundary condition at the plasma core side is defined in a matrix format (3.28) such that the contributions from the perturbed state via \bar{B}_1 and actuation input (vector) $\tilde{\mathbf{u}}^\top(t) = [\tilde{\Gamma}_c(t), \tilde{q}_c(t)]$ via \bar{B}_2 are separated.

$$\tilde{\mathbf{v}}_x(L, t) = \bar{B}_1 \tilde{\mathbf{v}}(L, t) + \bar{B}_2 \tilde{\mathbf{u}}(t) \quad (3.28)$$

$$\bar{B}_1 = \begin{bmatrix} 0 & 0 & 0 \\ -\frac{\bar{T}_x(L)}{\bar{n}(L)} & \frac{\zeta \bar{\Gamma}_c}{D_{\max} \bar{n}(L)} & 0 \\ 0 & 0 & 0 \end{bmatrix}, \quad \bar{B}_2 = \begin{bmatrix} -\frac{1}{D_{\max}} & 0 \\ \frac{\zeta \bar{T}(L)}{D_{\max} \bar{n}(L)} & -\frac{\zeta(\gamma-1)}{D_{\max} \bar{n}(L)} \\ 0 & 0 \end{bmatrix} \quad (3.29)$$

As can be seen from (3.28), the actuation parameters $\tilde{\Gamma}_c(t)$ and $\tilde{q}_c(t)$ are contained in the first and second entry of the boundary condition $\tilde{\mathbf{v}}_x(L, t)$. The absolute value of diffusion, advection and reaction coefficients are depicted, respectively, in Figure 3.9, Figure 3.11 and Figure 3.13 near the scrape-off layer. This is because the functions vary significantly near the separatrix and around the e.t.b. Also, the coefficients are shown with sign in Figure 3.10, Figure 3.12 and Figure 3.14. The equilibrium solution of nominal plant \mathcal{P}_1 is used for computation.

3.3.2 Constraints

The backstepping transformation of Vazquez and Krstic [78] applies to linear diffusion-advection-reaction systems of size n and forms the backbone of the controller design for the linear p.d.e. system (3.19). The linear p.d.e. system contains square spatially-dependent matrices of size $n = 3$. However, the backbone backstepping method is restricted to uncoupled diffusive processes, whereas the linear system diffusion matrix $\bar{\Sigma}(x)$ contains off-diagonal terms due to the electric field dependent diffusivities. Therefore, the diffusion matrix of the linear system is factorized using the eigendecomposition

$$\bar{\Sigma}(x) = Q(x)R(x)Q^{-1}(x), \quad (3.30)$$

with eigenvalue matrix $R(x)$, eigenvector matrix $Q(x)$ and its inverse $Q^{-1}(x)$, respectively:

$$R(x) = \begin{bmatrix} \bar{\sigma}_{11}(x) & 0 & 0 \\ 0 & \bar{\sigma}_{22}(x) & 0 \\ 0 & 0 & \bar{\sigma}_{33}(x) \end{bmatrix}, \quad Q(x) = \begin{bmatrix} 1 & 0 & -\frac{\bar{\sigma}_{13}(x)}{\bar{\sigma}_{11}(x) - \bar{\sigma}_{33}(x)} \\ 0 & 1 & -\frac{\bar{\sigma}_{23}(x)}{\bar{\sigma}_{22}(x) - \bar{\sigma}_{33}(x)} \\ 0 & 0 & 1 \end{bmatrix}. \quad (3.31)$$

Hereto, each component of the advection and reaction matrices (of the reference system) gains an additional contribution by virtue of this decomposition.

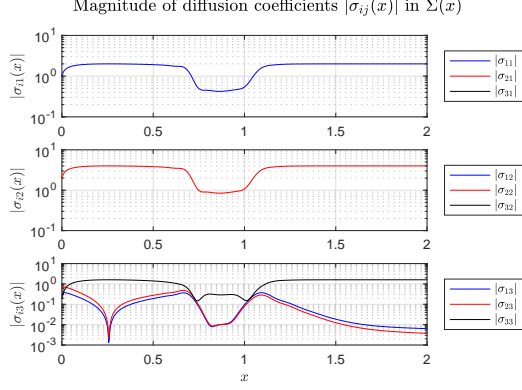


Figure 3.9: Diffusivities $\sigma_{ii}(x) \approx D_{\min}$ around the e.t.b. and decreases also significantly towards the separatrix ($x = 0$).

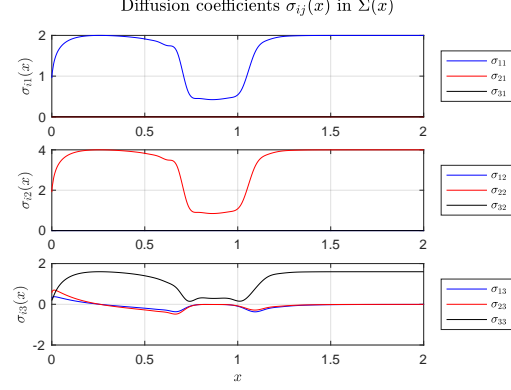


Figure 3.10: Off-diagonal diffusivities $\sigma_{i \neq j}(x)$ change sign at the minimum of the electric field profile (bottom plot).

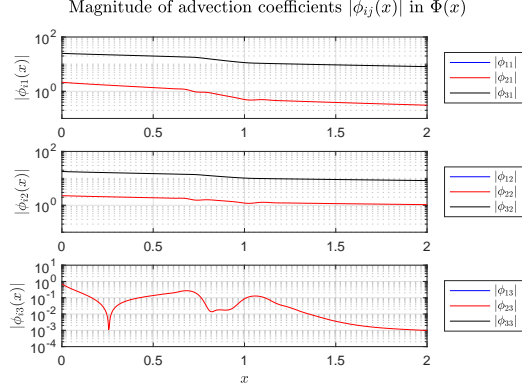


Figure 3.11: Advection coefficients affected by density and temperature perturbations behave similarly (top/middle plot).

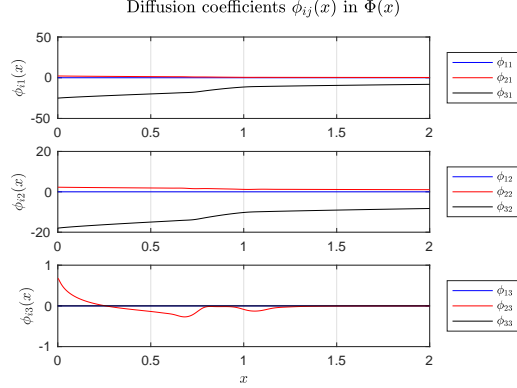


Figure 3.12: $\phi_{23}(x)$ influences T_t due to electric field perturbations (bottom plot), which behaves similarly as the off-diagonal diffusivities $\sigma_{i \neq j}(x)$.

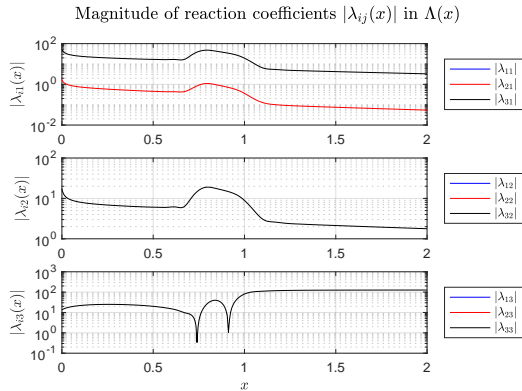


Figure 3.13: Reactivity due to density/temperature perturbations (top/middle plot) increases around the e.t.b., whereas $\lambda_{33}(x)$ (bottom plot) changes sign around e.t.b.

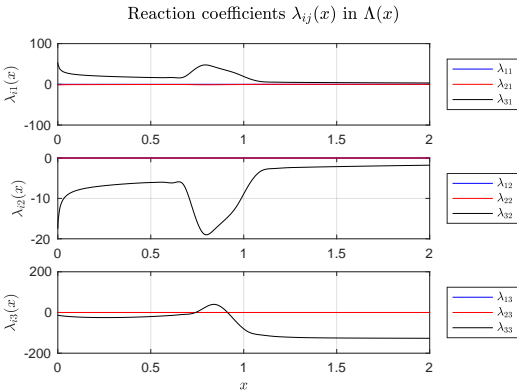


Figure 3.14: Density reactivity is always positive for T_t (top plot), while $\lambda_{33}(x)$ is positive only at the e.t.b. (bottom plot). Temperature perturbations affect Z_t negatively (middle plot).

3.4 Reference p.d.e. system

3.4.1 State transformation

The linear p.d.e. system (3.19) has been factorized using the eigendecomposition (3.30), because the interpretation of the boundary conditions resulting from the backstepping transformation is greatly simplified. Yet the system of p.d.e. needs to be further developed to obtain the general form (3.19). Therefore, the factorization of $\bar{\Sigma}(x)$ (3.30) is now substituted into the linear p.d.e. system such that

$$\tilde{\mathbf{v}}_t = \partial_x (Q(x)\Sigma(x)Q^{-1}(x)\tilde{\mathbf{v}}_x) + \bar{\Phi}(x)\tilde{\mathbf{v}}_x + \bar{\Lambda}(x)\tilde{\mathbf{v}} \quad (3.32)$$

with the (diagonal) diffusion matrix:

$$\Sigma(x) = R(x). \quad (3.33)$$

As aforementioned, the aim of this transformation is to retain only the diagonal diffusion matrix within the partial derivative (diffusion) term. Therefore, the reference state \mathbf{v} and linear state $\tilde{\mathbf{v}}$ are coupled via the eigenvector matrix $Q(x)$ yielding (3.34)–(3.35).

$$\mathbf{v} = Q^{-1}(x)\tilde{\mathbf{v}} \iff \tilde{\mathbf{v}} = Q(x)\mathbf{v} \quad (3.34)$$

$$\mathbf{v}_x = Q_x^{-1}(x)\tilde{\mathbf{v}} + Q^{-1}(x)\tilde{\mathbf{v}}_x \iff \tilde{\mathbf{v}}_x = Q(x)(\mathbf{v}_x - Q_x^{-1}(x)Q(x)\mathbf{v}) \quad (3.35)$$

The spatial derivatives of $Q(x)$, up to second-order, are derived explicitly in Appendix C and depicted for the nominal plant equilibrium. In Figure 3.15, the coefficient functions $q^{i3}(x)$, first-order spatial derivatives $q_x^{i3}(x)$ and second-order spatial derivatives $q_{xx}^{i3}(x)$ of $Q(x)$ are depicted near the plasma edge $x = [0, 2]$. As can be seen from the figure, the spatial behavior of $Q_x(x)$ and $Q_{xx}(x)$ is localized to the transport barrier region, i.e., about $x \approx 1$. Figure 3.16 shows the spatial derivatives of the nominal plant solution (H-mode) $\mathbf{v}(x)$ up to third-order.

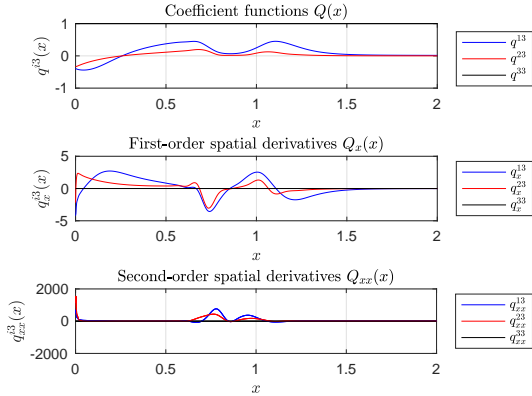


Figure 3.15: Q , Q_x and Q_{xx} for $x = [0, 2]$.

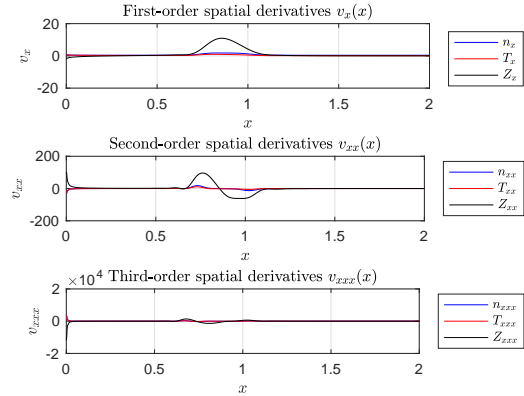


Figure 3.16: Derivatives of $\mathbf{v}(x)$ for $x = [0, 2]$.

The diffusion term of (3.32) is now treated separately. Substituting (3.35) for $\tilde{\mathbf{v}}_x$ and extracting \mathbf{v} from the brackets results in a diffusive and advective contribution (3.36).

$$\begin{aligned} \partial_x (Q(x)\Sigma(x)Q^{-1}(x)\tilde{\mathbf{v}}_x) &= \partial_x (Q(x)\Sigma(x)(\mathbf{v}_x - Q_x^{-1}(x)Q(x)\mathbf{v})) \\ &= Q(x)\partial_x (\Sigma(x)\mathbf{v}_x) + Q_x(x)\Sigma(x)\mathbf{v}_x \\ &\quad - \partial_x (Q(x)\Sigma(x)Q_x^{-1}(x)Q(x))\mathbf{v} - Q(x)\Sigma(x)Q_x^{-1}(x)Q(x)\mathbf{v}_x \end{aligned} \quad (3.36)$$

Before reinserting this result, the transformation to the reference system is completed by substituting (3.34) and (3.35) for $\tilde{\mathbf{v}}$ and $\tilde{\mathbf{v}}_x$ into (3.32), respectively, using $\tilde{\mathbf{v}}_t = Q(x)\mathbf{v}_t$.

$$Q(x)\mathbf{v}_t = \partial_x (Q(x)\Sigma(x)Q^{-1}(x)\tilde{\mathbf{v}}_x) + \bar{\Phi}(x)Q(x)(\mathbf{v}_x - Q_x^{-1}(x)Q(x)\mathbf{v}) + \bar{\Lambda}(x)Q(x)\mathbf{v} \quad (3.37)$$

Multiplying both sides of (3.37) by $Q^{-1}(x)$ and reinserting the expression found for the diffusion term (3.36) into (3.37) completes the development of the reference p.d.e. (3.38).

$$\begin{aligned} \mathbf{v}_t &= \partial_x (\Sigma(x)\mathbf{v}_x) + Q^{-1}(x) (Q_x(x)\Sigma(x) - Q(x)\Sigma(x)Q_x^{-1}(x)Q(x) + \bar{\Phi}(x)Q(x)) \mathbf{v}_x \\ &\quad + Q^{-1}(x) (-\partial_x (Q(x)\Sigma(x)Q_x^{-1}(x)Q(x)) - \bar{\Phi}(x)Q(x)Q_x^{-1}(x)Q(x) + \bar{\Lambda}(x)Q(x)) \mathbf{v}. \end{aligned} \quad (3.38)$$

The reference p.d.e. is denoted in a fashion similar to (3.19), which is described in § 3.3. Using this general form, the reference p.d.e. is expressed as

$$\mathbf{v}_t = \partial_x (\Sigma(x)\mathbf{v}_x) + \Phi(x)\mathbf{v}_x + \Lambda(x)\mathbf{v}, \quad (3.39)$$

with coefficient matrices

$$\Phi(x) = Q^{-1}(x) (Q_x(x)\Sigma(x)Q^{-1}(x) - Q(x)\Sigma(x)Q_x^{-1}(x) + \bar{\Phi}(x)) Q(x), \quad (3.40)$$

$$\Lambda(x) = Q^{-1}(x) (-\partial_x (Q(x)\Sigma(x)Q_x^{-1}(x)Q(x)) - \bar{\Phi}(x)Q(x)Q_x^{-1}(x)Q(x) + \bar{\Lambda}(x)Q(x)), \quad (3.41)$$

which depend on $R(x)$, $Q(x)$, $\bar{\Phi}(x)$ and $\bar{\Lambda}(x)$, which are denoted in equations (3.31) and (3.22)-(3.23), respectively. Using the state transformation (3.34)-(3.35), the boundary conditions of the linear p.d.e. system (3.26) and (3.28) are translated to the reference system

$$\begin{aligned} \mathbf{v}_x(0, t) &= Q_x^{-1}(0)\tilde{\mathbf{v}}(0, t) + Q^{-1}(0)\bar{E}\tilde{\mathbf{v}}(0, t) \\ &= (Q_x^{-1}(0)Q(0) + Q^{-1}(0)\bar{E}Q(0)) \mathbf{v}(0, t) := E\mathbf{v}(0, t) \end{aligned} \quad (3.42)$$

$$\begin{aligned} \mathbf{v}_x(L, t) &= Q_x^{-1}(L)\tilde{\mathbf{v}}(L, t) + Q^{-1}(L)\tilde{\mathbf{v}}_x(L, t) \\ &= Q^{-1}(L) (\bar{B}_1 Q(L)\mathbf{v}(L, t) + \bar{B}_2 \tilde{\mathbf{u}}(t)) := \bar{B}_1 \mathbf{v}(L, t) + \bar{B}_2 \tilde{\mathbf{u}}(t), \end{aligned} \quad (3.43)$$

where $\sigma_{i3}(x) \propto F(\bar{Z}_x) \propto \bar{Z}_x$ (3.25) and $\bar{Z}_x = 0$ (s.o.l. boundary condition) imply that $\lim_{x \rightarrow L} Q(x) = Q^{-1}(x) = I_{3 \times 3}$ and $\lim_{x \rightarrow L} Q_x(x) = Q_x^{-1}(x) = 0_{3 \times 3}$.

Description 2. Let $x, t \in \Omega$. The reference system contains the set of coupled reference p.d.e. (3.39) with state $\mathbf{v}(x, t)$ and boundary conditions $\mathbf{v}_x(0, t)$ (3.42) and $\mathbf{v}_x(L, t)$ (3.43). The coefficient matrices and functions are now denoted without a bar to distinguish from the linear p.d.e. system. Note that the same symbols are used, because the dynamical meaning of the terms remains identical.

For insight in the matrices, the coefficient functions of the reference system are shown $\forall x = [0, L]$ in Figure 3.17, Figure 3.19 and Figure 3.21. The behavior of the functions near the plasma scrape-off layer is displayed in Figure 3.18, Figure 3.20 and Figure 3.22. The change of coefficient values of $\Phi(x)$ and $\Lambda(x)$ is now more localized to the transport barrier, i.e., about $x \approx 1$, due to the eigendecomposition of the linear system diffusion matrix $\bar{\Sigma}(x)$. This leads to an additional advective contribution in $\phi_{ij}(x)$, which is proportional to $Q(x)$ for $1 \leq j \leq 2 \cup i = j = 3$ and $Q_x(x)$ for $1 \leq i \leq 2, j = 3$. The extra reactive contribution is due to the diffusion matrix $\Sigma(x)$ and advection term $\bar{\Phi}(x)$, which result in a leading order contribution in $\lambda_{ij}(x)$ from $Q(x)$ for $1 \leq j \leq 2$, $Q_x(x)$ for $i = j = 3$ and $Q_{xx}(x)$ for $1 \leq i \leq 2, j = 3$.

3.4.2 Constraints

Though Vazquez and Krstic [78] confine their system to the assumption $\sigma_{ii}(x) > \sigma_{ii+1}(x) > 0$ for $1 \leq i \leq n-1$, Baccoli et al. [2] state that their kernel problem remains ill-posedness unless more limiting constraints are applied. To trivialize one of the kernel conditions, an additional constraint is explored that assumes the diffusivity coefficients strictly equal such that $\sigma_{ii}(x) = \sigma(x)$ for $1 \leq i \leq n$, for some $\sigma(x) > 0$. It is possible to perform a transformation that equalizes the diffusivity coefficients in the reference (and linear) system. However, this transformation enters the backstepping design as well and does not lead to a simplification of the boundary conditions.

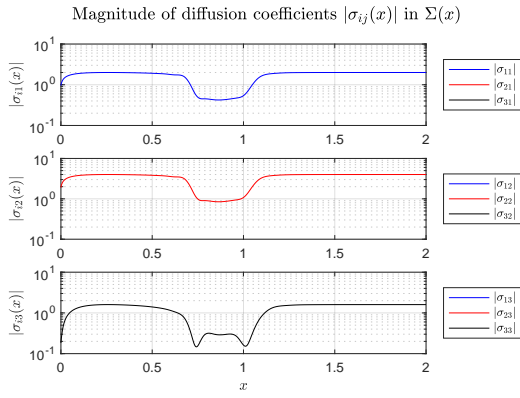


Figure 3.17: Diffusion coefficients $|\sigma_{ii}(x)|$ are identical to the linear system $\bar{\sigma}_{ii}(x)$.

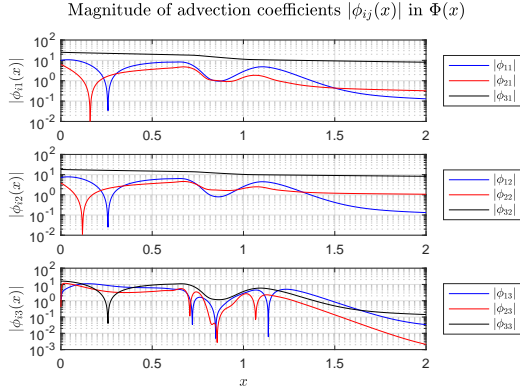


Figure 3.19: There are advective contributions that arise from the eigendecomposition affecting the density and temperature (top/middle plot).

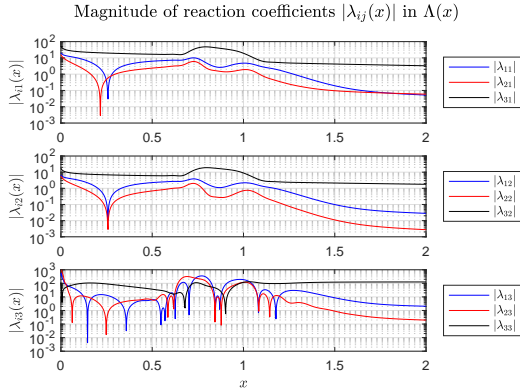


Figure 3.21: The coefficients $\lambda_{31/32}(x)$ behave similarly to the linear system coefficients, while other coefficients are dominated by eigendecomposition contributions.

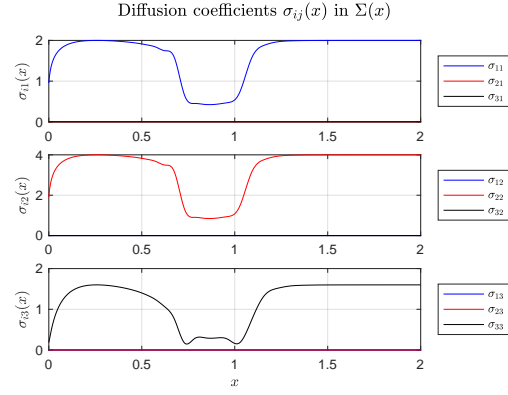


Figure 3.18: Diffusivities are positive for the whole domain, but the changing behavior is located to the edge region.

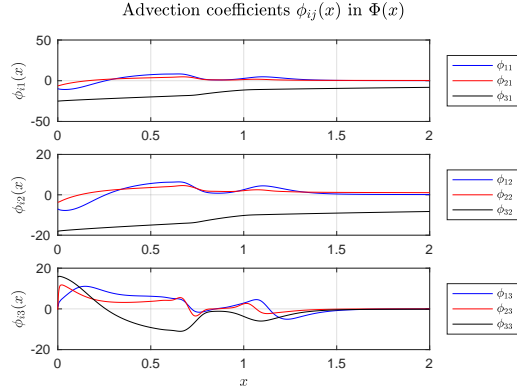


Figure 3.20: The advection coefficients affecting Z_t (bottom plot) change about four orders of magnitude between the e.t.b. region and separatrix.

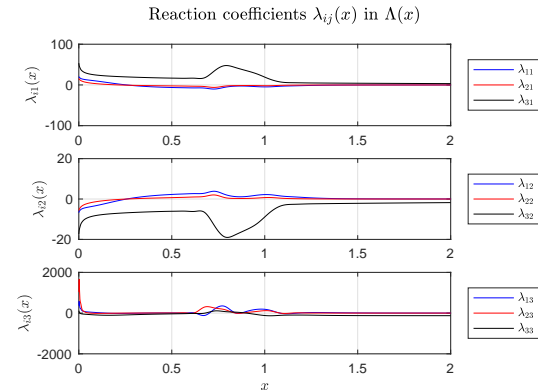


Figure 3.22: On top of the order of the magnitude spatial variation, there are coefficients that change sign once or multiple times.

3.5 Target p.d.e. system

3.5.1 Definition

The backstepping procedure takes off with the definition of a so-called target system. This system should result from a Volterra transformation, which maps the reference system into the target system. When the transformation map is known, the functions at the actuation boundary can be used as a control law. This control law then ensures that the reference system exhibits the same dynamics as the target system.

Description 3. Let $x, t \in \Omega$. The target system contains the set of coupled target p.d.e. (3.49) with state $\mathbf{w}(x, t)$ and boundary conditions $\mathbf{w}_x(0, t)$ and $\mathbf{w}_x(L, t)$. The boundary conditions are determined from the backstepping design and/or stability analysis. The coefficient matrices and functions are denoted in the same fashion as for the reference p.d.e. system.

Therefore, the definition of a suitable target system is key to the design of a backstepping boundary controller. The target system state is denoted by the vector $\mathbf{w}(x, t)$

$$\mathbf{w}(x, t) = \begin{bmatrix} w_1(x, t) \\ w_2(x, t) \\ w_3(x, t) \end{bmatrix}. \quad (3.44)$$

For the reference system (3.39), the diffusion matrix is positive definite on the whole domain for all times, because the diffusivity coefficient $\sigma_{ij}(x) > 0, \forall (x, t)$ with $1 \leq i = j \leq 3$. This is because the coefficients are proportional to the diffusivity function $D(\cdot) \geq D_{\min} > 0, \forall (x, t)$. The diffusive term effectively spreads any fluctuation in space such that the profiles converge to a smooth solution. In other words, the second-order differential operator leads to a stable contribution to the system dynamics, if the fluctuations or disturbances are sufficiently small. We choose the diffusion matrix equal to one in the reference system, which implies that the map

$$\partial_x (\Sigma(x)\mathbf{v}_x) \mapsto \partial_x (\Sigma(x)\mathbf{w}_x) \quad (3.45)$$

carries the parabolic character over to the target system. The advection term is more complicated to analyze, because the advection matrix leads to a fully-coupled system. For this model, the coupling seems to vanish in the limit of $x \rightarrow \infty$, i.e. towards the plasma core, when the matrix components vanish $\lim_{x \rightarrow 0} \phi_{ij} = \lim_{x \rightarrow 0} \lambda_{ij} = 0$ (see Figure 3.19 and Figure 3.21). However, this merely indicates the validity region of the model and not a true physical decoupling of the states. Therefore, the advection term of the target system is defined such that

$$\Phi(x)\mathbf{v}_x \mapsto \Psi(x)\mathbf{w}_x, \quad (3.46)$$

where $\Psi(x)$ is determined during the backstepping transformation and stability analysis. It should be noted that, in [78], an additional advection term is added to their target system that depends on the boundary condition at $x = 0$. This extra advection term includes a lower triangular matrix $G(x)$ that acts on the scrape-off layer boundary only: $-G(x)\mathbf{w}_x(0, t)$. This transforms the boundary condition into a cascade system (at $x = 0$), where each consecutive boundary condition depends on the former boundary condition(s) and the corresponding gradient. To include this freedom, we implement an equivalent (additional) advection term that acts on the s.o.l. boundary condition:

$$H(x)\mathbf{w}_x(0, t). \quad (3.47)$$

The coefficient functions $h_{ij}(x)$ are determined further on, but assume these are nonzero for now. A similar transformation on the target boundary conditions is done in the nonlinear o.d.e. backstepping designs of [18, 63]. Despite the stabilizing boundary condition in their target system, it is not necessary to include it in the partial differential equations due to the character of their method.

The reaction term is replaced by a damping matrix $\Theta(x)$. This choice is equivalent to [18], [63] and [78], where the separate reaction contributions of each state are decoupled. So, the reaction matrix should be transformed into a stabilizing contribution such that:

$$\Lambda(x)\mathbf{v}(x, t) \mapsto \Theta(x)\mathbf{w}(x, t). \quad (3.48)$$

This effectively resembles a translation of the (real part of the) eigenvalues of the system. Using the mappings (3.45)–(3.48), the target p.d.e. is defined by:

$$\mathbf{w}_t = \partial_x (\Sigma(x)\mathbf{w}_x) + \Psi(x)\mathbf{w}_x + \Theta(x)\mathbf{w}(x, t) + H(x)\mathbf{w}_x(0, t) \quad (3.49)$$

with $\Sigma(x)$ (3.33) from the reference system. Coefficient bounds θ_* , ψ_* and h_* on $\theta_{ij}(x)$, $\psi_{ij}(x)$ and $h_{ij}(x)$, respectively, are derived during the stability analysis in § 4.2.2. This guarantees the stability of the target system, when the coefficients are chosen in compliance with the stable parameter range.

3.5.2 Constraints

Before the backstepping design is introduced, it is important to note some generic issues associated with the backstepping transformation. The backstepping design yields a two-dimensional hyperbolic p.d.e. system, which can be solved to find the so-called kernel functions, i.e. $k_{ij}(x, \xi)$ for $1 \leq i, j \leq n$. These kernel functions eventually determine the boundary controller for the original system. However, the well-posedness of the kernel problem depends on the resulting (kernel) conditions. To avoid ill-posedness, the diffusion matrix in the reference system has been diagonalized. Furthermore, we mention optional constraints that can be applied to the target system or kernel matrix shortly, which are obtained from backstepping literature [1, 2, 78, 79].

In [2], an additional constraint is enforced to the kernel matrix. This constraint is very limiting, because it assumes that the transformation can be performed by a scalar kernel function. This has an impact on the class of possible target systems, since it allows only two boundary conditions. Although the problematic boundary condition is automatically satisfied $\forall k(x, \xi)$, the other boundary conditions present further limitations. For example, this constraint restricts the form of the damping term that can be chosen in [2]. For the constant coefficient kernel problem in [2], the constraint leads to a requirement on the damping matrix C with constant γ^* to be determined from stability considerations:

$$C := (\gamma^*\Sigma - \Lambda) \quad (3.50)$$

In [78, 79], the researchers follow a different approach to avoid ill-posedness of their kernel problem. A second advection term is introduced in their target system that provides additional freedom in the kernel problem. The additional freedom reduces the number of boundary conditions by $(n^2 - n)/2$ for the lower triangular form considered in [78]:

$$-G(x)\mathbf{w}_x(0, t), \quad \text{with} \quad g_{ij}(x) = \begin{cases} g_{ij}(x) & \text{for } i > j \\ 0 & \text{for } i \leq j \end{cases}. \quad (3.51)$$

It should be noted that this type of p.d.e. is not common in the literature. This is because the (extra) advection term depends on the state evaluated at a single spatial point $\mathbf{w}_x(0, t)$, whereas the other terms operate on the infinite-dimensional vector $\mathbf{v}(x, t)$. We also introduce this freedom into our target system, the necessity of which becomes clear in Chapter 4.

3.6 Discussion

The lack of experimental validation is a vast shortcoming for control design as there exists at least three keys to defining the control objective soundly. One is the estimation of parametric model uncertainties. Through the physics-based derivation of the electric field equation, it can be seen that there are additional

nonlinearities. The thermodynamic coefficients and viscosity are also functionally dependent on the state variables. This shows that there are two types of parametric uncertainty, one of which is state-dependent. The other uncertainty arises from the plasma parameters, which have been taken for a typical operational scenario in JET. Definition of the control objective would benefit from system identification; specifically, the observation of model parameters could even be the control objective.

As a second key, qualification of the class of disturbances may lead to more insight in the applicable area of control theory. Thirdly, the examination of engineering requirements such as real-time applicability or compatibility to diagnostics could be taken into account. However, we focused the control objective on model uncertainty, which is believed to constitute the major challenge in control of the H-L bifurcation.

Several constraints have arisen as a result of the linearization and choice of control design method. The constraints are briefly listed:

- Coupled diffusive processes arise from the electric field-dependent diffusivities and complicate the backstepping design. Hence, the system is factorized using an eigendecomposition at the cost of introducing additional advective/reactive couplings.
- Distinct diffusive processes do not allow for further simplification as opposed to the case of Baccelli et al. [1].
- The target system requires additional degrees of freedom, which can be implemented by adding a boundary advection term.

The consequences of the constraints follow from the backstepping transformation in the following chapter.

Chapter 4

Boundary control

The backstepping design procedure is exploited to design a stabilizing boundary feedback control based on the linear p.d.e. system dynamics. The goal of the control design is to obtain a boundary feedback control that stabilizes the linear system with a mismatch in model parameter(s). This means that the mismatched system features a different equilibrium and the feedback control should guarantee convergence to the original equilibrium.

The design problem defines an integral transformation for a set of kernel functions in § 4.1, of which the aim is to transform the reference p.d.e. system § 3.4 into a stable target p.d.e. system § 3.5. The kernel problem is derived from this integral transformation and requires a thorough analysis to define a feasible system of p.d.e. in § 4.2. The solution of the kernel system is obtained in § 4.3, which is used to compute the boundary feedback control. A discussion of the complications that arise from the method follows in § 4.4.

4.1 Backstepping transformation

The backstepping procedure for a spatially-varying linear p.d.e. system from Vazquez and Krstic [78] forms the backbone of the boundary control design. However, the general procedure of backstepping is first explained using the heat equation as an elementary example in § 4.1.1. The backstepping design for the linear p.d.e. system is introduced in § 4.1.2, where we describe the transformation and context. The integral transformation is then used to derive the kernel equation in § 4.1.3, which contains a set of p.d.e. and conditions. This is used to formulate the kernel p.d.e. system in § 4.1.4.

4.1.1 An elementary example

The backstepping design is explained for clarity and overview using the heat equation as an elementary example. This is because it resembles the main processes involved in the reference p.d.e. system described in § 3.4. Throughout this subsection, we refer to the boundary control design for the actual system that contains three coupled p.d.e. and spatially-varying coefficients. In analogy to the actual system we want to control, the original heat equation/reference system is denoted by $v(x, t)$ and the target system state is called $w(x, t)$. The backstepping design aims to find a kernel function $k(x, \xi)$ that maps the reference system into the target system. Because the backstepping transformation is invertible, the kernel function can be used for the control law transferring the desired target dynamics to the reference system.

Consider the well-known heat equation including a reaction term on an one-dimensional domain,

$$v_t = v_{xx} + \lambda v, \quad (4.1)$$

with state $v(x, t)$ and λ an arbitrary (reaction) parameter. We deploy an homogeneous boundary condition at $x = 0$ and define the actuation input $U(t)$ at the other end of the domain:

$$v(0, t) = 0, \quad v(1, t) = u(t). \quad (4.2)$$

Stability of the heat equation can be easily assessed using the direct Lyapunov method. The main idea is to find an energy functional $V(x, t)$ that implies $V(x, t) \geq 0$ and $\dot{V}(x, t) \leq 0$ for the domain, where the equality holds only at an equilibrium. If such a functional can be found, the system is asymptotically stable. A candidate Lyapunov functional can be written as,

$$V(x, t) = \frac{1}{2} \int_0^1 w^2 \, dx, \quad (4.3)$$

which is positive semi-definite $\forall x, t$. The time derivative can be computed along an arbitrary solution of (4.1):

$$V_t = \int_0^1 w w_t \, dx = \int_0^1 w [w_{xx} + \lambda w] \, dx = [ww_x]_0^1 - \int_0^1 w_x^2 \, dx + \lambda \int_0^1 w^2 \, dx \quad (4.4)$$

It can be seen that the diffusive contribution is stable for homogeneous boundary conditions $w(0, t) = w(1, t) = 0$ (i.e., $u(t) = 0$). Furthermore, the contribution from the reactive term is stable for $\lambda \leq 0$ indicating damping, but unstable for $\lambda > 0$. This excisition is also used to find conditions for stability of the reference p.d.e. system in § 4.2.2.

Let us assume that λ is indeed sufficiently large and positive. Then the goal of the backstepping transformation is to eliminate or compensate for the unstable reaction. This is formalized by definition of the so-called target system, e.g.,

$$w_t = w_{xx} - cw, \quad (4.5)$$

which features the desired system behavior for $c \geq 0$ and boundary conditions:

$$w(0, t) = 0, \quad w(1, t) = 0. \quad (4.6)$$

The aim of the backstepping design procedure is to find a kernel function $k(x, \xi)$ that maps the reference system $v(x, t)$ into the target system $w(x, t)$, which is described for the actual system (L-H transition model) in § 4.1.2. This kernel function also defines the boundary feedback control, which translates the target system behavior into the closed-loop (with control input) behavior of the reference system. The kernel function $k(x, \xi)$ defines the map of the backstepping transformation,

$$w(x, t) = v(x, t) - \int_0^x k(x, \xi)v(\xi, t) \, d\xi, \quad (4.7)$$

which is a Volterra integral equation of the second kind. There are two important properties of (4.7) that should be noted:

- The integral is limited to x such that information is accumulated starting from the left-hand boundary to the right-hand boundary, where the control input is located.
- The transformation is invertible such that a stable target system implies closed-loop stability of the reference system, when the eventual boundary feedback controller is used to define $u(t)$.

The backstepping transformation (4.7) is used to find conditions that $k(x, \xi)$ should obey by substituting the transformation into the target system (this derivation is performed in § 4.1.3 for the linear p.d.e. system). The result of this substitution exercise has been obtained by Krstic [57] for $c = 0$, which is called the kernel p.d.e. system in this thesis (see § 4.1.4 for the actual kernel problem):

$$\begin{aligned} k_{xx}(x, \xi) - k_{\xi\xi}(x, \xi) &= \lambda k(x, \xi), \\ k(x, 0) &= 0, \\ k(x, x) &= -\frac{\lambda}{2}x. \end{aligned} \quad (4.8)$$

The kernel p.d.e. system defines a hyperbolic p.d.e. on the triangular (2D) domain $0 \leq \xi \leq x \leq 1$ with boundary conditions at the edges $(x, 0)$ and (x, x) . The solution can be obtained analytically using the method of successive approximations [57]:

$$k(x, \xi) = -\lambda \xi \frac{I_1(\sqrt{\lambda(x^2 - \xi^2)})}{\lambda(x^2 - \xi^2)}, \quad (4.9)$$

where I_1 is a modified first-order, first-kind Bessel function. Using the kernel solution (4.9), the boundary feedback controller follows from evaluating the backstepping transformation at $x = 1$ and substituting the boundary condition $w(1, t) = 0$,

$$\begin{aligned} w(1, t) &= v(1, t) - \int_0^1 k(1, \xi) v(\xi, t) d\xi \\ 0 &= u(t) - \int_0^1 k(1, \xi) v(\xi, t) d\xi \end{aligned} \quad (4.10)$$

such that the boundary feedback becomes:

$$u(t) = - \int_0^1 \left[\lambda \xi \frac{I_1(\sqrt{\lambda(x^2 - \xi^2)})}{\lambda(x^2 - \xi^2)} \right] v(\xi, t) d\xi. \quad (4.11)$$

The backstepping design applied to the heat equation is partly comparable to the design for the reference system/L-H transition model. However, there are important differences due to the spatially-varying coefficients and couplings between states. The differences should become clear throughout the following subsections, where the actual boundary feedback design is considered.

4.1.2 Description

The goal of the backstepping design is to find a set of functions $k_{ij}(x, \xi)$ that map the solution $\mathbf{v}(x, t)$ into $\mathbf{w}(x, t)$. Through the definition of a Volterra integral equation (of the second kind), we can formulate the backstepping problem as finding a kernel matrix $K(x, \xi)$ such that

$$\mathbf{w}(x, t) = \mathbf{v}(x, t) - \int_0^x K(x, \xi) \mathbf{v}(\xi, t) d\xi, \quad (4.12)$$

where $K(x, \xi)$ contains $N (= 9)$ kernel functions $k_{ij}(x, \xi)$ for $1 \leq i, j \leq 3$,

$$K(x, \xi) = \begin{bmatrix} k_{11}(x, \xi) & k_{12}(x, \xi) & k_{13}(x, \xi) \\ k_{21}(x, \xi) & k_{22}(x, \xi) & k_{23}(x, \xi) \\ k_{31}(x, \xi) & k_{32}(x, \xi) & k_{33}(x, \xi) \end{bmatrix}. \quad (4.13)$$

The backstepping transformation of (4.12) is defined on a two-dimensional (triangular) domain \mathcal{T} (4.14) in the (x, ξ) -plane.

$$\mathcal{T} = \{x, \xi \in \mathbb{R}^2 \mid 0 \leq \xi \leq x \leq L\}. \quad (4.14)$$

The domain is bounded by the connected edges $\delta\mathcal{T}_m$ contained in the set $\delta\mathcal{T}$ (4.15).

$$\delta\mathcal{T}_1 = \{(x, \xi) \in \mathbb{R}^2 \mid \xi = 0\}, \quad \delta\mathcal{T}_2 = \{(x, \xi) \in \mathbb{R}^2 \mid x = L\}, \quad \delta\mathcal{T}_3 = \{(x, \xi) \in \mathbb{R}^2 \mid x = \xi\}. \quad (4.15)$$

The spatial domain \mathcal{T} is shown in Figure 4.1, where the domain boundaries are indicated as well as the corresponding outward normal vectors \vec{n}_m . Furthermore, if $\mathbf{v}(x, 0)$ is the assumed initial state of

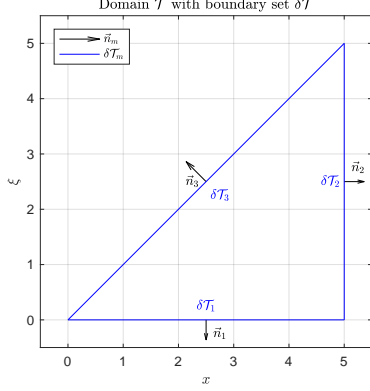


Figure 4.1: The integral transformation is defined on the (2D) spatial domain \mathcal{T} .

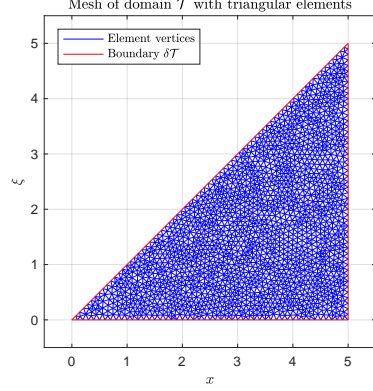


Figure 4.2: Domain \mathcal{T}_{num} is used for numerically solving the kernel problem.

the reference system, the backstepping transformation (4.12) defines the initial condition for the target system:

$$\mathbf{w}(x, 0) = \mathbf{v}(x, 0) - \int_0^x K(x, \xi) \mathbf{v}(\xi, 0) d\xi. \quad (4.16)$$

Also, it can be easily seen from (4.12) that

$$\mathbf{w}(0, t) = \mathbf{v}(0, t), \quad (4.17)$$

$$\mathbf{w}(L, t) = \mathbf{v}(L, t) - \int_0^L K(L, \xi) \mathbf{v}(\xi, t) d\xi \quad (4.18)$$

for the target system. However, the reference system includes Robin-type boundary conditions and we choose to maintain that p.d.e. system structure.

The integral transformation (4.12) is used to formulate the kernel problem. The kernel problem consists of finding a set of functions $K(x, \xi)$ that not only transform the state (\mathbf{v}), but also the temporal and spatial derivatives thereof. Due to the p.d.e. structure of the reference and target system, the kernel problem manifests a p.d.e. for the kernel functions with certain conditions that can be solved on the numerical domain \mathcal{T}_{num} depicted in Figure 4.2. The partial derivatives of the backstepping transformation are first computed from (4.12). These equations link partial derivatives of the target state \mathbf{w} to the reference state and partial derivatives, i.e., \mathbf{v} and $\mathbf{v}_{t,x,xx}$, respectively.

$$\mathbf{w}_t(x, t) = \mathbf{v}_t(x, t) - \int_0^x K(x, \xi) \mathbf{v}_t(\xi, t) d\xi \quad (4.19)$$

$$\mathbf{w}_x(x, t) = \mathbf{v}_x(x, t) - \int_0^x K_x(x, \xi) \mathbf{v}(\xi, t) d\xi - K(x, x) \mathbf{v}(x, t) \quad (4.20)$$

$$\begin{aligned} \partial_x (\Sigma(x) \mathbf{w}_x(x, t)) &= \partial_x (\Sigma(x) \mathbf{v}_x(x, t)) - \int_0^x \partial_x (\Sigma(x) K_x(x, \xi)) \mathbf{v}(\xi, t) d\xi \\ &\quad - \Sigma(x) K_x(x, x) \mathbf{v}(x, t) - \partial_x (\Sigma(x) K(x, x) \mathbf{v}(x, t)) \end{aligned} \quad (4.21)$$

Although the computations are mostly straightforward, the diffusion term (4.21) has been calculated using (4.20) and the product rule such that

$$\partial_x \left(\Sigma(x) \int_0^x K_x(x, \xi) \mathbf{v}(\xi, t) d\xi \right) = \int_0^x \partial_x (\Sigma(x) K_x(x, \xi)) \mathbf{v}(\xi, t) d\xi + \Sigma(x) K_x(x, x) \mathbf{v}(x, t) \quad (4.22)$$

where last terms represents the derivative with respect to the integral upper limit. Evaluating (4.20) at $x = \{0, L\}$, the Robin-type boundary conditions of the reference system reveal the b.c. for the target system. This leads to the scrape-off layer b.c. at $x = 0$ formulated in terms of $\mathbf{v}(0, t)$ and $\mathbf{v}_x(0, t)$:

$$\mathbf{w}_x(0, t) = \mathbf{v}_x(0, t) - K(0, 0)\mathbf{v}(0, t). \quad (4.23)$$

Note that any condition on $K(0, 0)$ influences the s.o.l. boundary condition and stability of the target system directly. The plasma core b.c. at $x = L$ can be found also from evaluating (4.20):

$$\mathbf{w}_x(L, t) = \mathbf{v}_x(L, t) - \int_0^L K_x(L, \xi)\mathbf{v}(\xi, t) d\xi - K(L, L)\mathbf{v}(L, t). \quad (4.24)$$

This reveals the control input vector, when $\mathbf{w}_x(L, t)$ is subjected to a requirement. This concludes the description of the kernel problem, which forms the basis for deriving the kernel p.d.e. and conditions explicitly in the next section § 4.1.3.

4.1.3 Derivation

The derivation of the kernel problem allows us to formulate the integral transformation into a system of p.d.e. with conditions, which is named the kernel p.d.e. system. The idea is that this results in a mathematical problem for which approaches are available to obtain a numerical (or even analytic) solution. First, the reference p.d.e. (3.39) is used to eliminate \mathbf{v}_t in the time derivative of the backstepping transformation (4.19).

$$\begin{aligned} \mathbf{w}_t(x, t) &= \partial_x (\Sigma(x)\mathbf{v}_x(x, t)) + \Phi(x)\mathbf{v}_x(x, t) + \Lambda(x)\mathbf{v}(x, t) \\ &\quad - \int_0^x K(x, \xi) [\partial_\xi (\Sigma(\xi)\mathbf{v}_\xi(\xi, t)) + \Phi(\xi)\mathbf{v}_\xi(\xi, t) + \Lambda(\xi)\mathbf{v}(\xi, t)] d\xi \end{aligned} \quad (4.25)$$

The time derivative of the reference state is now completely eliminated. Using the definition of the target system (3.49), the time derivative of the target state can be eliminated as well.

$$\begin{aligned} \partial_x (\Sigma(x)\mathbf{w}_x(x, t)) + \Psi(x)\mathbf{w}_x(x, t) + \Theta(x)\mathbf{w}(x, t) + H(x)\mathbf{w}_x(0, t) \\ = \partial_x (\Sigma(x)\mathbf{v}_x(x, t)) + \Phi(x)\mathbf{v}_x(x, t) + \Lambda(x)\mathbf{v}(x, t) \\ - \int_0^x K(x, \xi) [\partial_\xi (\Sigma(\xi)\mathbf{v}_\xi(\xi, t)) + \Phi(\xi)\mathbf{v}_\xi(\xi, t) + \Lambda(\xi)\mathbf{v}(\xi, t)] d\xi \end{aligned} \quad (4.26)$$

The target system dynamics at the left-hand side of (4.26) are now expressed in terms of the reference system (dynamics) using the Volterra transformation (4.12) for $\mathbf{w}(x, t)$ and the spatial derivatives thereof, (4.20) and (4.21), for $\mathbf{w}_x(x, t)$ and $\partial_x (\Sigma(x)\mathbf{w}_x(x, t))$, respectively. The s.o.l. boundary condition $\mathbf{w}_x(0, t)$ is replaced by (4.23).

$$\begin{aligned} \partial_x (\Sigma(x)\mathbf{v}_x(x, t)) - \int_0^x \partial_x (\Sigma(x)K_x(x, \xi)) \mathbf{v}(\xi, t) d\xi - \Sigma(x)K_x(x, x)\mathbf{v}(x, t) - \partial_x (\Sigma(x)K(x, x)\mathbf{v}(x, t)) \\ + \Psi(x)\mathbf{v}_x(x, t) - \int_0^x \Psi(x)K_x(x, \xi)\mathbf{v}(\xi, t) d\xi - \Psi(x)K(x, x)\mathbf{v}(x, t) + \Theta(x)\mathbf{v}(x, t) \\ - \int_0^x \Theta(x)K(x, \xi)\mathbf{v}(\xi, t) d\xi + H(x)\mathbf{v}_x(0, t) - H(x)K(0, 0)\mathbf{v}(0, t) \\ = \partial_x (\Sigma(x)\mathbf{v}_x(x, t)) + \Phi(x)\mathbf{v}_x(x, t) + \Lambda(x)\mathbf{v}(x, t) \\ - \int_0^x K(x, \xi) [\partial_\xi (\Sigma(\xi)\mathbf{v}_\xi(\xi, t)) + \Phi(\xi)\mathbf{v}_\xi(\xi, t) + \Lambda(\xi)\mathbf{v}(\xi, t)] d\xi \end{aligned} \quad (4.27)$$

Clearly, the diffusion term $\partial_x(\Sigma(x)\mathbf{v}_x)$ of the reference system drops out of the equation. As an intermediate step, the first and second term of the integral in the right-hand side of (4.27) is integrated by parts such that only the reference state occurs within the integral. This facilitates further derivation of the kernel problem.

$$\begin{aligned}
 & - \int_0^x [K(x, \xi) \partial_\xi (\Sigma(\xi) \mathbf{v}_\xi(\xi, t)) + K(x, \xi) \Phi(\xi) \mathbf{v}_\xi(\xi, t)] d\xi \\
 &= - [K(x, \xi) \Sigma(\xi) \mathbf{v}_\xi(\xi, t)]_0^x + \int_0^x K_\xi(x, \xi) \Sigma(\xi) \mathbf{v}_\xi(\xi, t) d\xi \\
 &\quad - [K(x, \xi) \Phi(\xi) \mathbf{v}(\xi, t)]_0^x + \int_0^x \partial_\xi (K(x, \xi) \Phi(\xi)) \mathbf{v}(\xi, t) d\xi \\
 &= -K(x, x) \Sigma(x) \mathbf{v}_x(x, t) + K(x, 0) \Sigma(0) \mathbf{v}_x(0, t) \\
 &\quad + K_\xi(x, x) \Sigma(x) \mathbf{v}(x, t) - K_\xi(x, 0) \Sigma(0) \mathbf{v}(0, t) - \int_0^x \partial_\xi (K_\xi(x, \xi) \Sigma(\xi)) \mathbf{v}(\xi, t) d\xi \\
 &\quad - K(x, x) \Phi(x) \mathbf{v}(x, t) + K(x, 0) \Phi(0) \mathbf{v}(0, t) + \int_0^x \partial_\xi (K(x, \xi) \Phi(\xi)) \mathbf{v}(\xi, t) d\xi \quad (4.28)
 \end{aligned}$$

Substituting the intermediate result (4.28), into (4.27) leads to the kernel equation (4.29).

$$\begin{aligned}
 & - \int_0^x \partial_x (\Sigma(x) K_x(x, \xi)) \mathbf{v}(\xi, t) d\xi - \Sigma(x) K_x(x, x) \mathbf{v}(x, t) - \partial_x (\Sigma(x) K(x, x)) \mathbf{v}(x, t) \\
 & \quad \rightarrow(4.30) \qquad \qquad \qquad \rightarrow(4.32) \qquad \qquad \qquad \rightarrow(4.32) \\
 & - \Sigma(x) K(x, x) \mathbf{v}_x(x, t) + \Psi(x) \mathbf{v}_x(x, t) - \int_0^x \Psi(x) K_x(x, \xi) \mathbf{v}(\xi, t) d\xi - \Psi(x) K(x, x) \mathbf{v}(x, t) \\
 & \quad \rightarrow(4.33) \qquad \qquad \qquad \rightarrow(4.33) \qquad \qquad \qquad \rightarrow(4.32) \qquad \qquad \qquad \rightarrow(4.30) \\
 & + \Theta(x) \mathbf{v}(x, t) - \int_0^x \Theta(x) K(x, \xi) \mathbf{v}(\xi, t) d\xi + H(x) E \mathbf{v}(0, t) - H(x) K(0, 0) \mathbf{v}(0, t) \\
 & \quad \rightarrow(4.32) \qquad \qquad \qquad \rightarrow(4.31) \qquad \qquad \qquad \rightarrow(4.31) \qquad \qquad \qquad \rightarrow(4.30) \\
 & = \Phi(x) \mathbf{v}_x(x, t) + \Lambda(x) \mathbf{v}(x, t) - \int_0^x K(x, \xi) \Lambda(\xi) \mathbf{v}(\xi, t) d\xi - K(x, x) \Sigma(x) \mathbf{v}_x(x, t) + K(x, 0) \Sigma(0) E \mathbf{v}(0, t) \\
 & \quad \rightarrow(4.33) \qquad \qquad \qquad \rightarrow(4.32) \qquad \qquad \qquad \rightarrow(4.33) \qquad \qquad \qquad \rightarrow(4.31) \\
 & + K_\xi(x, x) \Sigma(x) \mathbf{v}(x, t) - K_\xi(x, 0) \Sigma(0) \mathbf{v}(0, t) - \int_0^x \partial_\xi (K_\xi(x, \xi) \Sigma(\xi)) \mathbf{v}(\xi, t) d\xi \\
 & \quad \rightarrow(4.32) \qquad \qquad \qquad \rightarrow(4.31) \qquad \qquad \qquad \rightarrow(4.30) \\
 & - K(x, x) \Phi(x) \mathbf{v}(x, t) + K(x, 0) \Phi(0) \mathbf{v}(0, t) + \int_0^x \partial_\xi (K(x, \xi) \Phi(\xi)) \mathbf{v}(\xi, t) d\xi \quad (4.29) \\
 & \quad \rightarrow(4.32) \qquad \qquad \qquad \rightarrow(4.31) \qquad \qquad \qquad \rightarrow(4.30)
 \end{aligned}$$

Note that the scrape-off layer b.c. (3.42) is introduced such that $\mathbf{v}_x(0, t)$ is replaced by $E \mathbf{v}(0, t)$. Because of the structure of (4.29), it is possible to separate the complete equation into a set of p.d.e. and boundary conditions. The undersets beneath each contribution to the kernel equation (4.29) indicate whether the term relates to the kernel p.d.e. or one of the boundary condition sets. The formulation of the kernel p.d.e. set and boundary conditions is the subject of the next section.

4.1.4 Formulation of the kernel p.d.e. system

The kernel problem is now formulated as a p.d.e. system with additional conditions that should be satisfied for any solution $\mathbf{v}(x, t)$. To find the kernel p.d.e. set, we equate the integrals that affect $\mathbf{v}(\xi, t)$. This (matrix) equation is satisfied for arbitrary solutions $\mathbf{v}(\cdot, t)$ if the arguments (under the integral)

sum to zero. So, the kernel p.d.e. defined on $(x, \xi) \in \mathcal{T}$ becomes a set of N coupled partial differential equations:

$$\begin{aligned} \partial_x (\Sigma(x)K_x(x, \xi)) - \partial_\xi (K_\xi(x, \xi)\Sigma(\xi)) + \Psi(x)K_x(x, \xi) + \partial_\xi (K(x, \xi)\Phi(\xi)) \\ - K(x, \xi)\Lambda(\xi) + \Theta(x)K(x, \xi) = 0. \end{aligned} \quad (4.30)$$

To solve (4.30) for the kernel functions $k_{ij}(x, \xi)$, we need boundary conditions that define the system at the domain boundary $\delta\mathcal{T}$ (4.15). In (4.29), there are terms including the kernel functions evaluated at $\delta\mathcal{T}_1 : (x, 0)$ and $\delta\mathcal{T}_3 : (x, x)$ that affect $\mathbf{v}(0, t)$, $\mathbf{v}(x, t)$ and $\mathbf{v}_x(x, t)$. The kernel conditions follow from collecting the foregoing terms in separate equations as well.

The first kernel condition \mathcal{K}_1 is found by equating the terms including $\mathbf{v}(0, t)$ (4.31). Kernel condition \mathcal{K}_1 constitutes a set of N Robin-type boundary conditions at $\delta\mathcal{T}_1$ containing both the outward (normal) derivative and the functions $k_{ij}(x, \xi)|_{x=0}$.

$$\mathcal{K}_1 : (-K_\xi(x, 0)\Sigma(0) + K(x, 0)(\Phi(0) + \Sigma(0)E) + H(x)(K(0, 0) - E))\mathbf{v}(0, t) = 0 \quad (4.31)$$

It should be noted that this condition is trivially satisfied in [78], because their reference system includes $\mathbf{v}(0, t) = 0$. By contrast, the bifurcation behavior at the separatrix is uttermost important for the dynamic behavior. This implies that we cannot assume that the perturbed state vanishes at $x = 0$.

Furthermore, the second kernel condition \mathcal{K}_2 arises from collecting terms affecting $\mathbf{v}(x, t)$ (4.32), which are defined on domain boundary $\delta\mathcal{T}_3$. This condition differs from the transformation in [78], since their target system does not include a designable advection matrix.

$$\begin{aligned} \mathcal{K}_2 : (\Sigma(x)K_x(x, x) + K_\xi(x, x)\Sigma(x) - K(x, x)\Phi(x) + \Psi(x)K(x, x) \\ + \frac{d}{dx}(\Sigma(x)K(x, x)) + \Lambda(x) - \Theta(x))\mathbf{v}(x, t) = 0 \end{aligned} \quad (4.32)$$

Lastly, the terms that affect $\mathbf{v}_x(x, t)$ constitute the third kernel condition \mathcal{K}_3 (4.33) at $\delta\mathcal{T}_3$. As for \mathcal{K}_3 , retaining the advection term reveals the same condition as obtained in [78].

$$\mathcal{K}_3 : (\Sigma(x)K(x, x) - K(x, x)\Sigma(x) + \Phi(x) - \Psi(x))\mathbf{v}_x(x, t) = 0 \quad (4.33)$$

In summary, the kernel conditions (4.32) and (4.33) are practically identical to those obtained in [78]. If used directly as boundary conditions, the kernel conditions specify $3N$ boundary conditions for N kernel functions in a two-dimensional domain. A solution to the kernel problem may then cease to exist, because it is overdetermined. In Appendix D, we derive the characteristic o.d.e. set corresponding to the p.d.e. problem to investigate the allowable number of boundary conditions. Analysis of the homogeneous problem indicates that only $2N$ boundary conditions are allowed, for the kernel p.d.e. set is overdetermined otherwise.

4.2 Kernel p.d.e. system

The kernel p.d.e. (4.30) and kernel conditions (4.31)–(4.33) constitute the kernel problem. The kernel conditions are interpreted in § 4.2.1 with the aim of reducing the number of conditions. As a result, we define a set of $2N$ ($N = 9$) boundary conditions that resolves the overdetermination. The kernel p.d.e. set in combination with the set of boundary conditions \mathcal{B}_1 is named the kernel p.d.e. system. A stability analysis is performed on the target p.d.e. system in § 4.2.2 to find requirements that guarantee stability.

4.2.1 Interpretation of the kernel conditions

The kernel conditions (4.31)–(4.33) yield $3N$ boundary conditions for the kernel problem, if applied directly. This shows that we need to find a set of boundary conditions called \mathcal{B}_1 that:

- (i) fully constrains the kernel p.d.e. (4.30),
- (ii) satisfies the kernel conditions \mathcal{K}_m , for $m = \{1, 2, 3\}$,
- (iii) and complies at the intersection $\delta\mathcal{T}_1 \cap \delta\mathcal{T}_3 = \{x, \xi \in \mathcal{T} \mid x = \xi = 0\}$.

This section is dedicated to finding a set of $2N$ boundary conditions that satisfy the foregoing properties. Our approach is to interpret the kernel conditions \mathcal{K}_m component-wise such that more insight into the underlying structure is obtained.

Kernel condition 1

Due to $H(x)\mathbf{w}_x(0, t)$ in the target system, the unknown functions $h_{ij}(x)$ can be interpreted as a set of outputs. This means that the conditions including such a function do not constitute a boundary condition, for the condition may be met a posteriori by defining $h_{ij}(x)$ accordingly. This can be seen from kernel condition \mathcal{K}_1 defined at $\delta\mathcal{T}_1 : (x, 0)$, which results in N conditions for any solution $\mathbf{v}(0, t)$:

$$\begin{aligned} \mathcal{K}_1 : -k_\xi^{ij}(x, 0)\sigma_{jj}(0) + \sum_{m=1}^3 \left(k_{im}(x, 0)(\phi_{mj}(0) + \sigma_{mm}(0)e_{mj}) \right) = \\ \sum_{m=1}^3 \left(h_{im}(x)(e_{mj} - k_{mj}(0, 0)) \right), \end{aligned} \quad (4.34)$$

which couples $k_{ij}(0, 0)$ row-wise and $k_{ij}(x, 0), h_{ij}(x)$ column-wise. Provided $E - K(0, 0)$ is invertible, (4.34) denotes a set of N additional conditions for the column-wise coupled outputs $h_{ij}(x)$. If $H(x)$ is set to zero, the degrees of freedom are lost and kernel condition \mathcal{K}_1 amounts nine boundary conditions to \mathcal{B}_1 . Hence, $H(x)$ can be used to reduce the number of boundary conditions arising from \mathcal{K}_1 .

Kernel condition 3

Focusing on $\delta\mathcal{T}_3 : (x, x)$, the third kernel condition is often the problematic one for control design using p.d.e. backstepping [2]. Kernel condition \mathcal{K}_3 (4.33) imposes a set of Dirichlet-type conditions,

$$\mathcal{K}_3 : \sigma_{ii}(x)k_{ij}(x, x) - k_{ij}(x, x)\sigma_{jj}(x) + \phi_{ij}(x) - \psi_{ij}(x) = 0, \quad (4.35)$$

which restricts the class of allowable target systems by inclusion of $\Psi(x)$. It is clear that this condition is independent of $k_{ii}(x, x)$, i.e., the kernel functions on the diagonal of $K(x, x)$. So, \mathcal{K}_3 results in six conditions for $i \neq j$ (4.36) and three requirements on $\psi_{ii}(x)$ (4.37).

$$k_{ij}(x, x) = \frac{\psi_{ij}(x) - \phi_{ij}(x)}{\sigma_{ii}(x) - \sigma_{jj}(x)} \quad \text{for } i \neq j \quad (4.36)$$

$$\phi_{ii}(x) - \psi_{ii}(x) = 0 \quad \text{for } i = j \quad (4.37)$$

Since $\Psi(x)$ is included also in \mathcal{K}_2 , it introduces a nonlinearity in that kernel condition via $\Psi(x)K(x, x)$ restricting further simplification. Therefore, we choose $\Psi(x) = \Phi(x)$ such that the condition trivially yields the boundary conditions for $k_{ij}(x, x)$ with $i \neq j$:

$$k_{ij}(x, x) = 0 \quad \text{for } i \neq j \quad (4.38)$$

Hence, this condition also implies the requirement that $k_{ij}(0, 0) = 0$ for the off-diagonal kernel functions. Note that in Vaquez and Krstic [78], their target system transforms the reaction matrix only such that \mathcal{K}_3 leads to $k_{ij}(x, x) = 0$ for $i \neq j$ directly.

Kernel condition 2

The second kernel condition \mathcal{K}_2 (4.32) yields N Robin-type conditions, which can be denoted in component-wise form:

$$\begin{aligned} \mathcal{K}_2 : \sigma_{ii}(x)k_x^{ij}(x, x) + k_\xi^{ij}(x, x)\sigma_{jj}(x) + \sum_{m=1}^3 (-k_{im}(x, x)\phi_{mj}(x) + \psi_{im}(x)k_{mj}(x, x)) \\ + \frac{d}{dx}(\sigma_{ii}(x)k_{ij}(x, x)) + \lambda_{ij}(x) - \theta_{ij}(x) = 0. \end{aligned} \quad (4.39)$$

Using (4.37) and (4.38) in \mathcal{K}_2 , the diagonal kernel functions $k_{ii}(x, x)$ can be simplified to yield:

$$\begin{aligned} 0 &= \sigma_{ii}(x)(k_x^{ii}(x, x) + k_\xi^{ii}(x, x)) + \frac{d}{dx}(\sigma_{ii}(x)k_{ii}(x, x)) + \lambda_{ii}(x) - \theta_{ii}(x) \\ &= 2\sigma_{ii}(x)\frac{d}{dx}k_{ii}(x, x) + \sigma_x^{ii}(x)k_{ii}(x, x) + \lambda_{ii}(x) - \theta_{ii}(x) \end{aligned} \quad \text{for } i = j, \quad (4.40)$$

where the Leibnitz differentiation rule defines the total derivative along (x, x) (4.41) through its partial derivatives (4.42). However, note that only the gradient of k_{ij} (4.41) can be computed at $\delta\mathcal{T}_3$, because its components in either direction remain undetermined.

$$\frac{d}{dx}k_{ij}(x, x) = k_x^{ij}(x, x) + k_\xi^{ij}(x, x) \quad (4.41)$$

$$k_x^{ij}(x, x) = \partial_x(k_{ij}(x, \xi))|_{\xi=x}, \quad k_\xi^{ij}(x, x) = \partial_\xi(k_{ij}(x, \xi))|_{\xi=x} \quad (4.42)$$

Kernel condition \mathcal{K}_3 can be integrated for $i = j$ along the boundary $\delta\mathcal{T}_3 : (x, x)$, which specifies Dirichlet-type boundary conditions for $k_{ii}(x, x)$ explicitly:

$$k_{ii}(x, x) = \frac{-1}{\sqrt{\sigma_{ii}(x)}} \int_0^x \frac{\lambda_{ii}(s) - \theta_{ii}(s)}{2\sqrt{\sigma_{ii}(s)}} ds + \frac{\sqrt{\sigma_{ii}(0)}k_{ii}(0, 0)}{\sqrt{\sigma_{ii}(x)}} \quad \text{for } i = j. \quad (4.43)$$

The third kernel condition can be simplified also for $i \neq j$ by substitution of (4.38), which provides six boundary conditions at $\delta\mathcal{T}_3$:

$$(\sigma_{ii}(x) - \sigma_{jj}(x))k_x^{ij}(x, x) + \phi_{ij}(x)(k_{jj}(x, x) - k_{ii}(x, x)) + \lambda_{ij}(x) - \theta_{ij}(x) = 0 \quad \text{for } i \neq j. \quad (4.44)$$

Hence, the summation of k_{im} and k_{mj} simplifies to $k_{ii}(x, x)$ and $k_{jj}(x, x)$, while $k_{ij}(x, x) = 0$ gives the total derivative as $\frac{d}{dx}k_{ij}(x, x) = 0$ that implies $k_x^{ij}(x, x) = -k_\xi^{ij}(x, x)$. However, it is not possible to further reduce the complexity or number of kernel conditions.

Set of boundary conditions

The kernel conditions \mathcal{K}_2 and \mathcal{K}_3 yield a total of 15 boundary conditions. It can be seen that this requires six degrees of freedom in kernel condition \mathcal{K}_1 such that it amounts at most three boundary conditions to \mathcal{B}_1 . This is realized by setting the functions below the diagonal of $H(x)$ to zero, i.e., $h_{ij}(x) = 0$ for

$i > j$. Therefore, the total boundary condition set \mathcal{B}_1 can be defined:

$$\begin{aligned} -k_\xi^{ij}(x, 0)\sigma_{jj}(0) + \sum_{m=1}^3 (k_{im}(x, 0)(\phi_{mj}(0) + \sigma_{mm}(0)e_{mj})) &= 0 \quad \text{for } i > j \\ \mathcal{B}_1 : \quad k_{ii}(x, x) &= \frac{-1}{\sqrt{\sigma_{ii}(x)}} \int_0^x \frac{\lambda_{ii}(s) - \theta_{ii}(s)}{2\sqrt{\sigma_{ii}(s)}} ds + \frac{\sqrt{\sigma_{ii}(0)}k_{ii}(0, 0)}{\sqrt{\sigma_{ii}(x)}} = 0 \quad \text{for } i = j \quad (4.45) \\ k_{ij}(x, x) &= 0 \quad \text{for } i \neq j \\ (\sigma_{ii}(x) - \sigma_{jj}(x))k_x^{ij}(x, x) + \phi_{ij}(x)(k_{jj}(x, x) - k_{ii}(x, x)) + \lambda_{ij}(x) - \theta_{ij}(x) &= 0 \quad \text{for } i \neq j \end{aligned}$$

The choice to set $h_{ij}(x) = 0$ for $i > j$ is by the structure of the s.o.l. boundary condition $E\mathbf{w}(0, t)$. The lower triangular form ensures that $H(x)[E - K(0, 0)]$ also contains zeros below the diagonal:

$$\begin{bmatrix} h_{11}(x)(e_{11} - k_{11}(0, 0)) & h_{12}(x)(e_{22} - k_{22}(0, 0)) & h_{13}(x)(e_{33} - k_{33}(0, 0)) + e_{13}h_{11}(x) + e_{23}h_{12}(x) \\ 0 & h_{22}(x)(e_{22} - k_{22}(0, 0)) & h_{23}(x)(e_{33} - k_{33}(0, 0)) + e_{23}h_{22}(x) \\ 0 & 0 & h_{33}(x)(e_{33} - k_{33}(0, 0)) \end{bmatrix}. \quad (4.46)$$

However, other formats for $H(x)$ can be chosen as well. The restriction hereto is that the functions decoding the off-diagonal elements e_{13} and e_{23} cannot be set to zero.

The remaining kernel conditions in \mathcal{K}_1 (4.34) reduce to additional conditions, which are used to compute $h_{ij}(x)$ for $i \leq j$ after the kernel solution is obtained. Additionally, we have chosen the advective term $\Psi(x) = \Phi(x)$, which fixes the advection matrix of the target system. As a result, the total set \mathcal{B}_1 contains $2N$ boundary conditions with additional conditions and requirements that fulfill the properties stated at the beginning of this section. Analysis of the target system stability is performed in the next section, where we derive conditions that guarantee asymptotic stability of the target p.d.e. system.

4.2.2 Stability analysis of target system

The stability proof of a p.d.e. system is most often based on Lyapunov's direct method [69]. The direct method focuses on finding a Lyapunov functional candidate satisfying the properties denoted in Theorem 1 [29]. This implies that the system tends toward the equilibrium along any trajectory for $t \rightarrow \infty$, except at the equilibrium.

Theorem 1. Lyapunov stability [29, §4.1, p. 114]. *Suppose $\mathbf{w}(x, t)$ is a solution for (3.49) with boundary conditions (4.23)–(4.24). Suppose the equilibrium solution is given by $\bar{\mathbf{w}}(x)$. Let $V : \mathbb{R}^3 \rightarrow \mathbb{R}$ be a continuously differentiable function such that*

$$V(\bar{\mathbf{w}}(x)) = 0, \quad (4.47)$$

$$V(\mathbf{w}(x, t)) > 0 \quad \text{for } \mathbf{w}(x, t) \neq \bar{\mathbf{w}}(x). \quad (4.48)$$

If the rate of change of $V(t)$

$$\dot{V}(t) < 0 \quad \text{for } \mathbf{w}(x, t) \neq \bar{\mathbf{w}}(x) \quad (4.49)$$

then the equilibrium solution $\bar{\mathbf{w}}(x)$ is asymptotically stable in the sense of Lyapunov.

The theory of Lyapunov can be used to establish the stability properties of a given system or to find conditions that guarantee stability. Theorem 1 is used to establish a set of stability conditions for the target system, despite the unknown coefficient matrix $H(x)$. In p.d.e. literature, the Lyapunov functionals often include the L^2 spatial norm (squared) on the interval $[0, L]$ (positive semi-definite):

$$\|\mathbf{w}\|_{L^2}^2 = \int_0^L |\mathbf{w}|^2 dx, \quad (4.50)$$

which is the infinite-dimensional extension to the space of square-integrable vector functions of the finite-dimensional 2-norm, i.e., the Euclidean norm:

$$|\mathbf{w}| = \left(\sum_{i=1}^n |w_i|^2 \right)^{1/2}. \quad (4.51)$$

Candidate Lyapunov functional

A Lyapunov functional can be seen as a measure of the energy in the system, which is non-negative $\forall x, t \in \Omega$. To determine the stability of the target system, we consider the candidate Lyapunov functional $V : \mathbb{R}^3 \rightarrow \mathbb{R}$:

$$V(t) = \frac{1}{2} \int_0^L \mathbf{w}^\top P \mathbf{w} dx, \quad (4.52)$$

$$P = \text{diag } p_{ii} \succ 0 \quad (4.53)$$

It is easily seen that $V(t)$ (4.52) satisfies properties (4.47) and (4.48). Using the degrees of freedom in the target system, i.e., the coefficient functions $\theta_{ij}(x)$, we aim to find the lower limit that theoretically guarantees asymptotic stability. Therefore, the time derivative of $V(t)$ (4.52) is computed, along an arbitrary solution of the p.d.e. system:

$$\begin{aligned} 2\dot{V} &= \int_0^L [\mathbf{w}^\top P \mathbf{w}_t + \mathbf{w}_t^\top P \mathbf{w}] dx \\ &= [\mathbf{w}^\top P \Sigma \mathbf{w}_x]_0^L + \int_0^L [\mathbf{w}^\top P (\Phi \mathbf{w}_x + \Theta \mathbf{w}) - \mathbf{w}_x^\top P \Sigma \mathbf{w}_x] dx + \int_0^L [\mathbf{w}^\top P H \mathbf{w}_x(0, t)] dx \\ &\quad [\mathbf{w}_x^\top \Sigma P \mathbf{w}]_0^L + \int_0^L [(\mathbf{w}_x^\top \Phi^\top + \mathbf{w}^\top \Theta^\top) P \mathbf{w} - \mathbf{w}_x^\top \Sigma P \mathbf{w}_x] dx + \int_0^L [\mathbf{w}_x(0, t) H^\top P \mathbf{w}] dx \end{aligned} \quad (4.54)$$

using $(A_1 \dots A_n) = (A_n^\top \dots A_1^\top)^\top$, $\Sigma = \Sigma^\top$ and $P = P^\top$. Note that partial integration has been used in (4.54) to obtain

$$\int_0^L \mathbf{w}^\top P \partial_x (\Sigma \mathbf{w}_x) dx = [\mathbf{w}^\top P \Sigma \mathbf{w}_x]_0^L - \int_0^L \mathbf{w}_x^\top P \Sigma \mathbf{w}_x dx. \quad (4.55)$$

For clarity, \dot{V} (4.54) is separated into stability contributions from the boundary conditions in \dot{V}_1 (4.56), the infinite-dimensional integral arguments in \dot{V}_2 (4.57) and the integral affecting $H(x)\mathbf{w}_x(0, t)$ in \dot{V}_3 (4.58).

$$\dot{V}_1 = [\mathbf{w}^\top P \Sigma \mathbf{w}_x + \mathbf{w}_x^\top \Sigma P \mathbf{w}]_0^L \quad (4.56)$$

$$\dot{V}_2 = \int_0^L [\mathbf{w}^\top (P\Theta + \Theta^\top P) \mathbf{w} + \mathbf{w}^\top P \Phi \mathbf{w}_x + \mathbf{w}_x^\top \Phi^\top P \mathbf{w} - \mathbf{w}_x^\top (P\Sigma + \Sigma P) \mathbf{w}_x] dx \quad (4.57)$$

$$\dot{V}_3 = \int_0^L [\mathbf{w}^\top P H \mathbf{w}_x(0, t) + \mathbf{w}_x^\top(0, t) H^\top P \mathbf{w}] dx \quad (4.58)$$

Target boundary conditions \dot{V}_1

The boundary conditions for the target system must be chosen adequately such that $\dot{V}_1 < 0$. We choose the s.o.l. boundary condition for the target system equivalent to $\mathbf{v}_x(0, t) = E\mathbf{v}(0, t)$, while \mathbf{w}_x is required to vanish at the plasma core:

$$\mathbf{w}_x(0, t) := [E - K(0, 0)] \mathbf{w}(0, t), \quad \mathbf{w}_x(L, t) := 0. \quad (4.59)$$

Substituting (4.59) into (4.56) reduces the contribution from the boundary conditions to

$$\dot{V}_1 = -\mathbf{w}(0, t)^\top \left[P\Sigma(0) [E - K(0, 0)] + [E - K(0, 0)]^\top \Sigma(0)P \right] \mathbf{w}(0, t), \quad (4.60)$$

which leads the symmetric matrix inequality,

$$P\Sigma(0) [E - K(0, 0)] + [E - K(0, 0)]^\top \Sigma(0)P \succ 0, \quad (4.61)$$

with $K(0, 0) = \text{diag } k_{ii}(0, 0)$ due to \mathcal{B}_1 (4.45). It should be noted that the stability of E depends strongly on the equilibrium solution $\bar{v}(x, t)$ about which the linearization is obtained. This is because the eigendecomposition adds extra couplings into the boundary condition matrix E , which are significant compared to the scrape-off layer e-folding scales (i.e., $\frac{1}{\lambda_{n,T,Z}}$ on the diagonal):

$$E = \begin{bmatrix} \frac{1}{\lambda_n} & 0 & \frac{q_{13}(0)}{\lambda_n} - \frac{q_{13}(0)}{\lambda_Z} - q_x^{13}(0) \\ 0 & \frac{1}{\lambda_T} & \frac{q_{23}(0)}{\lambda_T} - \frac{q_{23}(0)}{\lambda_Z} - q_x^{23}(0) \\ 0 & 0 & \frac{1}{\lambda_Z} \end{bmatrix} \approx \begin{bmatrix} \frac{4}{5} & 0 & 2.29 \\ 0 & \frac{2}{3} & 0.61 \\ 0 & 0 & \frac{4}{5} \end{bmatrix}. \quad (4.62)$$

For the nominal plant equilibrium, it is not obvious that the matrix inequality suffices the positive definiteness condition. Therefore, example 1 is presented to show the effect of the kernel condition $K(0, 0)$ on stability.

Example 1. Let P and $K(0, 0)$ be chosen, within restrictions implied by \mathcal{B}_1 (4.45), as

$$P = I, \quad K(0, 0) = -2I \quad (4.63)$$

where I is the identity matrix and $k_{ii}(0, 0) = 0$ is fulfilled. Then \dot{V}_1 amounts to the stability of the target system, since the linear matrix inequality (4.61) becomes positive definite:

$$\begin{bmatrix} 5.80 & 0 & 2.38 \\ 0 & 11.05 & 1.25 \\ 2.38 & 1.25 & 1.21 \end{bmatrix} \succ 0. \quad (4.64)$$

By restating the condition as $E \succ K(0, 0)$, it can be seen that the eigenvalues of $E - K(0, 0)$ can be shifted by choosing $K(0, 0)$ sufficiently negative such that $\dot{V}_1 < 0$. This also shows that the eigenvalues are dominantly determined by $K(0, 0)$ for $-k_{ii}(0, 0) \gg \max_{i,j} e_{ij}$, which makes the system more stable.

Infinite-dimensional integral arguments \dot{V}_2

Secondly, the integral arguments of \dot{V}_2 are put in the augmented matrix S_1 . This yields the following condition for \dot{V}_2 , which should hold for any target system solution:

$$\dot{V}_2 = \int_0^L \begin{bmatrix} \mathbf{w} \\ \mathbf{w}_x \end{bmatrix}^\top \begin{bmatrix} P\Theta + \Theta^\top P & P\Phi \\ \Phi^\top P & -2P\Sigma \end{bmatrix}_{S_1} \begin{bmatrix} \mathbf{w} \\ \mathbf{w}_x \end{bmatrix} dx, \quad (4.65)$$

where S_1 is a symmetric matrix. The damping term Θ constitutes a set of nine degrees of freedom, which must be chosen sufficiently negative such that $V < 0$. However, the off-diagonal coefficients do not necessarily contribute to stability, because these provide extra couplings between the states. Such coupling divides the energy inserted into the system by the damping term. Hence, we let Θ assume a diagonal form, which imposes the requirement:

$$\theta_{ij}(x) = 0, \quad \text{for } i \neq j. \quad (4.66)$$

Since the matrix S_1 is symmetric under requirement (4.66), there are various theorems that can be used to formulate conditions that guarantee $S_1 \prec 0$. Before the stability condition for \dot{V}_2 (4.65) is derived, the third contribution \dot{V}_3 is assessed to reveal the implications of the uncommon additional advective term $H(x)$.

Additional boundary advection \dot{V}_3

Thirdly, we consider the contribution of the integral with argument $H(x)\mathbf{w}_x(0,t)$. This term requires an estimation, whereas the other integrals contain the infinite-dimensional state, spatial derivative or a combination thereof. To find upper bounds, the Cauchy-Schwarz inequality (4.67) and Young's inequality (4.68) are frequently used for Lyapunov functionals. It should be noted that Young's inequality gives a tighter bound than the inequality of Cauchy and Schwarz.

$$\|\mathbf{v}^\top \mathbf{w}\|_{L^2} \leq \|\mathbf{v}\|_{L^2} \|\mathbf{w}\|_{L^2} \quad \text{Cauchy-Schwarz inequality} \quad (4.67)$$

$$\|\mathbf{v}\|_{L^2} \|\mathbf{w}\|_{L^2} \leq \frac{\alpha_m}{2} \|\mathbf{v}\|_{L^2}^2 + \frac{1}{2\alpha_m} \|\mathbf{w}\|_{L^2}^2, \quad \alpha_m > 0 \quad \text{Young's inequality} \quad (4.68)$$

For brevity, we define an upper bound for $H(x)$ based on the coefficient bound h_{\max} and its structure, which is due to the definition of the (kernel) boundary conditions \mathcal{B}_1 (4.45):

$$H(x) \leq h_{\max} H_* := \max_{x,i,j} |h_{ij}(x)| \begin{bmatrix} 1 & 1 & 1 \\ 0 & 1 & 1 \\ 0 & 0 & 1 \end{bmatrix}. \quad (4.69)$$

Using the Cauchy-Schwarz inequality (4.67) and Young's inequality (4.68), an upper bound is found for \dot{V}_3 in terms of the spatial norms and coefficient bound h_{\max} :

$$\begin{aligned} \dot{V}_3 &= 2 \int_0^L [\mathbf{w}^\top P H(x) \mathbf{w}_x(0,t)] dx \leq 2 \left\| \mathbf{w}^\top \sqrt{P} \right\|_{L^2} \left\| \sqrt{P} H(x) E \mathbf{w}(0,t) \right\|_{L^2} \\ &\leq \alpha_1 \left\| \mathbf{w}^\top \sqrt{P} \right\|_{L^2}^2 + \frac{h_{\max}^2}{\alpha_1} \left\| \sqrt{P} H_* E \mathbf{w}(0,t) \right\|_{L^2}^2, \end{aligned} \quad (4.70)$$

where the introduction of $\mathbf{w}_x(0,t) = E\mathbf{w}(0,t)$ (4.59) is motivated by the estimation procedure, which yields a bound in terms of its function and derivative, i.e., the H^1 norm. At the s.o.l. $\mathbf{w}(0,t)$ can be estimated using a test function $f(x) \in \mathbb{R}$,

$$f(x) := \frac{x-L}{L} = \begin{cases} -1, & \text{for } x=0 \\ 0, & \text{for } x=L \end{cases}, \quad (4.71)$$

which is chosen such that $\mathbf{w}(L,t)$ drops out:

$$f(L)\sqrt{P}H_*E\mathbf{w}(L,t) - f(0)\sqrt{P}H_*E\mathbf{w}(0,t) = \int_0^L [f(x)\sqrt{P}H_*E\mathbf{w}(x,t)]_x dx. \quad (4.72)$$

Introducing the estimation (4.72) into (4.70), the stability contribution of \dot{V}_3 can be bounded by:

$$\begin{aligned} \dot{V}_3 &\leq \alpha_1 \left\| \mathbf{w}^\top \sqrt{P} \right\|_{L^2}^2 + \frac{h_{\max}^2}{\alpha_1} \left\| \sqrt{P} H_* E \mathbf{w}(0,t) \right\|_{L^2}^2 \\ &\leq \alpha_1 \int_0^L [\mathbf{w}^\top P \mathbf{w}] dx + \frac{h_{\max}^2}{\alpha_1 L^2} \int_0^L \left| [(x-L)\sqrt{P}H_*E\mathbf{w}(x,t)]_x \right|^2 dx \\ &\leq \alpha_1 \int_0^L [\mathbf{w}^\top P \mathbf{w}] dx + \frac{2h_{\max}^2}{\alpha_1 L^2} \int_0^L [\mathbf{w}^\top (E^\top H_*^\top P H_* E) \mathbf{w} + L^2 \mathbf{w}_x^\top (E^\top H_*^\top P H_* E) \mathbf{w}_x] dx, \end{aligned} \quad (4.73)$$

using $|x-L|^2 \leq L^2$ and the norm property $|\mathbf{w} + \mathbf{w}_x|^2 \leq 2|\mathbf{w}|^2 + 2|\mathbf{w}_x|^2$. The contribution \dot{V}_3 is rephrased into a matrix integral equation, with the matrix denoted by S_2 , to yield the inequality:

$$\dot{V}_3 \leq \int_0^L \begin{bmatrix} \mathbf{w} \\ \mathbf{w}_x \end{bmatrix}^\top \begin{bmatrix} \alpha_1 P + \alpha_2 P_* & 0 \\ 0 & \alpha_3 P_* \end{bmatrix} \begin{bmatrix} \mathbf{w} \\ \mathbf{w}_x \end{bmatrix} dx, \quad (4.74)$$

where

$$\begin{aligned}\alpha_2 &= \frac{2h_{\max}^2}{\alpha_1 L^2}, \quad \alpha_3 = \frac{2h_{\max}^2}{\alpha_1}, \\ P_* &= E^\top H_*^\top P H_* E.\end{aligned}\tag{4.75}$$

This integral equation contains a single d.o.f. in choosing α_1 . This concludes the derivation of the stability conditions, which are used to find the solution and boundary feedback controller in § 4.3.

4.3 Boundary feedback controller

The approximation strategy to finding a kernel solution is the subject of § 4.3.1. This provides a method to obtain the kernel solution in § 4.3.2 sufficing the stability conditions (4.79)–(4.81). The boundary feedback control law is derived in § 4.3.3.

4.3.1 Procedure for numerical solution

The boundary advection contribution (4.74) complicates the stability analysis due to the unknown bound h_{\max} and uncontrollable term $\alpha_3 P_*$. Therefore, it is not possible to analyze stability directly without deriving an explicit bound for h_{\max} . Although an explicit bound can be found [2], we follow a numerical approach to cope with the a priori unknown term. This approach allows to find a solution for the kernel system, which can be verified in light of stability a posteriori. This is motivated by the negligible analytic effort, despite that we need to make an assumption on the boundedness of $H(x)$.

First, focus on the uncontrollable term by noting that Θ acts on the state \mathbf{w} only. This means that we need to shift the advection contribution towards the state \mathbf{w} by setting, e.g., $\alpha_1 = 2\beta h_{\max}^2$ such that:

$$S_2 = \begin{bmatrix} 2\beta h_{\max}^2 P + \frac{1}{\beta L^2} P_* & 0 \\ 0 & \frac{1}{\beta} P_* \end{bmatrix}, \quad (4.76)$$

with $\beta > 0$ a free parameter. Now, the structure of both \dot{V}_2 and \dot{V}_3 allows addition of both matrices to yield S :

$$\dot{V}_2 + \dot{V}_3 \leq \int_0^L \begin{bmatrix} \mathbf{w} \\ \mathbf{w}_x \end{bmatrix}^\top \begin{bmatrix} 2P\Theta + 2\beta h_{\max}^2 P + \frac{1}{\beta L^2} P_* & P\Phi \\ \Phi^\top P & -2P\Sigma + \frac{1}{\beta} P_* \end{bmatrix} \begin{bmatrix} \mathbf{w} \\ \mathbf{w}_x \end{bmatrix} dx, \quad (4.77)$$

where $P_* = P_*^\top$ by definition (4.75) and $\Theta = \Theta^\top$ due to requirement (4.66). The integral of (4.77) implies that S must be negative definite across the whole domain. Hereto, the positive definiteness of $-S$ is analyzed using the Schur complement stated in Theorem 2.

Theorem 2. Let S be given by the symmetric matrix (4.77). Then $-S$ is positive definite if and only if $\left[2P\Sigma - \frac{1}{\beta} P_*\right] \succ 0$ and the complement of $\left[2P\Sigma - \frac{1}{\beta} P_*\right]$ in $-S$, i.e.,

$$-S / \left[2P\Sigma - \frac{1}{\beta} P_*\right] = - \left[2P\Theta + 2\beta h_{\max}^2 P + \frac{1}{\beta L^2} P_*\right] - P\Phi \left[2P\Sigma - \frac{1}{\beta} P_*\right]^{-1} \Phi^\top P \succ 0, \quad (4.78)$$

for all $x \in \Omega$.

Using the Schur complement of $-S$, the stability conditions can phrased as a set of (linear) matrix inequalities, called \mathcal{C} :

$$\mathcal{C}_1 : \quad 0 \prec P\Sigma(0) [E - K(0, 0)] + [E - K(0, 0)]^\top \Sigma(0) P, \quad (4.79)$$

$$\mathcal{C}_2 : \quad \frac{1}{\beta} P_* \prec 2P\Sigma, \quad (4.80)$$

$$\mathcal{C}_3 : \quad 2P\Theta \prec -2\beta h_{\max}^2 P - \frac{1}{\beta L^2} P_* - P\Phi \left[2P\Sigma - \frac{1}{\beta} P_*\right]^{-1} \Phi^\top P \quad (4.81)$$

The difficulty to proceed the stability analysis relies in the freedom of the target system. The issue is boundedness of $H(x)$, which is determined by the additional conditions from \mathcal{K}_1 (4.34) at $\delta\mathcal{T}_1$. Kernel

solution $K(x, 0)$ at $\delta\mathcal{T}_1$ is part of the kernel transformation, which maps a full-rank matrix $\Lambda(x)$ into a diagonal damping matrix $\Theta(x)$. Therefore, the coefficient functions $\theta_{ii}(x)$ influence the solution of $h_{ij}(x)$ ¹, the maximum bound (h_{\max}) of which enters condition (4.81) quadratically.

Yet, there are additional degrees of freedom $k_{ii}(0, 0)$ that are not restricted to either the boundary conditions for the kernel system nor the stability analysis. $K(0, 0)$ is included in kernel condition \mathcal{K}_1 (4.34) at the right-hand side: $H(x)[E - K(0, 0)]$. Although the stability from the boundary conditions (4.61) imposes a constraint on $K(0, 0)$, it is satisfied if $k_{ii}(0, 0)$ is sufficiently negative. Therefore, we denote the following assumption:

Assumption 1. *For a given $\Theta(x)$, it is possible to choose $k_{ii}(0, 0)$ sufficiently large and negative such that the outputs $h_{ij}(x)$ are suppressed.*

This allows to consider the following strategy:

1. If $h_{ij}(x) \rightarrow 0$, the analysis provides a condition on the elements of $\Theta(x)$, i.e., $\theta_{ii}(x) < \theta_{\min}(x) < 0$, where $\theta_{\min}(x)$ follows from (4.81).
2. The kernel solution $K(x, \xi)$ can be solved numerically to obtain the kernel functions $K(x, 0)$ at the boundary $\delta\mathcal{T}_1 : (x, 0)$, which reveal the boundary advection matrix $H(x)$.
3. Condition (4.81) can be checked whether $\dot{V} < 0$.
4. If $h_{\max} \gg 0$, $K(0, 0)$ can be redefined based on the obtained solution for $H(x)$, which provides the input to start again at (2).

In the following section, the kernel p.d.e. system is solved using the aforementioned procedure and the stability conditions (4.79)–(4.81). The second-order kernel problem § 4.1.4 is transformed into an equivalent first-order system in Appendix E to include both Dirichlet- and Robin-type boundary conditions at a single domain boundary. The kernel equations are solved using the MATLAB PDE toolbox, of which the numerical implementation is outlined in Appendix F.

4.3.2 Solution of the kernel system

A solution of the kernel p.d.e. system is obtained via a series of approximations, of which the first approximation assumes $h_{ij}(x) = h_{\max} = 0$ to derive the stability condition explicitly. Note that we do not change the boundary conditions for the kernel system, since we want to obtain the solution $h_{ij}(x)$ corresponding to the choice of $\Theta(x)$. This allows definition of a minimum function $\theta_{\min}(x)$ for the coefficients $\theta_{ii}(x)$, which is shown logarithmically in Figure 4.3 for $0 \leq x \leq L$.

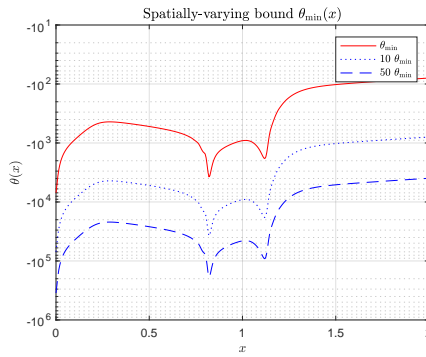


Figure 4.3: Spatially-varying minimum bound $\theta_{\min}(x)$ and integer multiples thereof are shown on a (negative) logarithmic scale. Note that the spatial distance near the transport barrier and separatrix is increased by raising the damping.

¹The influence of $\Theta(x)$ on $H(x)$ is not obvious, but this amounts to $h_{\max} \sim \max_{x,i} \theta_{ii}$ as verified numerically.

As can be seen, the dynamical properties vary strongly around the transport barrier ($x \approx 1$). A similar behavior can be seen from the diffusion coefficients, which are included inversely in the stability condition (4.81). Also, it is indicated in Figure 4.3 the coefficients increase significantly near the separatrix. The s.o.l. solution is important to the bifurcation dynamics, because it directly specifies the electric field shear via the Robin-type boundary condition. When lowering the heat flux, there is a decline in thermodynamic currents and electric field. This increases the diffusivity by lesser flow shear, which requires smaller gradients. Hence, the coefficients are set such that $\theta_{ii}(x) = 8\theta_{\min}(x)$ ($1 \leq i \leq 3$) to account for model (coefficient) uncertainty near the separatrix and transport barrier².

Now, we consider two extreme cases that are obtained from the successive approximations. During the approximation series, we have increased the damping term or further decreased the boundary condition $k_{ii}(0, 0) < 0$. The values set for each case are noted in Table 4.1 and we set the damping bound to a constant bound for simplicity.

For the first case, the stability conditions (4.79) and (4.80) are satisfied by choosing the parameters adequately. This leads to an update for the condition on Θ involving h_{\max} , which is shown spatially in Figure 4.4. It can be seen that the third condition is not met, which is due to the advection term and results in instability of the target system. The maximum value of h_{\max} enters the condition quadratically, while the parameter β has a minimum due to the second condition. Hence, it is not possible to design a stable boundary feedback controller for this case.

Secondly, we consider another extreme case which is defined by the insight gained from previous approximations. The values for the second case are shown also in Table 4.1, which already reveals that h_{\max} has significantly declined compared to the first case. In Figure 4.5, we depict again the stability condition \mathcal{C}_2 to show the influence of an increased damping and decrease in boundary condition $k_{ii}(0, 0)$ at the origin of the kernel domain.

Table 4.1: Two extreme cases considered during the successive approximations.

Case	$k_{ii}(0, 0)$	$\min \theta_{ii} : \theta_{\min}$	h_{\max}
1	-10^1	10	$\sim 10^4$
2	-10^5	50	$\sim 10^1$

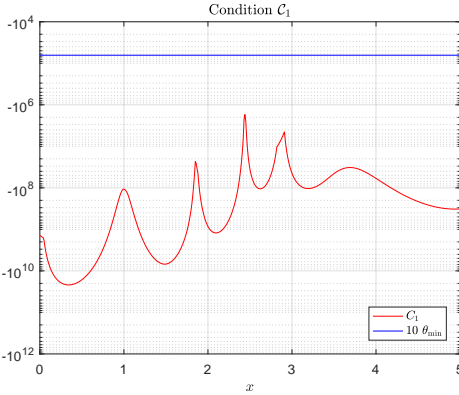


Figure 4.4: The updated condition requires θ_{\min} larger by $\sim 10^5$.

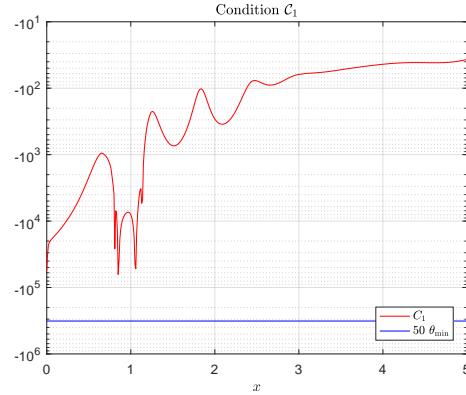


Figure 4.5: Stability condition \mathcal{C}_1 can be sufficed for sufficiently large $\theta_{ii}(x)$ and large $k_{ii}(0, 0) < 0$.

²It should be noted that the location of the separatrix and transport barrier are also uncertain during experiment.

The kernel functions $k_{ij}(x, \xi)$ are shown in Figure 4.6 at the domain boundary $\delta\mathcal{T}_3 : (x, x)$. It can be seen that the off-diagonal solutions obey the boundary condition $k_{ij}(x, x) = 0$ ($i \neq j$). At the origin $(x, \xi) = (0, 0)$, the kernel functions $k_{ij}(x, x)$ converge to zero for $i \neq j$ and $k_{ii}(x, x)$ tend to $k_{ii}(0, 0)$ specified by the boundary condition. The same holds for the function $k_{ij}(x, x)$ at $\delta\mathcal{T}_1 : (x, 0)$ as can be seen from Figure 4.7. Furthermore, the diagonal functions at the origin are set $k_{ii}(0, 0) = -10^5$ and $P = I$, where example 1 shows $K(0, 0) = -2I$ already leads to stable boundary conditions for the target system via condition (4.79).

In Figure 4.8, the boundary advection functions $h_{ij}(x)$ are depicted that verify stability of the target system. This can be seen from the stability conditions (4.80)–(4.81). Condition \mathcal{C}_1 is easily verified by setting $\beta > \beta_{\min}$:

$$\beta_{\min} = \frac{\|H_*\|_2 \|E\|_2}{\sigma_{\min}}, \quad (4.82)$$

given $\sigma_{\min} = \min_{x,i} \sigma_{ii}(x)$ and $P = I$. The third condition \mathcal{C}_1 for stability can be computed as well by updating the bound θ_{\min} (found for $H(x) = 0$) to $\hat{\theta}_{\min}$:

$$\hat{\theta}_{\min}(x) < -\beta h_{\max}^2 - \frac{\|H_*\|_2 \|E\|_2}{\beta L^2} - \|\Phi(x)\|_2 \left\| \left[\Sigma(x) - \frac{1}{2\beta} P_* \right]^{-1} \right\|_2 \|\Phi^\top(x)\|_2, \quad (4.83)$$

which has been depicted in Figure 4.5.

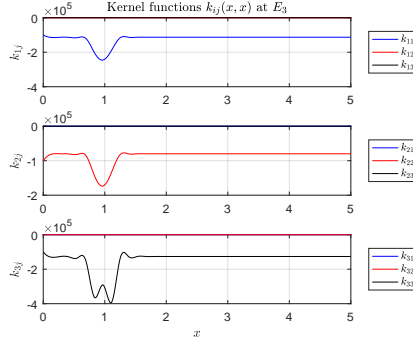


Figure 4.6: Kernel functions $K(x, x)$ at $\delta\mathcal{T}_3$.

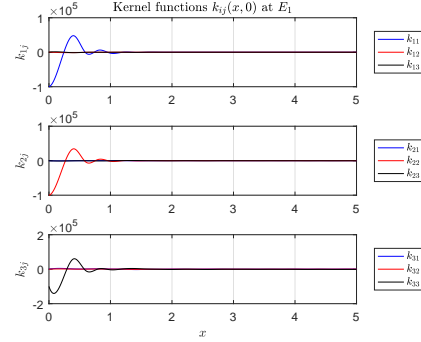


Figure 4.7: Kernel functions $K(x, 0)$ at $\delta\mathcal{T}_1$.

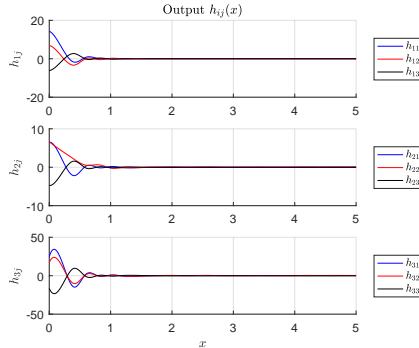


Figure 4.8: Output functions $h_{ij}(x)$ for $\theta_{ii}(x) = 500\theta_{\min}(x)$.

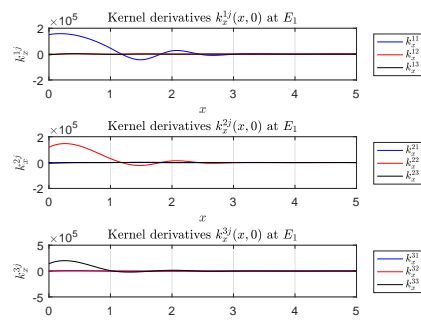


Figure 4.9: Kernel derivatives $K_\xi(x, 0)$ at $\delta\mathcal{T}_1$.

4.3.3 Feedback control law for the plasma model

The kernel solution at the right-hand boundary $\delta\mathcal{T}_2 : (L, \xi)$ determines the boundary feedback controller. The kernel functions $k_{ij}(L, \xi)$ at boundary $\delta\mathcal{T}_2$ are shown in Figure 4.10 and the spatial derivatives $k_x^{ij}(L, \xi)$ thereof can be seen in Figure 4.11. The solution assumes small values outside the region where the transport barrier is active. Towards the s.o.l. boundary, however, the amplitude of the kernel solutions tends to increase again. This can be expected from the stability analysis, which shows that the stabilizing contribution $\Theta(x)$ needs to increase also towards the plasma edge and is mostly active around the transport barrier.

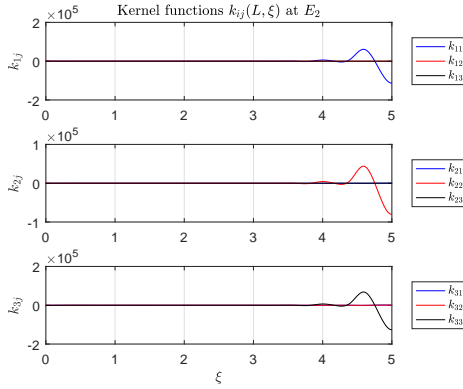


Figure 4.10: Kernel functions $K(L, \xi)$ at $\delta\mathcal{T}_2$.

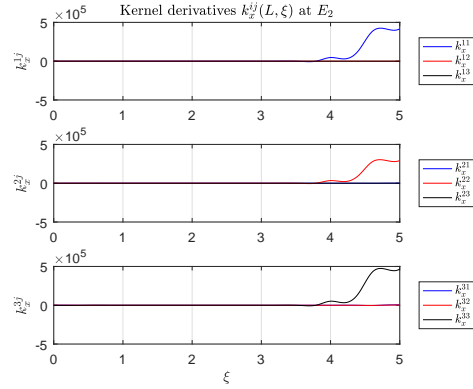


Figure 4.11: Kernel derivatives $K_x(L, \xi)$ at $\delta\mathcal{T}_2$.

The boundary feedback controller can be obtained from the kernel solution using the the boundary condition for the target system. The control input vector can be revealed from the partial derivative of the backstepping transformation (4.24) evaluated at $x = L$, where we use the target boundary condition at the plasma core $\mathbf{w}_x(L, t) = 0$ (4.59):

$$\mathbf{v}_x(L, t) = K(L, L)\mathbf{v}(L, t) + \int_0^L K_x(L, \xi)\mathbf{v}(\xi, t) d\xi. \quad (4.84)$$

Using the state transformations (3.34) and (3.35), it can be seen that the eigendecomposition vanishes for $x \rightarrow L$ and the state of the linear and reference system become identical:

$$\tilde{\mathbf{v}}(L, t) = \mathbf{v}(L, t) \quad (4.85)$$

$$\tilde{\mathbf{v}}_x(L, t) = \mathbf{v}_x(L, t), \quad (4.86)$$

due to the vanishing off-diagonal diffusion coefficients $\lim_{x \rightarrow L} \bar{\sigma}_{ij}(x) = 0$ ($i \neq j$). This is because the coupling of electric field shear on the diffusivities vanishes physically. The boundary feedback for the linear p.d.e. system can thus be formulated as follows:

$$\tilde{\mathbf{v}}_x(L, t) = K(L, L)\tilde{\mathbf{v}}(L, t) + \int_0^L \tilde{K}_x(L, \xi)\tilde{\mathbf{v}}(\xi, t) d\xi, \quad (4.87)$$

where $\tilde{K}_x(L, \xi) := K_x(L, \xi)Q^{-1}(\xi)$ and $K(L, L)$ assumes a diagonal form,

$$K(L, L) = -10^5 \text{ diag}([1.1303 \ 0.7993 \ 1.2632]). \quad (4.88)$$

Using the perturbed equilibrium $\hat{\mathbf{v}}(x, t) = \bar{\mathbf{v}}(x, t) + \tilde{\mathbf{v}}(x, t)$, the boundary feedback can be formulated into a boundary condition for the nonlinear p.d.e. system,

$$\hat{\mathbf{v}}_x(x, t) = \bar{\mathbf{v}}_x(x, t) + \tilde{\mathbf{v}}_x(x, t). \quad (4.89)$$

4.4 Discussion

There are options to resolve the overdetermination of the kernel problem. The options have been investigated and processed through the derivation. The kernel condition \mathcal{K}_3 is often the problematic condition, for spatially-varying or -constant systems [2]:

- It can be seen that condition \mathcal{K}_3 is trivial when K and Σ commute, i.e., $K\Sigma = \Sigma K$ [2]. It is noted that this option has been explored also during this research. However, the commutation property imposes that the diffusion coefficients must be equal for each diagonal element. Due to the different state variables considered, it can be stated that this is usually not possible for a physics-based model/system.
- Boundary condition set \mathcal{B}_1 requires $H(x)$ to assume an upper diagonal form (functions below diagonal are zero), which is in contrast to [78]. There, the authors use a lower triangular matrix with functions on the diagonal also set to zero. For this form, it can be shown that its contribution is stable regardless of $h_{ij}(x)$. However, the non-diagonal format complicates the stability proof and leads to the boundedness assumption on $H(x)$. A thorough mathematical analysis may provide an analytical bound, but this is not pursued due to time restrictions.

The stability analysis can be concluded by noting that we find similar stability conditions as do the authors of [78]. Despite the similar conditions, there are several important differences that should be noted.

- The stability analysis of [78] is based on extreme limit bounds and the target system includes spatially-constant damping coefficients.
- The stability analysis of [78] is more involved due to a second Lyapunov functional $\mathbf{w}_x^\top P \mathbf{w}_x$. This is necessary due to the estimation of $\mathbf{w}_x(0, t)$, which is bounded by the first and second spatial derivative. We are able to use the Robin-type b.c. at the s.o.l. $\mathbf{w}_x(0, t) = E\mathbf{w}(0, t)$ such that only $\mathbf{w}(0, t)$ needs to be estimated.
- The target system of [78] includes an exponentially decaying contribution in the Dirichlet control input $\mathbf{w}(L, t) \propto \exp(-\alpha t)$. This carries over to the reference system such that its origin is exponentially stable. However, we impose an homogeneous boundary condition $\mathbf{w}_x(L, t) = 0$ and do not further exploit the possibility due to time restrictions.

Due to the different approach, it is interesting to compare the spatially-constant bound θ_* from [78] to the spatially-varying bound $\theta_{\min}(x)$. Using their result and our notation to bound $\Sigma, \forall x$, the minimum value θ_* (spatially-constant) is obtained as,

$$\begin{aligned}\theta_* &= \frac{1}{2} \max \left(2p + 1, 2p + \frac{3}{\sigma_{\min}} (\sigma_{x,\max}^2 + p^2) - \frac{7\sigma_{\min}}{4} \right) \\ &\approx \frac{3}{2\sigma_{\min}} (\sigma_{x,\max}^2 + p^2) \approx 1.11 \cdot 10^5,\end{aligned}$$

where the coefficients bounds used in [78] take the numerical values:

$$\max_x \|\Phi(x)\|_2 \leq p \approx 153.42, \quad \sigma_{\min} = \min_{x,i} \sigma_{ii}(x) \approx 0.21, \quad \sigma_{x,\max} = \max_{x,i} \sigma_x^{ii}(x) \approx 59.08. \quad (4.90)$$

Note that the damping term in [78] is defined as $-C\mathbf{w}(x, t)$ instead of $\Theta(x)\mathbf{w}(x, t)$. Comparing the conservative bound θ_* to $\theta_{\min}(x)$ (4.83), it can be seen that the spatially-varying bound is about two orders of magnitude larger: $\max_x |\theta_{\min}(x)| \approx 1.33 \cdot 10^7$.

Chapter 5

Conclusion and discussion

After the research questions are answered in § 5.1, we review and discuss the approach, tools and results that come forth throughout this thesis in § 5.2, which is accompanied by suggestions for further research and control development.

5.1 Conclusion

Sustainment of the H-mode requires a minimum heat flux across the separatrix, which is limited to capabilities of the tokamak divertor and m.h.d. instabilities. Meanwhile, the plasma edge in the H-mode is characterized by large variations of the plasma state in a narrow layer. This study addressed the problem of plasma edge operation near the H-L transition using (model-based) control engineering.

How does the radial electric field equation relate to the L-H transition physics?

The L-H transition model [99] describes the dynamical behavior of the plasma edge, which constitutes an insulating boundary layer in H-mode. Suppression of turbulent transport provides the insulation due to a sheared $\mathbf{E} \times \mathbf{B}$ flow. The plasma model contains a self-consistent description of the (radial) electric field that generates the shear flow during H-mode operation. Due to the nonlinear couplings, the electric field equation gives rise to the confinement bifurcation.

The physical origin of the electric field equation allows to investigate uncertainty of the H-L bifurcation. Analysis of well-known H-mode theory reveals various nonambipolar particle fluxes that contribute to the bifurcation behavior, which are used to derive a physics-based p.d.e. for the electric field. As a result, the physics-based and L-H model equation for the electric field can be compared to assess parametric uncertainties.

The cumulative effect of nonambipolar radial currents yields a nonlinear partial differential equation for the electric field. The physics-based and model equation equivalently contain state-dependent terms due to the polarization current, viscous shear stress, thermodynamic forces and radial currents that are functions of the electric field. This physics-based equation is scaled by $\frac{T}{n}$, because we aim at a comparison to the model equation. Hereto, the linear dependence on plasma density (n) is eliminated from the nonambipolar processes [99].

The polarization (time scale), viscosity and thermodynamic coefficients are comparable within one order of magnitude. However, the polynomial coefficients of our approximation (i.e., function fit $g(Z)$) become of the order 10^{-13} due to the scaling by $\frac{T}{n}$. By contrast, polynomial coefficients $|a, b, c| \sim 10^{-1} - 10^1$ are usually stated for $G(Z)$ by other authors [15, 101, 99, 85]. Hence, there is a discrepancy between the coefficients that follow from our derivation using nonambipolar particle fluxes described in H-mode theory and those that are used for the L-H transition model by other authors. Despite the discrepancy in magnitude, it is shown that the polynomial function qualitatively approximates the nonlinear part of the radial currents.

The physics-based electric field p.d.e. is not used to assess model uncertainty due to the discrepancy to the (L-H transition) model equation. However, insight on the H-mode dynamics substantiates the idea that model uncertainty is a key challenge for plasma control near the H-L bifurcation/transition. Hence, the control objective is focused on plasma control subjected to parametric uncertainty using the L-H transition model.

How close to the H-L bifurcation can the plasma model be stabilized?

The control question has been investigated within the framework of boundary feedback control applied to the (L-H transition) plasma model. The plasma model describes the thin boundary layer at the confined plasma edge, where the heat and particle flux actuate the density and temperature edge profiles directly. The induced thermodynamic currents influence the electric field, the coupling of which to plasma temperature and density presents the main difficulty for control.

Backstepping p.d.e. control has been chosen as the control design procedure. This is motivated by the idea that it provides a systematic method to deal with a p.d.e. system and benefits from the infinite-dimensional structure of the model. This should avoid the need to approximate the model a priori for design and assess the impact of model structure, choices and parameters directly. Yet, the results have shown that the backstepping method for linear p.d.e. systems is not sufficiently developed to constitute a systematical approach for control design. Therefore, we have not been able to fully develop the boundary feedback controller and assess the research objective on a model-basis. The reasons for inadequacy of the backstepping method are mentioned with a focus on the main issues.

The backstepping design procedure restricts the form of the plasma model that can be used for boundary control design.

- The important dynamic of the H-mode is shear flow suppression of turbulence, which implies diffusive couplings between plasma states. The backstepping design is tailored to uncoupled diffusive processes. This compatibility issue is avoided by decoupling the diffusive processes, but leads to irregular advective and reactive coefficients that introduce significant errors in the numerical kernel solution.
- An inhomogeneous boundary condition at the scrape-off layer (s.o.l.) results in an infeasible kernel problem, whereas an homogeneous boundary condition apparently does not [78]. The plasma model cannot be simplified to include an homogeneous s.o.l. boundary condition, because this is physically unrealistic.

The stability analysis reveals that a spatially-constant damping is not required.

- The damping term in the target system is allowed to vary spatially, which results in two benefits. Firstly, it localizes the required damping to the transport barrier and separatrix. Secondly, it allows to suppress the irregular reactive term by setting $\Theta = \Lambda - \text{diag}(C)$ to reduce irregularity in the kernel transformation. However, exact elimination of the reactive term is not reasonable due to the model uncertainty.

The backstepping transformation for linear spatially-varying diffusion-advection-reaction systems has been formulated by Vazquez and Krstic [78]. Here, we denote our findings that follow after the formulation of the kernel problem.

- A feasible backstepping transformation requires the addition of a boundary advection term, which provides nine degrees of freedom. Vazquez and Krstic [78] prove that a maximum of three d.o.f. provides analytical closure of the stability analysis. The kernel characteristic analysis shows that we need six degrees of freedom. Therefore, our stability analysis cannot be solved without analyzing the kernel problem explicitly and requires a numerical approach.
- Due to the boundary advection, the kernel problem becomes feasible at the expense of analytical closure of the stability analysis. We attempt to provide numerical closure by means of a series of successive approximations, which indeed allows to compute the kernel solution. Yet, the required

minimum damping and boundary condition $k_{ii}(0,0) < 0$ to suppress the outputs for stability greatly restricts the target systems.

A thorough assessment of the research objective could not be performed. The backstepping design applied to the L-H transition model did not provide a true systematic approach due to various restrictions. Therefore, a concluding answer to the research objective cannot be given on the basis of the backstepping design.

5.2 Discussion

The result of the physics research question provides a promising route to model the electric field at the plasma edge. We discuss the strengths and weaknesses of the L-H transition model and suggest further development. Due to the found complications, the control research question revealed that the backstepping method is not sufficiently developed for application to the plasma model. Yet, the gained insight provides sufficient ground to motivate control development using other areas of control engineering.

Plasma model

There are many mature and recent models for the L-H transition that can be used for numerical purpose [97, 23, 49, 47, 99], some of which are validated experimentally. However, the L-H transition model developed by Weymiens et al. [99] forms the backbone for this study due to several reasons.

- The spatial dimensionality (1D) of the plasma behavior varies strongly near the transport barrier and separatrix. This presents the challenge to control engineering of dealing with a distributed parameter system.
- The bifurcation analyses compensate for a lack of experimental validation. The results and approaches thereof are extensively used during the model analysis.
- It should be noted that we require more extensive knowledge of the radial electric field dynamics for implementation on a fusion experiment.

This motivates further development to a physics-based model that allows experimental validation. This idea is substantiated by the following observations.

- The physics-based equation for electric field reveals the parametric dependence of model parameters on the plasma state. A validated model allows to assess the parametric uncertainty, which can be dealt with by control engineering.
- Accurate measurements of plasma edge temperature and density become increasingly vital due to their influence on electric field model uncertainty.
- A recent validation study by Kobayashi et al. [91] considered an electric field model based on the nonambipolar processes considered for the physics research question. Their result indicates that the observed radial current and electric field can be described by the model, albeit with uncertainty of $\sim 40\%$.

Control objective

The main issue for control resides in modeling and observing the radial electric field.

- There are several actuators that may influence the electric field equation, e.g., resonant magnetic perturbations, neutral gas puffing. Their inclusion in the model introduces an additional control input for the electric field.
- Measurements of electric field are mostly too inaccurate for control due to large and fast fluctuations, which makes output-based control difficult. However, an observer-based approach requires accurate determination of parameters on the other hand.

- The developments in control-oriented modeling of transport [22, 4, 14] could present a solution to determine the plasma temperature and density more accurately at the plasma edge. This is vital to model-based control of the electric field.
- The control-oriented model could be specialized to a specific fusion experiment, or even discharge regime, to increase model validity and reduce uncertainty. However, note that this requires more knowledge of the power threshold hysteresis in the tokamak experiments.

Backstepping p.d.e. control

The backstepping p.d.e. design has been thoroughly investigated to find possibilities to increase the design freedom. This issue has consumed the major amount of time for the part on control design of this study. In contrast to the original design procedure [78], we find that the kernel problem is overdetermined by six boundary conditions. The difference relies in the boundary condition for the plasma model, of which it is not justifiable to assume an homogeneous case.

- The degrees of freedom are insufficient when the target system contains Neumann- or Robin-type boundary conditions such as the L-H transition model. The full-state feedback design of Vazquez and Krstic [78] considers Dirichlet boundary actuation with proposed further development towards Neumann-type boundary condition.
- The boundary advection term is included to solve the overdetermination problem. However, the formulation of analytical conditions is thereby not possible without analyzing the kernel transformation explicitly. The numerical approach formulated to counter this problem does lead to a stabilizing control law, but constitutes an inefficient method for the control engineer during the control design.

The inclusion of the boundary advection term complicates the stability analysis of the target system, which is vital to find a stabilizing boundary feedback control.

- There is a cyclic relationship that complicates the stability analysis when the boundary advection is included. The stability bound is used to define the damping, which allows to solve the kernel problem. In turn, the kernel solution determines the boundary advection, which may lead to an unstable contribution to the target system. This contribution enters the stability analysis and hence, may show that the target system with boundary advection is unstable.
- To break this cyclic relation, we assume that the boundary advection is bounded and the bound is not strongly dependent of the damping. However, this is not completely verified in retrospect,

Analysis of the kernel problem consumed a significant amount of time, which has mainly contributed to mathematical analysis of the kernel problem. This contribution to the backstepping p.d.e. theory is rewarding, since it reveals many difficulties and restrictions when the backstepping design is applied to an involved physics-based model. Often, the theory is applied to much more investigated mathematical p.d.e. of which the feasibility has been determined, e.g., the heat equation, wave equation or Schrodinger's equation. As for control engineering, it is rewarding to focus on more mature p.d.e. boundary control theories, e.g., LQR or the port-Hamiltonian approach [31], or o.d.e. methods for boundary control.

Appendix A

Nonambipolar particle fluxes

This section describes the physical mechanisms and mathematical expressions underlying various non-ambipolar particle fluxes, which are used to define the basis for the electric field p.d.e. derivation in § 2.4. The tokamak and plasma parameters are defined for JET in § A.1 and used throughout this section for numerical evaluation. The considered nonambipolar particle fluxes are separated into terms involving the electric field, density gradient and temperature gradient in § A.2 to § A.9. Eventually, each set of parameters affecting one of the plasma variables is then contained in a separate function to retain conciseness of the derivation in § 2.6.

Note that the nonambipolar fluxes that can be found in H-mode literature are mentioned here, but we use only the processes that are stated in (2.9) for the derivation. Throughout the analysis, we assume equal density and temperature for each species, i.e., $n \approx n_i \approx n_e$ and $T \approx T_i \approx T_e$. Whenever expressions are evaluated, we use the last closed flux surface as the location at the plasma edge, which in the model means $x = a$ for the spatial coordinate.

A.1 Tokamak and plasma parameters

As a case study, we use JET parameters whenever there are tokamak parameters involved in a calculation or comparison. The size dimensions are, in descending order in Table A.1, the major radius R and (vertical/horizontal) minor radius $a_{v,h}$ [58]. The plasma current I_p and toroidal magnetic field at major radius B_t are also assumed to be fixed parameters [58]. Furthermore, the (unscaled) radial e-folding lengths at the scrape-off layer, $\hat{\lambda}_n$ and $\hat{\lambda}_T$, correspond to the MkIIGB divertor configuration [96]. Additionally, the pedestal density and temperature, n_{ped} and T_{ped} [eV], have been obtained from H-L transition experiments in a JET H-mode plasma [12].

Table A.1: Tokamak and plasma parameters for JET [58][12].

Parameter	R_0	a_v	a_h	$\hat{\lambda}_n$	$\hat{\lambda}_T$	I_p	B_t	n_{ped}	T_{ped}
Value	2.96	2.10	1.25	0.020	0.015	3.20	3.45	10^{19}	10^3

The mean minor radius is determined by assuming an ellipsoidal shape of the plasma poloidal cross section, which gives the (mean) aspect ratio ϱ .

$$a_m = \sqrt{\frac{a_h^2 + a_v^2}{2}} \approx 1.728 \text{ [m]} \quad (\text{A.1})$$

$$\varrho = \frac{a_m}{R_0} \approx 1.33 \quad (\text{A.2})$$

Using the plasma current I_p , the poloidal magnetic field can be calculated from Ampere's law assuming a circular plasma shape,

$$B_p = \frac{\mu_0 I_p}{2\pi a_m} \approx 0.37 \text{ [T]}, \quad (\text{A.3})$$

and the safety factor becomes,

$$q = \frac{\varrho B_t}{B_p} \approx 12. \quad (\text{A.4})$$

Formulae for plasma parameters are adopted from Freidberg [37], which yields scaling laws for the electron-ion and ion-ion collision frequencies,

$$\nu_{ei} = 1.33 \cdot 10^5 \left(\frac{n \cdot 10^{-20}}{T \cdot 10^{-3}} \right)^{3/2}, \quad \nu_{ii} = 1.2 \left(\frac{m_e}{m_i} \right)^{1/2} \nu_{ei}, \quad (\text{A.5})$$

the effective collision frequencies,

$$\nu_{*i} = \frac{\nu_{ii}}{\omega_{bi}}, \quad \omega_{bi} = \frac{\varrho^{3/2} v_{Ti}}{qR} \quad (\text{A.6})$$

$$\nu_{*e} = \frac{\nu_{ei}}{\omega_{be}}, \quad \omega_{be} = \frac{\varrho^{3/2} v_{Te}}{qR}. \quad (\text{A.7})$$

The effective detrapping frequency of ions and the ion-neutral collision frequency near the X-point of the separatrix are given as [87],

$$\nu_{\text{eff}} = \nu_{ii} + \nu_{in_0}, \quad \nu_{in_0} = \alpha_{in_0} \omega_{bi}, \quad \alpha_{in_0} = \frac{n_0}{n_{\text{ped}}}, \quad (\text{A.8})$$

where the neutral density n_0 at the X-point is estimated assuming that the neutral-ion collisions induce the ionization,

$$n_0 = 4 \cdot 10^{17} \alpha_{in_0} \left(\frac{T}{10^2} \right)^{3/4}. \quad (\text{A.9})$$

A.2 Polarization current

A polarization current is generated whenever the rate of change of the electric field is non-zero, which can be seen from Maxwell's addition to Ampere's law. The polarization current has been used for tokamak plasma modelling by, i.a., [90], whom define the neoclassical polarization current as

$$e\Gamma_i^{\text{pol}} = \frac{\sum_s m_s n_s}{B^2} \frac{\partial E_r}{\partial t}, \quad (\text{A.10})$$

in which the mass density, $m_s n_s$, in a two-fluid hydrogenic plasma is dominated by the ions. Simplifying the mass density to $m_i n_i$, it can be seen that the ions dictate the time scale of neutralization:

$$e\Gamma_i^{\text{pol}} \approx \frac{m_i n_i}{B^2} \frac{\partial E_r}{\partial t}. \quad (\text{A.11})$$

This definition of the polarization current is used throughout this thesis, which also has been noted by Weymiens [99].

A.3 Ion (perpendicular) shear viscosity

The ion shear viscosity constitutes the perpendicular component of the viscous stress tensor. In the L-H transition model, its main effect is to couple the L- and H-mode solution in the spatial domain. This is because the ion viscosity coefficient is presumably of the same order as the polarization time scale $\varepsilon \sim \mu$. As can be found in Itoh [83], the shear viscosity can be expressed, for example, as,

$$\begin{aligned} J^{\pi\perp} &= \nabla \left(\frac{e\rho_p n_i}{v_{T_i}} \mu_i \nabla \left(\frac{E_r}{B_p} \right) \right) \\ &= \nabla \left(\frac{m_i n_i}{B_p^2} \mu_i \nabla E_r \right) \end{aligned} \quad (\text{A.12})$$

Taking the inner product of the ion shear viscosity expression defined in [64] with the radial unit vector \vec{e}_r yields, in slab coordinates,

$$e\Gamma_i^{\pi\perp} = -\varepsilon_0 \varepsilon_\perp \frac{\partial}{\partial x} \left(\mu_i \frac{\partial E_r}{\partial x} \right), \quad (\text{A.13})$$

with the ion shear viscosity coefficient μ_i and the perpendicular permittivity of the plasma ε_\perp . Using the definition of perpendicular permittivity in [90], the factor $\varepsilon_0 \varepsilon_\perp$ reduces to,

$$\varepsilon_0 \varepsilon_\perp = \varepsilon_0 \left(1 + \sum_s \frac{m_s n_s}{\varepsilon_0 B_p^2} \right) \approx \frac{m_i n_i}{B_p^2}, \quad (\text{A.14})$$

with $m_i \gg m_e$ and $n_i \approx n_e$. Expressing $\varepsilon_0 \varepsilon_\perp$ in terms of plasma parameters, using equation (A.14), leads to

$$e\Gamma_i^{\pi\perp} \approx -\frac{m_i n_i}{B_p^2} \frac{\partial}{\partial x} \left(\mu_i \frac{\partial E_r}{\partial x} \right). \quad (\text{A.15})$$

Clearly, both expressions lead to an equivalent result under the assumption that the density derivative can be excluded from the derivative. Furthermore, the authors of [83] and [64] have assumed a constant shear viscosity coefficient. We introduce a general expression for the shear viscosity in the derivation:

$$e\Gamma_i^{\pi\perp} \approx -\frac{\partial}{\partial x} \left(\frac{m_i n_i \mu_i}{B_p^2} \frac{\partial E_r}{\partial x} \right). \quad (\text{A.16})$$

A.4 Ion (parallel) bulk viscosity

Toroidal plasma flow is unimpeded in an axisymmetric magnetic field, but axisymmetry is broken in a tokamak by, for example, the finite number of toroidal field coils [33]. Non-axisymmetric components of the magnetic field cause damping of the plasma flow parallel to the magnetic field by transit-time magnetic pumping, ripple-trapping and center drift of banana orbits. Around the L-H transition, the poloidal flow is supposed to change quickly due to the $\mathbf{E} \times \mathbf{B}$ force, while the toroidal flow and pressure gradient remain roughly constant. The poloidal plasma flow, however, is damped on the ion-ion collision time scale. Therefore, the bulk (parallel) plasma flow is damped mainly in the poloidal direction and leads to a radial current or flux surface-averaged viscous torque [52],

$$e\Gamma_i^{\pi\parallel} = \langle \mathbf{B}_p \cdot \nabla \cdot \pi \rangle = \frac{\sqrt{\pi}}{4} \frac{\rho^2}{r} n_i m_i v_{T_i} B (\xi_p u_p + \xi_t u_{p0}) \quad (\text{A.17})$$

with u poloidal flow velocities and $\xi_{p,t}$ geometric integrals. The angular brackets $\langle \dots \rangle$ indicate that the quantity is averaged over a flux surface. The poloidal flow velocities u_{pm} , u_p and u_{p0} are expressed as,

$$u_{pm} = Z \quad (\text{A.18})$$

$$\begin{aligned} u_p &= \frac{v_{T_i} B_p}{B} \left(u_{pm} + \frac{\rho_{pi}}{2} \left(\frac{1}{p_i} \frac{\partial p_i}{\partial x} \right) \right) \\ &= \frac{v_{T_i} B_p}{B} \left(Z + \frac{\rho_{pi}}{2} \left(\frac{1}{n_i} \frac{\partial n_i}{\partial x} + \frac{1}{T_i} \frac{\partial T_i}{\partial x} \right) \right) \end{aligned} \quad (\text{A.19})$$

$$u_{p0} = -\frac{\rho_{pi} v_{T_i}}{2} \left(\frac{1}{T_i} \frac{\partial T_i}{\partial x} \right) \quad (\text{A.20})$$

with the ion pressure $p_i = n_i T_i$ and the geometric integrals $\xi_{p,t}$ containing the $\mathbf{E} \times \mathbf{B}$ -induced poloidal flow u_{pm} ,

$$\begin{pmatrix} \xi_p \\ \xi_t \end{pmatrix} = \frac{1}{\pi} \int_0^{\nu_{*i}^{1/2}} \begin{pmatrix} 1 \\ \frac{5}{2} - x \end{pmatrix} x^2 \exp(-x) \int_{-1}^1 \frac{\nu_{*i} \varrho^{3/2} (\nu_{ei}/\nu_{ii} \sqrt{x})}{(y + u_{pm}/\sqrt{x})^2 + (\nu_{*i} \varrho^{3/2} (\nu_{ei}/\nu_{ii} \sqrt{x}))^2} dx dy. \quad (\text{A.21})$$

Although the bulk poloidal flow relaxes to a temperature gradient-driven poloidal flow on the ion-ion collision time scale, the $\mathbf{E} \times \mathbf{B}$ flow may approach velocities near the sound speed causing decay of the viscosity [40]. Therefore, the ion bulk viscosity is considered in L-H bifurcation models [53][87], which can be expressed in terms of normalized electric field and spatial derivatives as,

$$e\Gamma^{\pi\parallel} = \frac{\sqrt{\pi}}{4} \frac{\varrho^2}{r} n m_i v_{T_i} B \left(\xi_p \left(\frac{v_{T_i} B_p}{B} \right) \left(Z + \frac{\rho_{pi}}{2} \left(\frac{1}{n} \frac{\partial n}{\partial x} + \frac{1}{T} \frac{\partial T}{\partial x} \right) \right) - \xi_t \left(\frac{\rho_{pi} v_{T_i}}{2} \right) \left(\frac{1}{T} \frac{\partial T}{\partial x} \right) \right) \quad (\text{A.22})$$

$$:= g_n^{\pi\parallel} \frac{1}{n} \frac{\partial n}{\partial x} + g_T^{\pi\parallel} \frac{1}{T} \frac{\partial T}{\partial x} + g_Z^{\pi\parallel} Z, \quad (\text{A.23})$$

where the index i has been removed from the plasma variables. As such, the functions $g^{\pi\parallel}$ are denoted for conciseness as,

$$g_n^{\pi\parallel} = \frac{\sqrt{\pi}}{8} \frac{\varrho^2}{a_m} n m_i \rho_{pi} (v_{T_i})^2 B_p \xi_p \quad (\text{A.24})$$

$$g_T^{\pi\parallel} = \frac{\sqrt{\pi}}{8} \frac{\varrho^2}{a_m} n m_i \rho_{pi} (v_{T_i})^2 (B_p \xi_p - B \xi_t) \quad (\text{A.25})$$

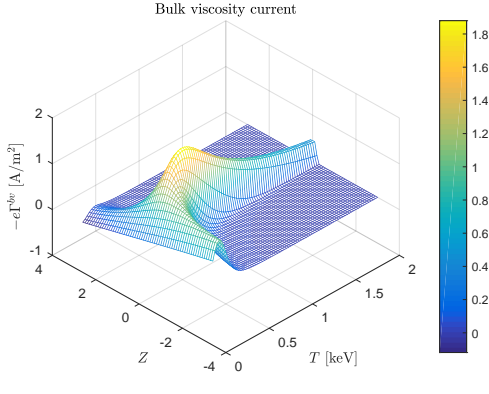
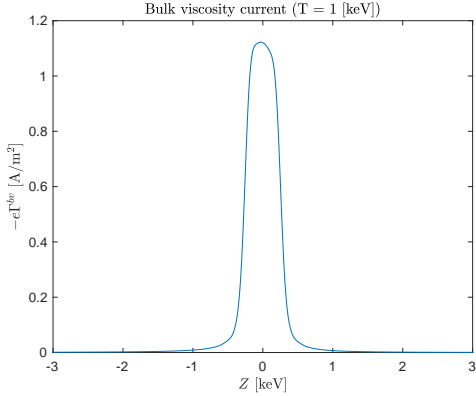
$$g_Z^{\pi\parallel} = \frac{\sqrt{\pi}}{4} \frac{\varrho^2}{a_m} n m_i (v_{T_i})^2 B_p \xi_p \quad (\text{A.26})$$

In the regime considered for plasma variables (T, Z) , the bulk viscosity multiplied by -1 is depicted in Figure A.1 for $T \in [0.1, 2.0]$ [keV] and for fixed $T = T_{\text{ped}}$ in Figure A.2. Both figures show the bulk viscosity current for a fixed $n = n_{\text{ped}}$ at the radial location $x = a_m$, such that the boundary conditions for the density and temperature gradient apply. As can be seen from Figure A.1, the bulk viscosity decays clearly with temperature, while the width in Z direction decreases as well.

A.5 Residual Reynolds stress

Turbulent fluctuations cause perturbations to the plasma flow, of which the velocity components are correlated under gradient-driven transport [73]. If the fluctuations are coherent and spatially varying (i.e. a radial gradient exists), a nonzero Reynolds stress causes acceleration of the poloidal flow [73] relating to fluctuations of the electric field [11] as,

$$\frac{\partial v_\theta}{\partial t} = -(\tilde{\mathbf{v}} \cdot \nabla \tilde{\mathbf{v}})_\theta = -\frac{\partial}{\partial r} (\tilde{v}_r \tilde{v}_\theta) = \frac{\partial}{\partial r} \left(\frac{\tilde{E}_r \tilde{E}_\theta}{B^2} \right) \quad (\text{A.27})$$


 Figure A.1: Bulk viscosity in the T, Z space.

 Figure A.2: Bulk viscosity at $T_{\text{ped}} = 1$ [keV].

Turbulent Reynolds stress has been invoked as a mechanism for zonal flow generation, and its importance has been established in experiments [105] as well as L-H transition theories [70]. Because turbulent Reynolds stress has a key role in zonal flow drive [25][49], it can also be considered as a precursor to the L-H transition [88].

A.6 Electron anomalous diffusion

Turbulent fluctuations can also drive a nonambipolar flux, because these may interact differently with ions and electrons [5]. For example, when drift wave turbulence preferentially removes electron momentum across the last closed flux surface [84], it essentially constitutes a nonambipolar electron flux [89],

$$e\Gamma_e^{\text{an}} = -en_e D_e \left(\frac{1}{n_e} \frac{\partial n_e}{\partial x} + \frac{\alpha_{\text{an}}}{T_e} \frac{\partial T_e}{\partial x} + \frac{eE_r}{T_e} \right) \quad (\text{A.28})$$

with $\alpha_{\text{an}} \sim 1$ a numerical coefficient and D_e the anomalous diffusion coefficient [93],

$$D_e = \frac{\pi^{1/2} \varrho^2 \rho_{pe} T_e}{2a_m B}, \quad (\text{A.29})$$

which is bounded to the range $\sim 0.1 - 10$ for the temperatures considered. Now, separating the terms that involve one of the plasma variables leads to an expression for Γ^{an} in terms of functions g^{an} ,

$$e\Gamma^{\text{an}} := g_n^{\text{an}} \frac{1}{n} \frac{\partial n}{\partial x} + g_T^{\text{an}} \frac{1}{T} \frac{\partial T}{\partial x} + g_Z^{\text{an}} Z \quad (\text{A.30})$$

$$g_n^{\text{an}} = -enD_{an}, \quad g_T^{\text{an}} = -enD_{an}\alpha_{an}, \quad g_Z^{\text{an}} = \frac{-enD_{an}}{\rho_{pi}} \quad (\text{A.31})$$

$$D_{an} = \frac{\pi^{1/2} \varrho^2 \rho_{pe} T}{2a_m B}. \quad (\text{A.32})$$

As can be seen from Figure A.3 and A.4, an increase of temperature steepens the anomalous current curve along the Z direction.

A.7 Ion orbit loss

A part of the ion population accesses orbits that cross the last closed flux surface, due to the radial extent of their gyro- or banana orbit. The collisionless part of the ion loss cone, therefore, yields

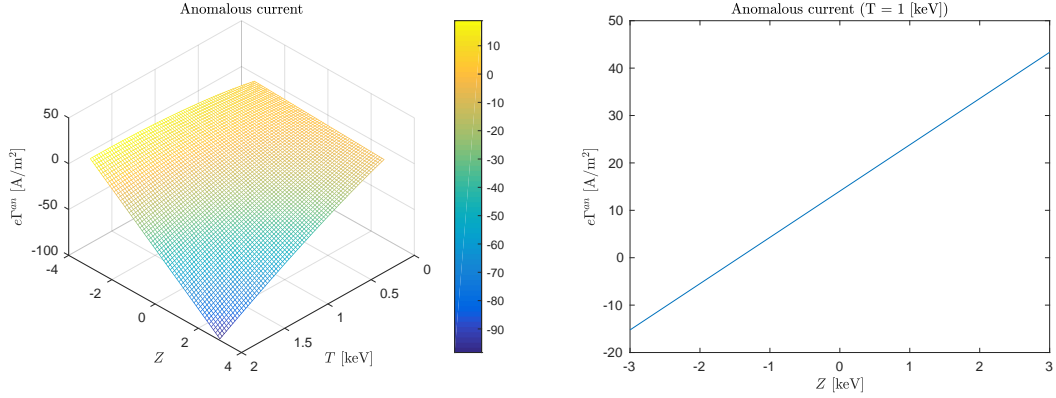


Figure A.3: Anomalous current in the T, Z space. Figure A.4: Anomalous current at $T_{\text{ped}} = 1$ [keV].

a nonambipolar ion flux, so-called (direct) ion orbit losses Γ_i^{ol} . Consequently, the ion orbit may be squeezed by the (negative) electric field, further complicating the dynamics. Ion orbit loss has been invoked often in literature for bifurcation of radial electric field [7][89][53], although it is not necessarily dominant [41][30]. Numerical simulations [94] and experiments [27][50][98] agree, at least qualitatively, with analytic expressions for ion orbit loss, for example from Shaing [52],

$$e\Gamma^{\text{ol}} = \frac{en_i\nu_{\text{eff}}\sqrt{\varrho}\rho_{pi}}{(\nu_{*i} + Z^4)^{1/2}} \exp\left(-(\nu_{*i} + Z^4)^{1/2}\right) \quad (\text{A.33})$$

$$g^{\text{ol}} = en\nu_{\text{eff}}\sqrt{\varrho}\rho_{pi} \quad (\text{A.34})$$

with ν_{eff} the effective detrapping frequency and ν_{*i} effective ion collision frequency. In Figure A.5, the orbit loss current has been depicted (negative) for the a grid of temperature and electric field values. The orbit loss curve does not change shape qualitatively when the temperature increases, but the peak value for zero electric field does increase at the expense of its width in Z direction. As can be seen from Figure A.6, the orbit loss current at a pedestal temperature of 1 [keV] is relevant in a narrow region of $|Z| < 1$ only.

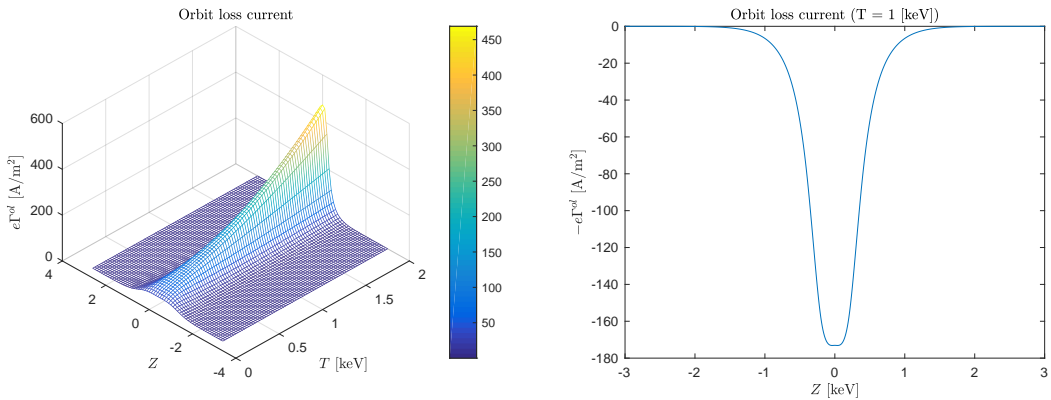


Figure A.5: Orbit loss current in the T, Z space. Figure A.6: Orbit loss current at $T_{\text{ped}} = 1$ [keV].

A.8 Charge exchange friction

The presence of neutral particles causes charge exchange with plasma ions and ionization by electron impact at the plasma edge. Since the charge exchange rate dominates over electron ionization impact [17], the loss of ion momentum results in a nonambipolar ion flux [87],

$$e\Gamma_i^{\text{cx}} = -\frac{m_i n_0 \langle \sigma v \rangle_{\text{cx}} n_i T_i}{B_p^2} \left(\frac{1}{n_i} \frac{\partial n_i}{\partial x} + \frac{\alpha_{\text{cx}}}{T_i} \frac{\partial T_i}{\partial x} - \frac{eE_r}{T_i} \right) \quad (\text{A.35})$$

with $\alpha_{\text{cx}} \sim 1$ a numerical coefficient. The neutral particle population changes dynamically on the ion collision time-scale, as charge exchange generates a ‘hot’ neutral population, while electron ionization impact produces a ‘cold’ ion population. A model for the spatial distribution of neutrals is derived in the Appendix A.3. Expressing (A.35) in terms of the gradients and electric field yields,

$$e\Gamma^{\text{cx}} := g_n^{\text{cx}} \frac{1}{n} \frac{\partial n}{\partial x} + g_T^{\text{cx}} \frac{1}{T} \frac{\partial T}{\partial x} + g_Z^{\text{cx}} Z, \quad (\text{A.36})$$

$$g_n^{\text{cx}} = -\frac{m_i n_0 \langle \sigma v \rangle_{\text{cx}} n T}{B_p^2}, \quad g_T^{\text{cx}} = -\frac{\alpha_{\text{cx}} m_i n_0 \langle \sigma v \rangle_{\text{cx}} n T}{B_p^2} \quad g_Z^{\text{cx}} = \frac{m_i n_0 \langle \sigma v \rangle_{\text{cx}} n T}{\rho_{pi} B_p^2} \quad (\text{A.37})$$

The charge exchange current is depicted in Figure A.7 for the temperature and electric field grid. With increasing temperature, the charge exchange curve steepens in the Z direction equivalent to the behavior of the anomalous current. The charge exchange contribution to the total current, however, becomes much more positive for negative Z values. In Figure A.8, the charge exchange current is shown for $T = T_{\text{ped}}$.

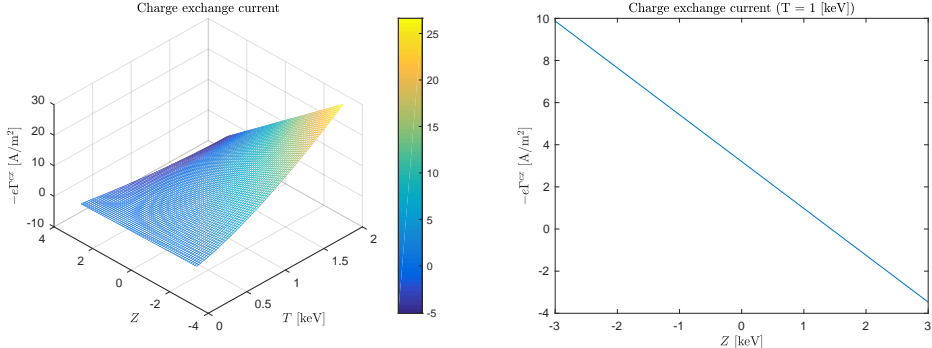


Figure A.7: Orbit loss current in the T, Z space.
Figure A.8: Orbit loss current at $T_{\text{ped}} = 1$ [keV].

A.9 Ion ripple loss

The process of ripple loss resembles the counterpart of direct orbit losses for toroidally trapped particles. Such particles transit between adjacent toroidal field coils, while their vertical drift contributes to the radial particle flux. Ripple loss is not limited to ions, for electrons may be lost by magnetic field ripples if the electric field is sufficiently large [44]. Because of the possible impact of ripple loss, the effect on plasma rotation and electric field have been studied on various fusion experiments [68][26]. Also ripple loss effects have been studied in earlier L-H bifurcation analyses, for example, given by Itoh [42] as,

$$\Gamma_s^{\text{rl}} = -\varrho^2 \varrho_h^{1/2} n_s v_D^2 \int_0^\infty dw \frac{w^{5/2} e^{-w} \nu_s(w)}{\nu_s^2 + 1.5 \sqrt{\varrho \varrho_h^{-1} \omega_{\text{rot}}^2}} \left(\frac{1}{n_s} \frac{\partial n_s}{\partial x} - \frac{eE_r}{T_s} + \frac{w - 3/2}{T_s} \frac{\partial T_s}{\partial x} \right) \quad (\text{A.38})$$

with s the plasma species under consideration. However, the toroidal ripple loss varies strongly with plasma collisionality, yielding a different expression for low, high or intermediate collision frequency [56].

Appendix B

Linearization

This section describes the linearization of the nonlinear p.d.e. system § 3.2, which is used to define the linear p.d.e. system in § 3.3. The linearization of the p.d.e. system is obtained about an arbitrary perturbed equilibrium $\hat{\mathbf{v}}(x, t) = \bar{\mathbf{v}}(x) + \epsilon\tilde{\mathbf{v}}(x, t)$ with $\epsilon \ll 1$, where the perturbed state vector for the linearized p.d.e. system is defined by:

$$\tilde{\mathbf{v}}(x, t) = \begin{bmatrix} \tilde{n}(x, t) \\ \tilde{T}(x, t) \\ \tilde{Z}(x, t) \end{bmatrix} \quad (\text{B.1})$$

The equilibrium solution $\bar{\mathbf{v}}(x)$ is time-independent and the perturbed state $\tilde{\mathbf{v}}(x, t)$ depends on both space and time. The formal procedure is as follows:

- (i) Substitute $\hat{\mathbf{v}}(x, t)$ for $\mathbf{v}(x, t)$ in the system of partial differential equations.
- (ii) Differentiate each term of each p.d.e. with respect to ϵ , respecting the chain rule.
- (iii) Let $\epsilon \rightarrow 0$ to obtain the linearized set of partial differential equations.

The nonlinear p.d.e. system is restated using the short-hand notation, which yields the p.d.e. system for the perturbed equilibrium $\hat{\mathbf{v}}$:

$$\begin{aligned} \hat{n}_t &= \partial_x \left(D(\hat{Z}_x) \hat{n}_x \right) \\ \hat{T}_t &= \partial_x \left(\frac{D(\hat{Z}_x)}{\zeta} \hat{T}_x \right) + \left(\frac{\zeta+1}{\zeta} \right) \frac{D(\hat{Z}_x)}{\hat{n}} \hat{n}_x \hat{T}_x \\ \hat{Z}_t &= \partial_x \left(\frac{\mu D(\hat{Z}_x)}{\varepsilon} \hat{Z}_x \right) + \frac{c_n \hat{T}}{\varepsilon \hat{n}^2} \hat{n}_x + \frac{c_T \hat{T}}{\varepsilon \hat{n}} \hat{T}_x + \frac{1}{\varepsilon} G(\hat{Z}) \end{aligned} \quad (\text{B.2})$$

Substitution of the perturbed equilibrium $\hat{\mathbf{v}}$ leads to the following partial differential equations, in which the equilibrium time derivatives are by definition $\bar{\mathbf{v}}_t(x) = 0$.

$$\epsilon\tilde{n}_t = \partial_x \left(D((\bar{Z} + \epsilon\tilde{Z})_x)(\bar{n} + \epsilon\tilde{n})_x \right) \quad (\text{B.3})$$

$$\epsilon\tilde{T}_t = \partial_x \left(\frac{D((\bar{Z} + \epsilon\tilde{Z})_x)}{\zeta} (\bar{T} + \epsilon\tilde{T})_x \right) + \left(\frac{\zeta+1}{\zeta} \right) \frac{D((\bar{Z} + \epsilon\tilde{Z})_x)}{(\bar{n} + \epsilon\tilde{n})} (\bar{n} + \epsilon\tilde{n})_x (\bar{T} + \epsilon\tilde{T})_x \quad (\text{B.4})$$

$$\begin{aligned} \epsilon\tilde{Z}_t &= \partial_x \left(\frac{\mu D((\bar{Z} + \epsilon\tilde{Z})_x)}{\varepsilon} (\bar{Z} + \epsilon\tilde{Z})_x \right) + \frac{c_n(\bar{T} + \epsilon\tilde{T})}{\varepsilon(\bar{n} + \epsilon\tilde{n})^2} (\bar{n} + \epsilon\tilde{n})_x + \frac{c_T}{\varepsilon(\bar{n} + \epsilon\tilde{n})} (\bar{T} + \epsilon\tilde{T})_x \\ &\quad + \frac{1}{\varepsilon} G(\bar{Z} + \epsilon\tilde{Z}) \end{aligned} \quad (\text{B.5})$$

Taking the derivative with respect to ϵ and letting $\epsilon \rightarrow 0$ leads to a set of linear p.d.e. for \tilde{n} , \tilde{T} and \tilde{Z} .

$$\tilde{n}_t = \partial_x \left(D(\bar{Z}_x) \tilde{n}_x + F(\bar{Z}_x) \bar{n}_x \tilde{Z}_x \right) \quad (\text{B.6})$$

$$\begin{aligned} \tilde{T}_t &= \partial_x \left(\frac{D(\bar{Z}_x)}{\zeta} \tilde{T}_x + \frac{F(\bar{Z}_x) \bar{T}_x}{\zeta} \tilde{Z}_x \right) \\ &\quad + \left(\left(\frac{\zeta+1}{\zeta} \right) \frac{D(\bar{Z}_x) \bar{T}_x}{\bar{n}} \right) \tilde{n}_x + \left(\left(\frac{\zeta+1}{\zeta} \right) \frac{D(\bar{Z}_x) \bar{n}_x}{\bar{n}} \right) \tilde{T}_x \\ &\quad + \left(\left(\frac{\zeta+1}{\zeta} \right) \frac{F(\bar{Z}_x) \bar{n}_x \bar{T}_x}{\bar{n}} \right) \tilde{Z}_x + \left(- \left(\frac{\zeta+1}{\zeta} \right) \frac{D(\bar{Z}_x) \bar{n}_x \bar{T}_x}{\bar{n}^2} \right) \tilde{n} \\ \tilde{Z}_t &= \partial_x \left(\frac{\mu D(\bar{Z}_x)}{\varepsilon} \tilde{Z}_x + \frac{\mu F(\bar{Z}_x) \bar{Z}_x}{\varepsilon} \tilde{Z}_x \right) + \left(\frac{c_n \bar{T}}{\varepsilon \bar{n}^2} \right) \tilde{n}_x + \left(\frac{c_T}{\varepsilon \bar{n}} \right) \tilde{T}_x \\ &\quad - \left(\frac{c_T \bar{T}_x}{\varepsilon \bar{n}^2} + \frac{2 c_n \bar{n}_x \bar{T}}{\varepsilon \bar{n}^3} \right) \tilde{n} + \left(\frac{c_n \bar{n}_x}{\varepsilon \bar{n}^2} \right) \tilde{T} + \left(\frac{b - 3(Z_S - \bar{Z})^2}{\varepsilon} \right) \tilde{Z} \end{aligned} \quad (\text{B.7})$$

The function $F(\bar{Z}_x)$ is used to denote the derivative of the diffusivity function $\partial_{\bar{Z}_x} D(\bar{Z}_x)$ with respect to the argument \bar{Z}_x :

$$F(\bar{Z}_x) = - \frac{2\alpha (D_{\max} - D_{\min}) \bar{Z}_x}{\left(1 + \alpha (\bar{Z}_x)^2\right)^2}. \quad (\text{B.9})$$

Also, the boundary condition at the s.o.l. is linearized accordingly yielding (B.10), where the e-folding lengths \bar{e}_i are introduced to distinguish from the reaction coefficients λ_{ij} .

$$\tilde{\mathbf{v}}_x(0, t) = \bar{E} \begin{bmatrix} \tilde{n}(0) \\ \tilde{T}(0) \\ \tilde{Z}(0) \end{bmatrix}, \quad \bar{E} = \begin{bmatrix} \bar{e}_1 & 0 & 0 \\ 0 & \bar{e}_2 & 0 \\ 0 & 0 & \bar{e}_3 \end{bmatrix} := \begin{bmatrix} \frac{1}{\lambda_n} & 0 & 0 \\ 0 & \frac{1}{\lambda_T} & 0 \\ 0 & 0 & \frac{1}{\lambda_Z} \end{bmatrix} \quad (\text{B.10})$$

The boundary conditions at the plasma core can be expressed in matrix format too, where $\lim_{x \rightarrow L} \bar{Z}_x = 0$ such that $D(\bar{Z}_x(L)) = D_{\max}$:

$$\tilde{\mathbf{v}}_x(L, t) = \begin{bmatrix} -\frac{1}{D_{\max}} \tilde{\Gamma}_c(t) \\ -\frac{\zeta(\gamma-1)}{D_{\max} \bar{n}(L)} \tilde{q}_c(t) + \frac{\zeta \bar{T}(L)}{D_{\max} \bar{n}(L)} \tilde{\Gamma}_c(t) - \frac{\bar{T}_x(L)}{\bar{n}(L)} \tilde{n}(L, t) + \frac{\zeta \bar{\Gamma}_c}{D_{\max} \bar{n}(L)} \tilde{T}(L, t) \\ 0 \end{bmatrix}. \quad (\text{B.11})$$

The linearized set of p.d.e. (B.6) in combination with the boundary conditions (B.10) and (B.11) are used to define the linear p.d.e. system in § 3.3.

Appendix C

Spatial derivatives of eigendecomposition

The coefficient matrices of the reference p.d.e. system § 3.4.1 contain the first and second spatial derivative of the eigenvector matrix $Q(x)$. Note that we use a superscript notation throughout this appendix due to the subscript derivative notation. The (first-order) spatial derivative of the eigenvector matrix $Q_x(x)$ is calculated as

$$Q_x(x) := \partial_x(Q(x)) = \begin{bmatrix} 0 & 0 & \frac{\bar{\sigma}_x^{13}\partial_x(\bar{\sigma}^{11} - \bar{\sigma}^{33})}{(\bar{\sigma}^{11} - \bar{\sigma}^{33})^2} - \frac{\bar{\sigma}_x^{13}}{\bar{\sigma}^{11} - \bar{\sigma}^{33}} \\ 0 & 0 & \frac{\bar{\sigma}_x^{23}\partial_x(\bar{\sigma}^{22} - \bar{\sigma}^{33})}{(\bar{\sigma}^{22} - \bar{\sigma}^{33})^2} - \frac{\bar{\sigma}_x^{23}}{\bar{\sigma}^{22} - \bar{\sigma}^{33}} \\ 0 & 0 & 0 \end{bmatrix}, \quad (\text{C.1})$$

$$Q_x^{-1}(x) := \partial_x(Q^{-1}(x)) = -Q_x(x) \quad (\text{C.2})$$

with the first-order spatial derivatives of $\bar{\sigma}^{ij}(x)$

$$\bar{\sigma}_x^{11}(x) := \partial_x(\bar{\sigma}^{11}(x)) = F(\bar{Z}_x)\bar{Z}_{xx} \quad (\text{C.3})$$

$$\bar{\sigma}_x^{22}(x) := \partial_x(\bar{\sigma}^{22}(x)) = \frac{F(\bar{Z}_x)\bar{Z}_{xx}}{\zeta} \quad (\text{C.4})$$

$$\bar{\sigma}_x^{33}(x) := \partial_x(\bar{\sigma}^{33}(x)) = \frac{2\mu F(\bar{Z}_x)\bar{Z}_{xx}}{\varepsilon} + \frac{\mu F_x(\bar{Z}_x)\bar{Z}_x}{\varepsilon} \quad (\text{C.5})$$

$$\bar{\sigma}_x^{13}(x) := \partial_x(\bar{\sigma}^{13}(x)) = F_x(\bar{Z}_x)\bar{n}_x + F(\bar{Z}_x)\bar{n}_{xx} \quad (\text{C.6})$$

$$\bar{\sigma}_x^{23}(x) := \partial_x(\bar{\sigma}^{23}(x)) = \frac{F_x(\bar{Z}_x)\bar{T}_x}{\zeta} + \frac{F(\bar{Z}_x)\bar{T}_{xx}}{\zeta}, \quad (\text{C.7})$$

and, $F_x(\bar{Z}_x)$, the spatial derivative of $F(\bar{Z}_x)$ defined for conciseness,

$$\begin{aligned} F_x(\bar{Z}_x) := \partial_x(F(\bar{Z}_x)) &= \frac{8\alpha^2(D_{\max} - D_{\min})\bar{Z}_x^2\bar{Z}_{xx}}{(1 + \alpha\bar{Z}_x^2)^3} - \frac{2\alpha(D_{\max} - D_{\min})\bar{Z}_{xx}}{(1 + \alpha\bar{Z}_x^2)^2} \\ &= F(\bar{Z}_x) \left(\frac{1}{\bar{Z}_x} - \frac{4\alpha\bar{Z}_x}{1 + \alpha\bar{Z}_x^2} \right) \bar{Z}_{xx} \\ &= F(\bar{Z}_x) \left(\frac{1 - 3\alpha\bar{Z}_x^2}{(1 + \alpha\bar{Z}_x^2)\bar{Z}_x} \right) \bar{Z}_{xx} \end{aligned} \quad (\text{C.8})$$

with the function $F(\bar{Z}_x)$ given in equation (B.9). The second-order spatial derivative of the eigenvector matrix $Q_{xx}(x)$ and its inverse $Q_{xx}^{-1}(x)$ are determined as

$$\begin{aligned} Q_{xx}(x) &:= \partial_x(Q_x(x)) \\ &= \begin{bmatrix} 0 & 0 & \frac{2\bar{\sigma}_x^{13}(\bar{\sigma}_x^{11} - \bar{\sigma}_x^{33})}{(\bar{\sigma}^{11} - \bar{\sigma}^{33})^2} - \frac{2\bar{\sigma}^{13}(\bar{\sigma}_x^{11} - \bar{\sigma}_x^{33})^2}{(\bar{\sigma}^{11} - \bar{\sigma}^{33})^3} - \frac{\bar{\sigma}_{xx}^{13}}{\bar{\sigma}^{11} - \bar{\sigma}^{33}} + \frac{\bar{\sigma}^{13}(\bar{\sigma}_{xx}^{11} - \bar{\sigma}_{xx}^{33})}{(\bar{\sigma}^{11} - \bar{\sigma}^{33})^2} \\ 0 & 0 & \frac{2\bar{\sigma}_x^{23}(\bar{\sigma}_x^{22} - \bar{\sigma}_x^{33})}{(\bar{\sigma}^{22} - \bar{\sigma}^{33})^2} - \frac{2\bar{\sigma}^{23}(\bar{\sigma}_x^{22} - \bar{\sigma}_x^{33})^2}{(\bar{\sigma}^{22} - \bar{\sigma}^{33})^3} - \frac{\bar{\sigma}_{xx}^{23}}{\bar{\sigma}^{22} - \bar{\sigma}^{33}} + \frac{\bar{\sigma}^{23}(\bar{\sigma}_{xx}^{22} - \bar{\sigma}_{xx}^{33})}{(\bar{\sigma}^{22} - \bar{\sigma}^{33})^2} \\ 0 & 0 & 0 \end{bmatrix} \quad (\text{C.9}) \\ Q_{xx}^{-1}(x) &:= \partial_x(Q_x^{-1}(x)) = -\partial_x(Q_x(x)) = -Q_{xx}(x) \quad (\text{C.10}) \end{aligned}$$

with the second-order spatial derivatives of the diffusion coefficients

$$\bar{\sigma}_{xx}^{11}(x) := \partial_{xx}(\bar{\sigma}^{11}(x)) = F_x(\bar{Z}_x)\bar{Z}_{xx} + F(\bar{Z}_x)\bar{Z}_{xxx} \quad (\text{C.11})$$

$$\bar{\sigma}_{xx}^{22}(x) := \partial_{xx}(\bar{\sigma}^{22}(x)) = \frac{F_x(\bar{Z}_x)\bar{Z}_{xx}}{\zeta} + \frac{F(\bar{Z}_x)\bar{Z}_{xxx}}{\zeta} \quad (\text{C.12})$$

$$\bar{\sigma}_{xx}^{33}(x) := \partial_{xx}(\bar{\sigma}^{33}(x)) = \frac{3\mu F_x(\bar{Z}_x)\bar{Z}_{xx}}{\varepsilon} + \frac{2\mu F(\bar{Z}_x)\bar{Z}_{xxx}}{\varepsilon} + \frac{\mu F_{xx}(\bar{Z}_x)\bar{Z}_x}{\varepsilon} \quad (\text{C.13})$$

$$\bar{\sigma}_{xx}^{13}(x) := \partial_{xx}(\bar{\sigma}^{13}(x)) = F_{xx}(\bar{Z}_x)\bar{n}_x + 2F_x(\bar{Z}_x)\bar{n}_{xx} + F(\bar{Z}_x)\bar{n}_{xxx} \quad (\text{C.14})$$

$$\bar{\sigma}_{xx}^{23}(x) := \partial_{xx}(\bar{\sigma}^{23}(x)) = \frac{F_{xx}(\bar{Z}_x)\bar{T}_x}{\zeta} + \frac{2F_x(\bar{Z}_x)\bar{T}_{xx}}{\zeta} + \frac{F(\bar{Z}_x)\bar{T}_{xxx}}{\zeta} \quad (\text{C.15})$$

and, $F_{xx}(\bar{Z}_x)$, the second-order spatial derivative of $F(\bar{Z}_x)$:

$$\begin{aligned} F_{xx}(\bar{Z}_x) &:= \partial_x(F_x(\bar{Z}_x)) \\ &= F_x(\bar{Z}_x) \left(\frac{1 - 3\alpha\bar{Z}_x^2}{(1 + \alpha\bar{Z}_x^2)\bar{Z}_x} \right) \bar{Z}_{xx} + F(\bar{Z}_x)\partial_x \left(\frac{1 - 3\alpha\bar{Z}_x^2}{(1 + \alpha\bar{Z}_x^2)\bar{Z}_x} \right) \bar{Z}_{xx} + F(\bar{Z}_x) \left(\frac{1 - 3\alpha\bar{Z}_x^2}{(1 + \alpha\bar{Z}_x^2)\bar{Z}_x} \right) \bar{Z}_{xxx} \\ &= \frac{F_x^2(\bar{Z}_x)}{F(\bar{Z}_x)} + F(\bar{Z}_x) \left(-\frac{2\alpha(1 - 3\alpha\bar{Z}_x^2)}{(1 + \alpha\bar{Z}_x^2)^2} - \frac{6\alpha}{1 + \alpha\bar{Z}_x^2} - \frac{1 - 3\alpha\bar{Z}_x^2}{(1 + \alpha\bar{Z}_x^2)\bar{Z}_x^2} \right) \bar{Z}_{xx}^2 + \frac{F_x(\bar{Z}_x)\bar{Z}_{xxx}}{\bar{Z}_{xx}} \\ &= \frac{F_x^2(\bar{Z}_x)}{F(\bar{Z}_x)} + F(\bar{Z}_x) \left(\frac{3\alpha^2\bar{Z}_x^4 - 6\alpha\bar{Z}_x^2 - 1}{(1 + \alpha\bar{Z}_x^2)^2\bar{Z}_x^2} \right) \bar{Z}_{xx}^2 + \frac{F_x(\bar{Z}_x)\bar{Z}_{xxx}}{\bar{Z}_{xx}}. \quad (\text{C.16}) \end{aligned}$$

The partial derivatives of the eigendecomposition are used in § 3.4.

Appendix D

Characteristic o.d.e. for the kernel problem

To determine the allowed number of boundary conditions for the kernel system in § 4.2, we derive the set of characteristic o.d.e. for the kernel p.d.e. (4.30) with additional conditions (4.31)-(4.33). The method of characteristics aims to convert the p.d.e. into a system of o.d.e. [55], which can be solved for. First, we rewrite the kernel p.d.e. set such that lower-order terms arrive at the right-hand side,

$$\partial_x (\Sigma(x)K_x) - \partial_\xi (K_\xi \Sigma(\xi)) = -\partial_\xi (K\Phi(\xi)) - \Phi(x)K_x + K\Lambda(\xi) + C(x)K := H(x, \xi) \quad (\text{D.1})$$

or component-wise,

$$\partial_x (\sigma_{ii}(x)k_x^{ij}) - \partial_\xi (k_\xi^{ij} \sigma_{jj}(\xi)) = \sum_{m=1}^n (-\partial_\xi (k_{im}\phi_{mj}(\xi)) - \phi_{im}(x)k_x^{mj} + k_{im}\lambda_{mj}(\xi) + c_{im}(x)k_{mj}). \quad (\text{D.2})$$

Note that the spatial dependence of $K = K(x, \xi)$ is left out for brevity. To investigate whether a solution to (D.1) exists, we have to look for a solution to the homogeneous equation only, i.e., the right-hand side is set to zero. If a homogeneous solution exists, then there is at least one solution for the particular equation. The diagonal structure of the diffusion matrix $\Sigma(\cdot)$ results in a decoupled system of N equations for each $k_{ij}(x, \xi)$:

$$\partial_x (\sigma_{ii}(x)k_x^{ij}) - \partial_\xi (\sigma_{jj}(\xi)k_\xi^{ij}) = 0, \quad \text{for } 1 \leq i, j \leq 3. \quad (\text{D.3})$$

This homogeneous form of the kernel p.d.e. constitutes a conservation law in non-divergence form. Otherwise stated, the kernel problem can be written as a first-order system of conservation laws [55]

$$\mathbf{k}_\xi + B(x, \xi)\mathbf{k}_x = 0, \quad (\text{D.4})$$

where the matrix $B(x, \xi) : \mathbb{R}^2 \rightarrow \mathbb{M}^{2 \times 2}$. Then, the vector solution $\mathbf{k}(x, \xi)$ needs to have the form

$$\mathbf{k}(x, \xi) := \begin{bmatrix} \sigma_{ii}(x)k_x^{ij} \\ \sigma_{jj}(\xi)k_\xi^{ij} \end{bmatrix} \quad (\text{D.5})$$

to reconstruct the kernel p.d.e. of (D.3). From here on forward, k^{ij} is denoted as k , since (D.4) holds for any kernel function $1 \leq i, j \leq 3$. Taking the partial derivative in the ξ and x direction yields

$$\mathbf{k}_\xi = \partial_\xi (\mathbf{k}(x, \xi)) = \begin{bmatrix} \sigma_{ii}(x)k_{x\xi} \\ \partial_\xi (\sigma_{jj}(\xi)k_\xi) \end{bmatrix}, \quad \mathbf{k}_x = \partial_x (\mathbf{k}(x, \xi)) = \begin{bmatrix} \partial_x (\sigma_{ii}(x)k_x) \\ \sigma_{jj}(\xi)k_{\xi x} \end{bmatrix} \quad (\text{D.6})$$

which shows that the kernel p.d.e. can be put in the conservation law form of (D.4):

$$\mathbf{k}_\xi = \begin{bmatrix} 0 & \frac{\sigma_{ii}(x)}{\sigma_{jj}(\xi)} \\ 1 & 0 \end{bmatrix} \mathbf{k}_x \implies \mathbf{k}_\xi + \begin{bmatrix} 0 & -\frac{\sigma_{ii}(x)}{\sigma_{jj}(\xi)} \\ -1 & 0 \end{bmatrix} \mathbf{k}_x = 0 \quad (\text{D.7})$$

so, B is defined as

$$B(x, \xi) := \begin{bmatrix} 0 & -\frac{\sigma_{ii}(x)}{\sigma_{jj}(\xi)} \\ -1 & 0 \end{bmatrix}. \quad (\text{D.8})$$

For this system, we want to change the dependent variables such that the p.d.e. system becomes decoupled. Using $\mathbf{u}(x, t) := \mathbf{w}(\mathbf{k}(x, t))$ [55, §11.3], the eigendecomposition of $B(x, \xi)$ is determined by considering the eigenvalue problem

$$B(x, \xi) \mathbf{r}^m(x, \xi) = \lambda^m(x, \xi) \mathbf{r}^m(x, \xi), \quad \text{for } m \in \{1, 2\} \quad (\text{D.9})$$

with characteristic polynomial

$$\det(B - \lambda^m I_{2 \times 2}) = \det \left(\begin{bmatrix} -\lambda^m & -\frac{\sigma_{ii}(x)}{\sigma_{jj}(\xi)} \\ -1 & -\lambda^m \end{bmatrix} \right) = (\lambda^m)^2 - \frac{\sigma_{ii}(x)}{\sigma_{jj}(\xi)} = 0 \quad (\text{D.10})$$

so that the eigenvalues

$$\lambda_1 = \lambda, \quad \lambda_2 = -\lambda \quad \text{with} \quad \lambda := \sqrt{\frac{\sigma_{ii}(x)}{\sigma_{jj}(\xi)}} \quad (\text{D.11})$$

correspond to the (right) eigenvectors

$$\mathbf{r}_1 = \begin{bmatrix} -\lambda \\ 1 \end{bmatrix}, \quad \mathbf{r}_2 = \begin{bmatrix} \lambda \\ 1 \end{bmatrix}. \quad (\text{D.12})$$

As such, the eigendecomposition of $B(x, \xi)$ becomes

$$B(x, \xi) = V(x, \xi) D(x, \xi) V^{-1}(x, \xi) \quad (\text{D.13})$$

with the eigenvector matrix V , its inverse V^{-1} and eigenvalue matrix D

$$V = \begin{bmatrix} -\lambda & \lambda \\ 1 & 1 \end{bmatrix}, \quad D = \begin{bmatrix} \lambda & 0 \\ 0 & -\lambda \end{bmatrix}, \quad V^{-1} = \frac{1}{2} \begin{bmatrix} -\frac{1}{\lambda} & 1 \\ \frac{1}{\lambda} & 1 \end{bmatrix}. \quad (\text{D.14})$$

The first-order p.d.e. system of (D.7) is now rephrased using a change of variables $\mathbf{l}(x, \xi) = V^{-1} \mathbf{k}(x, \xi)$, the partial derivatives of which are

$$\mathbf{l}_x = (V^{-1})_x \mathbf{k} + V^{-1} \mathbf{k}_x \rightarrow \mathbf{k}_x = -B^{-1} \mathbf{k}_\xi \quad (\text{D.15})$$

$$\mathbf{l}_\xi = (V^{-1})_\xi \mathbf{k} + V^{-1} \mathbf{k}_\xi \rightarrow \mathbf{k}_\xi = V \left(\mathbf{l}_\xi - (V^{-1})_\xi V \mathbf{l} \right) \quad (\text{D.16})$$

Using the eigendecomposition (D.13), the variable transformation can be completed since the eigenvectors of B and B^{-1} are equal such that:

$$\begin{aligned} \mathbf{l}_x &= (V^{-1})_x V \mathbf{l} - D \left(\mathbf{l}_\xi - (V^{-1})_\xi V \mathbf{l} \right) \\ &= -D \mathbf{l}_\xi + \left((V^{-1})_x + D (V^{-1})_\xi \right) V \mathbf{l}. \end{aligned} \quad (\text{D.17})$$

Now, we are interested in finding two solutions that are constant along a characteristic of the p.d.e. system. For existence of such a solution, the decomposed p.d.e. system of (D.17) can be simplified to

$$\mathbf{l}_\xi + D(x, \xi)\mathbf{l}_x = 0 \quad (\text{D.18})$$

where only the highest-order derivatives of $\mathbf{l}(x, \xi)$ remain. Thus, the two first-order hyperbolic p.d.e. to be solved are:

$$l_\xi^1 + \sqrt{\frac{\sigma_{ii}(x)}{\sigma_{jj}(\xi)}} l_x^1 = 0 \iff \sqrt{\sigma_{jj}(\xi)} l_\xi^1 + \sqrt{\sigma_{ii}(x)} l_x^1 = 0 \quad (\text{D.19})$$

$$l_\xi^2 - \sqrt{\frac{\sigma_{ii}(x)}{\sigma_{jj}(\xi)}} l_x^2 = 0 \iff \sqrt{\sigma_{jj}(\xi)} l_\xi^2 - \sqrt{\sigma_{ii}(x)} l_x^2 = 0 \quad (\text{D.20})$$

with the characteristic o.d.e. for \mathbf{l}^m being

$$\dot{\mathbf{p}}^m(s) = \begin{bmatrix} (-1)^m \frac{1}{2\sqrt{\sigma_{ii}(x)}} \\ \frac{1}{2\sqrt{\sigma_{jj}(\xi)}} \end{bmatrix}, \quad \dot{\mathbf{x}}^m(s) = \begin{bmatrix} (-1)^m \sqrt{\sigma_{ii}(x)} \\ \sqrt{\sigma_{jj}(\xi)} \end{bmatrix} \quad (\text{D.21})$$

for $m = \{1, 2\}$. So, there are two characteristic equations for each $k_{ij}(x, \xi)$, $1 \leq i, j \leq 3$. This implies that the number of boundary conditions should equal $2N$ for the N kernel functions. In § 4.2.1, we attempt to find a set of boundary conditions compliant to this requirement.

Appendix E

First-order kernel problem

This section transforms the kernel problem into a first-order system, because the set of boundary conditions found in § 4.2.1 cannot be used directly to solve the second-order kernel problem. The set of boundary conditions \mathcal{B}_1 constrain the second-order kernel p.d.e. (4.30), but contain undesired boundary conditions that are not compatible with most numerical approaches (e.g., MATLAB PDE toolbox). This is due to the inclusion of a so-called Cauchy-type boundary condition at $\delta\mathcal{T}_3 : (x, x)$ (4.45),

$$\begin{aligned} k_{ij}(x, x) &= 0 && \text{for } i < j, \\ \sigma_{ii}(x)k_x^{ij}(x, x) + k_\xi^{ij}(x, x)\sigma_{jj}(x) &= 0 \end{aligned} \quad (\text{E.1})$$

i.e., the function and its normal derivative are subject to a b.c. simultaneously.

This numerical issue is circumvented through the redefinition of the kernel problem to a first-order system. The first-order system contains an additional N states $l_{ij}(x, \xi)$, which constitute a combination of $k_{ij}(x, \xi)$ and $k_{x,\xi}^{ij}(x, \xi)$. The second-order kernel p.d.e. (4.30) can be translated into a first-order system through the definition of $L(x, \xi)$ containing the functions $l_{ij}(x, \xi)$ [78],

$$L(x, \xi) = \sqrt{\Sigma}(x)K_x(x, \xi) + K_\xi(x, \xi)\sqrt{\Sigma}(\xi) + F_1(x, \xi)K(x, \xi) + K(x, \xi)G_1(x, \xi), \quad (\text{E.2})$$

whose partial derivatives are computed as:

$$\begin{aligned} \sqrt{\Sigma}(x)L_x(x, \xi) - L_\xi(x, \xi)\sqrt{\Sigma}(\xi) \\ = \sqrt{\Sigma}(x)\left(\partial_x\left(\sqrt{\Sigma}(x)K_x\right) + K_{\xi x}\sqrt{\Sigma}(\xi) + F_{1,x}K + F_1K_x + K_xG_1 + KG_{1,x}\right) \\ - \left(\sqrt{\Sigma}(x)K_{x\xi} + \partial_\xi\left(K_\xi\sqrt{\Sigma}(\xi)\right) + F_{1,\xi}K + F_1K_\xi + K_\xi G_1 + KG_{1,\xi}\right)\sqrt{\Sigma}(\xi). \end{aligned} \quad (\text{E.3})$$

It can be seen that the cross-derivatives $K_{x\xi}$ drop out as desired, hence the minus sign at the left-hand side of (E.3). The second-order derivatives of the kernel p.d.e. are revealed using

$$\begin{aligned} \sqrt{\Sigma}(x)\partial_x\left(\sqrt{\Sigma}K_x\right) - \partial_\xi\left(K_\xi\sqrt{\Sigma}\right)\sqrt{\Sigma}(\xi) \\ = \sqrt{\Sigma}(x)\left(\frac{\Sigma_x(x)}{2\sqrt{\Sigma}(x)}K_x + \sqrt{\Sigma}(x)K_{xx}\right) - \left(K_{\xi\xi}\sqrt{\Sigma}(\xi) + K_\xi\frac{\Sigma_\xi(\xi)}{2\sqrt{\Sigma}(\xi)}\right)\sqrt{\Sigma}(\xi) \\ = \partial_x(\Sigma(x)K_x) - \partial_\xi(K_\xi\Sigma(\xi)) - \frac{\Sigma_x(x)}{2}K_x + K_\xi\frac{\Sigma_\xi(\xi)}{2}. \end{aligned} \quad (\text{E.4})$$

Also, we use the definition of $L(x, \xi)$ to compute $-FL$ and LG :

$$\begin{aligned} -F_1K_\xi\sqrt{\Sigma}(\xi) &= -F_1L + F_1\sqrt{\Sigma}(x)K_x + F_1KG_1 + F_1^2K, \\ \sqrt{\Sigma}(x)K_xG_1 &= LG_1 - K_\xi\sqrt{\Sigma}(\xi)G_1 - F_1KG_1 - KG_1^2, \end{aligned}$$

which, via substitution of the second-order kernel p.d.e. (4.30) into (E.4), then yields:

$$\begin{aligned} & \sqrt{\Sigma}(x)L_x(x, \xi) - L_\xi(x, \xi)\sqrt{\Sigma}(\xi) \\ &= K \left[\Lambda(\xi) - \Phi_\xi(\xi) - G_{1,\xi}\sqrt{\Sigma}(\xi) - G_1^2 \right] + \left[-\Theta(x) + \sqrt{\Sigma}(x)F_{1,x} + F_1^2 \right] K \\ &+ \left[-\Phi(x) - \frac{1}{2}\Sigma_x(x) + \sqrt{\Sigma}(x)F_1 + F_1\sqrt{\Sigma}(x) \right] K_x + K_\xi \left[-\Phi(\xi) + \frac{1}{2}\Sigma_\xi(\xi) - G_1\sqrt{\Sigma}(\xi) - \sqrt{\Sigma}(\xi)G_1 \right] \\ &+ \sqrt{\Sigma}(x)KG_{1,x} - F_{1,\xi}K\sqrt{\Sigma}(\xi) - F_1L + LG_1. \end{aligned} \quad (\text{E.5})$$

It is necessary that (E.5) depends on $K(x, \xi)$ and $L(x, \xi)$ only, since we aim to obtain a first-order p.d.e. system. This motivates the specification of $F_1(x)$ and $G_1(\xi)$ along the lines of [78], for the matrix arguments affecting K_x and K_ξ should be eliminated:

$$f_1^{ij}(x) := \begin{cases} \frac{\phi_{ij}(x)}{\sqrt{\sigma_{ii}}(x) + \sqrt{\sigma_{jj}}(x)} & \text{for } i \neq j \\ \frac{\sigma_x^{ii}(x) + 2\phi_{ii}(x)}{4\sqrt{\sigma_{ii}}(x)} & \text{for } i = j \end{cases}, \quad g_1^{ij}(\xi) := \begin{cases} \frac{-\phi_{ij}(\xi)}{\sqrt{\sigma_{ii}}(\xi) + \sqrt{\sigma_{jj}}(\xi)} & \text{for } i \neq j \\ \frac{\sigma_\xi^{ii}(\xi) - 2\phi_{ii}(\xi)}{4\sqrt{\sigma_{ii}}(\xi)} & \text{for } i = j \end{cases} \quad (\text{E.6})$$

As a result, $F_1(x)$ and $G_1(\xi)$ now only depend on a single space coordinate such that $F_{1,\xi}(x)$ and $G_{1,x}(\xi)$ vanish from (E.5). Using $F_1(x)$ and $G_1(\xi)$ (E.6), the second-order hyperbolic system can be rephrased into an equivalent one of first-order,

$$\begin{aligned} \sqrt{\Sigma}(x)K_x(x, \xi) + K_\xi(x, \xi)\sqrt{\Sigma}(\xi) &= L(x, \xi) - F_1(x)K(x, \xi) - K(x, \xi)G_1(\xi), \\ \sqrt{\Sigma}(x)L_x(x, \xi) - L_\xi(x, \xi)\sqrt{\Sigma}(\xi) &= K(x, \xi)G_2(\xi) + F_2(x)K(x, \xi) \\ &+ L(x, \xi)G_1(\xi) - F_1(x)L(x, \xi), \end{aligned} \quad (\text{E.7})$$

where we define $F_2(x)$ and $G_2(\xi)$ for brevity:

$$F_2(x) = -\Theta(x) + \sqrt{\Sigma}(x)F_{1,x}(x) + (F_1(x))^2, \quad (\text{E.8})$$

$$G_2(\xi) = \Lambda(\xi) - \Phi_\xi(\xi) - G_{1,\xi}(\xi)\sqrt{\Sigma}(\xi) - (G_1(\xi))^2. \quad (\text{E.9})$$

The set of boundary conditions \mathcal{B}_1 (4.45) can be translated to the first-order system, which for the domain boundary $\delta\mathcal{T}_1 : (x, 0)$ becomes:

$$\begin{aligned} l_{ij}(x, 0) &= \sqrt{\sigma_{ii}}(x)k_x^{ij}(x, 0) + k_\xi^{ij}(x, 0)\sqrt{\sigma_{jj}}(0) + \sum_{m=1}^3 (f_{1,im}(x)k_{mj}(x, 0) + k_{im}(x, 0)g_{1,mj}(0)) \\ &= \sqrt{\sigma_{ii}}(x)k_x^{ij}(x, 0) \\ &+ \sum_{m=1}^3 \left(f_1^{im}(x)k_{mj}(x, 0) + k_{im}(x, 0) \left(g_1^{mj}(0) \frac{\phi_{mj}(0) + \sigma_{mm}(0)e_{mj}}{\sqrt{\sigma_{jj}}(0)} \right) \right), \quad \text{for } i > j. \end{aligned} \quad (\text{E.10})$$

The Dirichlet-type b.c. at $\delta\mathcal{T}_3 : (x, x)$ remain equal, since $k_{ij}(x, x)$ is part of the state:

$$k_{ij}(x, x) = 0, \quad \text{for } i \neq j \quad (\text{E.11})$$

The Robin-type b.c. are readily simplified, however, for the first-order system includes the total derivative in $L(x, \xi)$, i.e.,

$$k_{ij}(x, x) = 0 \implies \frac{d}{dx}k_{ij}(x, x) = k_x^{ij}(x, x) + k_\xi^{ij}(x, x) = 0 \quad \text{for } i \neq j. \quad (\text{E.12})$$

Therefore, the partial derivatives can be rewritten for $i \neq j$ as

$$\begin{aligned}
 & \sqrt{\sigma_{ii}}(x)k_x^{ij}(x, x) + k_\xi^{ij}(x, x)\sqrt{\sigma_{jj}}(x) \\
 &= (\sqrt{\sigma_{ii}}(x) - \sqrt{\sigma_{jj}}(x))k_x^{ij}(x, x) \\
 &= \frac{\sigma_{ii}(x) - \sigma_{jj}(x)}{\sqrt{\sigma_{ii}}(x) + \sqrt{\sigma_{jj}}(x)}k_x^{ij}(x, x) \\
 &= -\frac{\phi_{ij}(x)}{\sqrt{\sigma_{ii}}(x) + \sqrt{\sigma_{jj}}(x)}(k_{jj}(x, x) - k_{ii}(x, x)) - \frac{\lambda_{ij}(x) - \theta_{ij}(x)}{\sqrt{\sigma_{ii}}(x) + \sqrt{\sigma_{jj}}(x)}, \tag{E.13}
 \end{aligned}$$

where in the final step we use the kernel condition \mathcal{K}_2 (4.44), for $i \neq j$:

$$(\sigma_{ii}(x) - \sigma_{jj}(x))k_x^{ij}(x, x) + \phi_{ij}(x)(k_{jj}(x, x) - k_{ii}(x, x)) + \lambda_{ij}(x) - \theta_{ij}(x) = 0.$$

Substituting (E.13) into $l_{ij}(x, x)$ and using the definitions $f_1^{ij}(x), g_1^{ij}(\xi)$ at (x, x) (E.6), it can be seen that:

$$\begin{aligned}
 l_{ij}(x, x) &= \sqrt{\sigma_{ii}}(x)k_x^{ij}(x, x) + k_\xi^{ij}(x, x)\sqrt{\sigma_{jj}}(x) + f_1^{ij}(x)k_{jj}(x, x) + k_{ii}(x, x)g_1^{ij}(x) \\
 &= \frac{\theta_{ij}(x) - \lambda_{ij}(x)}{\sqrt{\sigma_{ii}}(x) + \sqrt{\sigma_{jj}}(x)}, \quad \text{for } i \neq j, \tag{E.14}
 \end{aligned}$$

$$\begin{aligned}
 l_{ii}(x, x) &= \sqrt{\sigma_{ii}}(x)\frac{d}{dx}k_{ii}(x, x) + (f_1^{ii}(x) + g_1^{ii}(x))k_{ii}(x, x) \\
 &= -\frac{\sigma_x^{ii}(x)k_{ii}(x, x) + \lambda_{ii}(x) - \theta_{ii}(x)}{2\sqrt{\sigma_{ii}}(x)} + \left(\frac{\sigma_x^{ii}(x) + 2\phi_{ii}(x)}{4\sqrt{\sigma_{ii}}(x)} + \frac{\sigma_x^{ii}(x) - 2\phi_{ii}(x)}{4\sqrt{\sigma_{ii}}(x)}\right)k_{ii}(x, x) \\
 &= \frac{\theta_{ii}(x) - \lambda_{ii}(x)}{2\sqrt{\sigma_{ii}}(x)}, \quad \text{for } i = j. \tag{E.15}
 \end{aligned}$$

Counting the boundary conditions for the first-order system (E.7) amounts to a total number of $2N$ boundary conditions for N kernel functions $k_{ij}(x, \xi)$ and N functions $l_{ij}(x, \xi)$. The total set of boundary conditions, i.e., (E.10), (E.11), (E.14) and (E.15), is collectively defined by \mathcal{B}_2 . This concludes the transformation to the first-order system description, which is used to find the kernel solution in § 4.3.2.

Appendix F

Numerical implementation of kernel problem

The kernel problem is solved numerically using the approximation procedure found in § 4.3.1. The choice for the numerical approach is due to its coupled structure and spatial dependence. This section describes a numerical implementation of the problem to obtain a solution. We use the PDE toolbox of MATLAB, because it includes the ability to solve problems that may be time-dependent and involve spatially-varying coefficients. The toolbox handles problems in the following format,

$$\left(m \frac{\partial^2 \mathbf{z}}{\partial t^2} + d \frac{\partial \mathbf{z}}{\partial t} \right) - \nabla \cdot (b \nabla \mathbf{z}) + a \mathbf{z} = f, \quad (\text{F.1})$$

with the second-order tensor b , matrix a and vector f . The time-dependent terms between brackets in (F.1) are set to zero, i.e., $m = d = 0$, because the kernel problem is independent of time. The coefficients may depend on the coordinates (x, ξ) , but also the state (\mathbf{z}) and spatial derivatives (e.g., \mathbf{z}_x).

The kernel p.d.e. is a coupled linear system defined on the triangular domain \mathcal{T} , which is depicted in Figure 4.1 in § 4.1. The formulation of the boundary conditions is restricted to the generalized Dirichlet- and Neumann-format, respectively,

$$h_m \mathbf{z} = r_m, \quad (\text{F.2})$$

$$\mathbf{n}_m \cdot (b \nabla \mathbf{z}) + q_m \mathbf{z} = g_m, \quad (\text{F.3})$$

for $1 \leq m \leq 3$. The p.d.e. toolbox of MATLAB uses a right-hand coordinate system to define the (outward) normal vector $\mathbf{n}_m = (\cos(\alpha_m), \sin(\alpha_m))$ with rotation parameter α_m in radians. It should also be noted that by defining the geometry or domain, the associated edges and normal vectors are fixed automatically. So, the normal vectors are defined for each edge of the domain $\delta\mathcal{T}_m$ as

$$\mathbf{n}_1 = \mathbf{n}(3\pi/2) = -\mathbf{e}_\xi, \quad \mathbf{n}_2 = \mathbf{n}(0) = \mathbf{e}_x, \quad \mathbf{n}_3 = \mathbf{n}(3\pi/4) = -\frac{1}{\sqrt{2}}\mathbf{e}_x + \frac{1}{\sqrt{2}}\mathbf{e}_\xi. \quad (\text{F.4})$$

The conventions of the PDE toolbox are especially suitable for the (second-order) kernel p.d.e. set (4.30), which can be translated exactly into (F.1). The set of boundary conditions \mathcal{B}_1 are also compatible with the generalized b.c. formulations (F.2)–(F.3), which have been found by interpretation in § 4.2.1. However, an implementation problem arises from the set of Cauchy-type b.c. that specify $k_{ij}(x, x)$ and $(\dots)k_x^{ij}(x, x)$ for $i < j$. This problem can not be avoided by redefining the boundary conditions, because the total number of b.c. has been reduced already to the minimum¹.

¹An alternative set of b.c. $\{\mathcal{B}\} < 2N$, associated to a target system that can be proved stable, has not been found by the author, but may still exist.

The second-order kernel problem is transformed into an equivalent first-order problem in E, which effectively augments the state vector to include the partial derivatives therein. The first-order p.d.e. system (E.7) is formulated in the form $a(x, \xi)\mathbf{z}(x, \xi) = f(x, \xi, \mathbf{z}_x, \mathbf{z}_\xi)$,

$$\begin{bmatrix} -I \otimes F_1 - G_1^\top \otimes I & I \otimes I \\ G_2^\top \otimes I + I \otimes F_2 & G_1^\top \otimes I - I \otimes F_1 \end{bmatrix} \begin{bmatrix} \mathbf{k} \\ \mathbf{l} \end{bmatrix} = \begin{bmatrix} \left(I \otimes \sqrt{\Sigma}(x) \right) \mathbf{k}_x + \left(\sqrt{\Sigma}^\top(\xi) \otimes I \right) \mathbf{k}_\xi \\ \left(I \otimes \sqrt{\Sigma}(x) \right) \mathbf{l}_x - \left(\sqrt{\Sigma}^\top(\xi) \otimes I \right) \mathbf{l}_\xi \end{bmatrix} \quad (\text{F.5})$$

Hence, in (F.1), the coefficients are set to $m = d = 0$ and the (first-order) partial derivatives are included in the vector f . The matrix products are vectorized in $\mathbf{k}(x, \xi)$ and $\mathbf{l}(x, \xi)$ using the following operation, e.g., on $K(x, \xi)G_2(\xi)$,

$$\text{vec}(IK(x, \xi)G_2(\xi)) = (G_2^\top(\xi) \otimes I) \mathbf{k}(x, \xi), \quad (\text{F.6})$$

where the (column ordered) vectorizations of K and L are obtained by stacking their columns:

$$\mathbf{k}(x, \xi) := \text{vec}(K(x, \xi)) = [k_{11}(x, \xi), k_{21}(x, \xi), \dots, k_{23}(x, \xi), k_{33}(x, \xi)]^\top \quad (\text{F.7})$$

$$\mathbf{l}(x, \xi) := \text{vec}(L(x, \xi)) = [l_{11}(x, \xi), l_{21}(x, \xi), \dots, l_{23}(x, \xi), l_{33}(x, \xi)]^\top. \quad (\text{F.8})$$

The Kronecker product, denoted \otimes , in (F.6) results in a matrix $\{N^2 \times N^2\}$ with components g_2^{ij} of $G_2(\xi)$:

$$G_2^\top \otimes I = \begin{bmatrix} g_2^{11}(\xi)I & \cdots & g_2^{31}(\xi)I \\ \vdots & \ddots & \vdots \\ g_2^{13}(\xi)I & \cdots & g_2^{33}(\xi)I \end{bmatrix}. \quad (\text{F.9})$$

Now, the vectors \mathbf{k} and \mathbf{l} constitute the states of the problem that must be solved for. The set of boundary conditions for the first-order system (E.10), (E.11), (E.14) and (E.15) can be formulated in terms of the generalized b.c. (F.2)–(F.3) directly. The numerical solution obtained is used in § 4.3.2.

Bibliography

- [1] A. Baccoli et al. On the boundary control of coupled reaction-diffusion equations having the same diffusivity parameters. In *53rd IEEE Conference on Decision and Control*.
- [2] A. Baccoli et al. Boundary control of coupled reaction-diffusion processes with constant parameters. *Automatica*, 54:80–90, 2015.
- [3] A. Kallenbach. Integrated exhaust control with divertor parameter feedback and pellet ELM pacemaking in ASDEX Upgrade. *Journal of Nuclear Materials*, 337-339:732–736, 2005.
- [4] A. Winter et al. Towards the conceptual design of the ITER real-time plasma control system.
- [5] A.G. Peeters. Equations for the evolution of the radial electric field and poloidal rotation in toroidally symmetric geometry. *Physics of Plasmas*, 5(3):763–767, 1998.
- [6] A.M. Garofalo et al. Advances towards QH-mode viability for ELM-stable operation in ITER. *Nuclear Fusion*, 51:083018(1–10), 2011.
- [7] A.V. Chankin, G.M. McCracken. Loss ion orbits at the tokamak edge. *Nuclear Fusion*, 33(10):1459–1469, 1993.
- [8] B. Scott. Three-dimensional computation of drift Alfvén turbulence. *Plasma Physics and Controlled Fusion*, 39:1635–1668, 1997.
- [9] B.D. Scott. The nonlinear drift wave instability and its role in tokamak edge turbulence. *New Journal of Physics*, 4(52):1–30, 2002.
- [10] B.N. Rogers and J.F. Drake. Enhancement of Turbulence in Tokamaks by Magnetic Fluctuations. *Physical Review Letters*, 79(2):229–232, 1997.
- [11] C. Hidalgo et al. On the interplay between turbulence and plasma flows in tokamaks.
- [12] C.F. Maggi et al. Experimental study of H-L transitions in JET. In M. B. V. Naulin, C. Angioni, editor, *40th EPS Conference on Plasma Physics*.
- [13] C.F. Maggi et al. L-H threshold at low density and low momentum input in the JET tokamak. In *EPS Conference on Plasma Physics*, volume 38.
- [14] D. Moreau et al. Combined magnetic and kinetic control of advanced tokamak steady state scenarios based on semi-empirical modelling. *Nuclear Fusion*, 55(063011):1–13, 2015.
- [15] D. Veldman. Degenerate Bogdanov-Takens bifurcation in l-h transition plasma model. 2015.
- [16] D.M. Thomas et al. The back transition and hysteresis effects in DIII-D. *Plasma Physics and Controlled Fusion*, 40:707–712, 1998.
- [17] D.W. Scott and B.C. Maglich. Ionization and Neutralization Reaction Rates of Deuterium in the Princeton Thermonuclear Fusion Test Reactor Operating Regime. 1996.

- [18] E. Schuster and M. Krstic. Control of a non-linear PDE system arising from non-burning tokamak plasma transport dynamics. *International Journal of Control*, 76(11):1116–1124, 2003.
- [19] Editors of Progress in the ITER Physics Basis. Chapter 1: Overview and summary. *Nuclear Fusion*, 47:S1–S17, 2007.
- [20] E.J. Doyle et al. Chapter 2: Plasma confinement and transport. *Nuclear Fusion*, 47:S18–S127, 2007.
- [21] F. Felici. *Real-time control of tokamak plasmas: from control of physics to physics-based control*. Phd thesis no.5203, Ecole Polytechnique Federale de Lausanne (EPFL), CH-1015 Lausanne, Switzerland, October 2011.
- [22] F. Felici et al. Real-time physics-model-based simulation of the current density profile in tokamak plasmas. *Nuclear Fusion*, 51:083052(1–19), 2011.
- [23] F. Pesamosca. *A model for dynamical oscillations in magnetically confined fusion plasmas at the transition to high confinement*. Master thesis, Politecnico di Milano.
- [24] F. Wagner et al. First results from Neutral Beam heating of diverted ASDEX discharges. *Heating in Toroidal Plasmas*, 1:35–48, 1982.
- [25] G.S. Xu et al. First Evidence of the Role of Zonal Flows for the L-H Transition at Marginal Input Power in the EAST Tokamak. *Physical Review Letters*, 107(125001):1–5, 2011.
- [26] H. Urano et al. H-mode pedestal structure in the variation of toroidal rotation and toroidal field ripple in JT-60U. *Nuclear Fusion*, 47:706–713, 2007.
- [27] H. Weisen et al. Boundary ion temperatures and ion orbit losses in JET. *Nuclear Fusion*, 31(12):2247–2269, 1991.
- [28] H. Zohm et al. Dynamic behavior of the L-H transition. *Physical Review Letters*, 72(2):222–226, 1994.
- [29] H.K. Khalil. *Nonlinear Systems*. Pearson Education Limited.
- [30] J.A. Heikkinen, T.P. Kiviniemi, A.G. Peeters. Neoclassical Radial Current Balance in Tokamaks and Transition to H-Mode. *Physical Review Letters*, 84(3):487–490, 2000.
- [31] J.A. Villegas. *A port-Hamiltonian approach to distributed parameter systems*. PhD thesis, University of Twente.
- [32] J.C. de Valenca. Bifurcation theory of the L-H transition dynamics in tokamak plasmas. 2010.
- [33] J.D. Callen, A.J. Cole, C.C. Hegna. Toroidal Rotation In Tokamak Plasmas. In IAEA-CN-165, editor, *Geneva Fusion Energy Conference*.
- [34] J.D. Callen et al. Toroidal flow and radial particle flux in tokamak plasmas. *Physics of Plasmas*, 16(082504):1–18, 2009.
- [35] J.E. Kinsey. Time-dependent transport simulations of JET H-mode plasmas. In *IAEA Fusion Energy Conference*, volume 17.
- [36] J.G. Cordey et al. Evolution of transport through the L-H transition in JET. *Nuclear Fusion*, 35(5):505–520, 1995.
- [37] J.P. Freidberg. *Plasma and Fusion Physics*. Cambridge University Press.
- [38] J.W. Connor and H.R. Wilson. A review of theories of the L-H transition. *Plasma Physics and Controlled Fusion*, 42:R1–R74, 2000.

- [39] J.W. Hughes et al. Modification of H-mode pedestal structure with lower hybrid waves on Alcator C-Mod. *Nuclear Fusion*, 50:064001(1–7), 2010.
- [40] K. Ida. Experimental studies of the physical mechanism determining the radial electric field and its radial structure in a toroidal plasma. *Plasma Physics and Controlled Fusion*, 40:1429–1488, 1998.
- [41] K. Ida et al. Reduction of Ion Thermal Diffusivity Associated with the Transition of the Radial Electric Field in Neutral-Beam-Heated Plasmas in the Large Helical Device. *Physical Review Letters*, 86(23):5297–5300, 2001.
- [42] K. Itoh and S.-I. Itoh. The role of the electric field in confinement. *Plasma Physics and Controlled Fusion*, 38:1–49, 1996.
- [43] K. Itoh and S.-I. Itoh. A structural bifurcation of transport in toroidal plasmas. *Plasma Physics and Controlled Fusion*, 58(045017):1–7, 2016.
- [44] K. Itoh et al. Effect of the loss cone on confinement in toroidal helical devices. *Nuclear Fusion*, 29(11):1851–1861, 1989.
- [45] K. Itoh et al. Solitary radial electric field structure in tokamak plasmas. *Physics of Plasmas*, 5(12):4121–4123, 1998.
- [46] K. Kamiya et al. Modifications to the edge radial electric field by angular momentum injection in jt-60u and their implication for pedestal transport. *Nuclear Fusion*, 52:114010(1–12), 2012.
- [47] K. Miki et al. Spatio-temporal evolution of the L-I-H transition. *Physics of Plasmas*, 19(9):092306(1–10), 2012.
- [48] K. Miki et al. Dynamics of stimulated L-H transitions. *Physics of Plasmas*, 20(082304):1–11, 2013.
- [49] K. Miki et al. Physics of stimulated L-H Transition. *Physical Review Letters*, 110(195002):1–5, 2013.
- [50] K. Miyamoto. Direct ion orbit loss near the plasma edge of a divertor tokamak in the presence of a radial electric field. *Nuclear Fusion*, 36(7):927–938, 1996.
- [51] K.A. Morris. What is hysteresis? *Applied Mechanics Reviews*, 64(5):050801, 2011.
- [52] K.C. Shaing, E.C. Crume, Jr. Bifurcation Theory of Poloidal Rotation in Tokamaks: A Model for the L-H Transition. *Physical Review Letters*, 63(21):2369–2372, 1989.
- [53] K.C. Shaing et al. Bifurcation of poloidal rotation and suppression of turbulent fluctuations: A model for the L-H transition in tokamaks. *Physics of Fluids B*, 2(6):1492–1498, 1990.
- [54] K.H. Burrel et al. Edge pedestal control in quiescent H-mode discharges in DIII-D using co- plus counter-neutral beam injection. *Nuclear Fusion*, 49:085024(1–9), 2009.
- [55] L.C. Evans. *Partial Differential Equations*. AMS.
- [56] L.M. Kovrizhnykh. Neoclassical theory of transport processes in toroidal magnetic confinement systems, with emphasis on non-axisymmetric configurations. *Nuclear Fusion*, 24(7):851–936, 1984.
- [57] M. Krstic and A. Smyshlyaev. *Boundary Control of PDEs: A Course on Backstepping Design*. Society for Industrial and Applied Mathematics.
- [58] M. Kubic. Review of plasma parameters of the JET tokamak in various regimes of its operation. 2007.

- [59] M. Leconte et al. Control of Edge Transport Barrier relaxations using Resonant Magnetic Perturbations. *AIP Conference Proceedings*, 993(35):35–38, 2008.
- [60] M. Leconte, P.H. Diamond, Y. Xu. Impact of resonant magnetic perturbations on zonal modes, drift-wave turbulence and the L-H transition threshold. *Nuclear Fusion*, 54(013004):1–12, 2014.
- [61] M.A. Malkov and P.H. Diamond. Weak hysteresis in a simplified model of the L-H transition. *Physics of Plasmas*, 16(012504):1–10, 2009.
- [62] M.A. Malkov et al. Linking the micro and macro: L-H transition dynamics and threshold physics. *Physics of Plasmas*, 22(032506):1–12, 2015.
- [63] M.D. Boyer and E. Schuster. Backstepping Control of Density and Energy Profiles in a Burning Tokamak Plasma. In *50th IEEE Conference on Decision and Control and European Control Conference*.
- [64] N. Kasuya, K. Itoh and Y. Takase. Effect of electrode biasing on the radial electric field structure bifurcation in tokamak plasmas. *Nuclear Fusion*, 43:244–249, 2003.
- [65] P. Gohil. Edge transport barriers in magnetic fusion plasmas. *C.R. Physique*, 7:606–621, 2006.
- [66] P. Gohil, K.H. Burrell and T.N. Carlstrom. Parametric dependence of the edge radial electric field in the DIII-D tokamak. *Nuclear Fusion*, 38(1):93–102, 1998.
- [67] P. Klaywittaphat, R. Picha, T. Onjun. Study of L-H Transition Triggered by Pellet Injection Based on a Power Threshold Model. *Plasma Physics Reports*, 40(10):790–796, 2014.
- [68] P.C. de Vries et al. Effect of toroidal field ripple on plasma rotation in JET. *Nuclear Fusion*, 48(035007):1–6, 2008.
- [69] P.C. Parks. A. M. Lyapunov stability theory 100 years on. *IMA Journal of Mathematical Control and Information*, 9:275–303, 1992.
- [70] P.H. Diamond et al. Self-Regulating Shear Flow Turbulence: A Paradigm for the L to H transition. *Physical Review Letters*, 72(16):2565–2568, 1994.
- [71] P.H. Diamond et al. Secondary instability in drift wave turbulence as a mechanism for zonal flow and avalanche formation. *Nuclear Fusion*, 41(8):1067–1080, 2001.
- [72] P.H. Diamond et al. Zonal flows in plasma - a review. *Plasma Physics and Controlled Fusion*, 47:R35–R161, 2005.
- [73] P.H. Diamond, Y.-B. Kim. Theory of mean poloidal flow generation by turbulence. *Physics of Fluids B*, 3(7):1626–1633, 1991.
- [74] P.J. Catto, A.N. Simakov. A new, explicitly collisional contribution to the gyroviscosity and the radial electric field in a collisional tokamak. *Physics of Plasmas*, 12(114503):1–4, 2005.
- [75] P.T. Lang et al. ELM Control at the L-H Transition Achieved by Pellet Pacing in the All-Metal Wall Tokamaks ASDEX Upgrade and JET. *EFDA-JET*, CP(14)03(03):1–5, 2014.
- [76] P.W. Terry. Suppression of turbulence and transport by sheared flow. *Reviews of Modern Physics*, 72(1):109–165, 2000.
- [77] R. Ball. Suppression of turbulence at low power input in a model for plasma confinement transitions. *Physics of Plasmas*, 12(090904):1–8, 2005.
- [78] R. Vazquez and M. Krstic. Boundary Control of Coupled Reaction-Advection-Diffusion Systems with Spatially-Varying Coefficients. *IEEE Transactions on Automatic Control*, 2016.

- [79] R. Vazquez and M. Krstic. Boundary control of coupled reaction-diffusion systems with spatially-varying reaction. *IFAC*, 49(8):222–227, 2016.
- [80] R.M. McDermott et al. Edge radial electric field structure and its connections to H-mode confinement in Alcator C-Mod plasmas. *Physics of Plasmas*, 16(5), 2009.
- [81] R.W. van Gils. *Feedback stabilisation of pool-boiling systems*. PhD thesis, University of Technology Eindhoven.
- [82] S.-H. Hahn et al. L-H Transitions Triggered by SMBI: Experiment and Theory. In *25th IAEA Fusion Energy Conference*.
- [83] S.-I. Itoh, K. Itoh and A. Fukuyama. The ELM My H mode as a limit cycle and the transient responses of H modes in tokamaks. *Nuclear Fusion*, 33(10):1445–1457, 1993.
- [84] S. Inoue et al. Anomalous ion loss due to low-frequency instabilities. *Nuclear Fusion*, 19(9):1252–1255, 1979.
- [85] S. Paquay. Studying bifurcations in proposed L-H transition models using Bifurcator. Master’s thesis, University of Technology Eindhoven.
- [86] S. Toda et al. Double hysteresis in L/H transition and compound dithers. *Plasma Physics and Controlled Fusion*, 38:1337–1341, 1996.
- [87] S. Toda et al. A theoretical model of H-mode transition triggered by condensed neutrals near X-point. *Plasma Physics and Controlled Fusion*, 39:301–312, 1997.
- [88] S.B. Korsholm et al. Reynolds stress and shear flow generation. *Plasma Physics and Controlled Fusion*, 42:1377–1395, 2001.
- [89] S.I. Itoh and K. Itoh. Model of L- to H-mode transition in tokamak. *Physical Review Letters*, 60(22):2276–2279, 1988.
- [90] T. Kiviniemi. *Numerical Simulations of Neoclassical Currents, Parallel Viscosity, and Radial Current Balance in Tokamak Plasmas*. PhD dissertation, Helsinki University of Technology.
- [91] T. Kobayashi et al. Experimental identification of electric field excitation mechanisms in a structural transition of tokamak plasmas. *Scientific Reports*, 6(30720):1–7, 2016.
- [92] T.C. Hender et al. Chapter 3: MHD stability, operational limits and disruptions. *Nuclear Fusion*, 47:S128–S202, 2007.
- [93] T.E. Stringer. Non-ambipolar neoclassical transport. *Nuclear Fusion*, 35(8):1008–1011, 1995.
- [94] T.P. Kiviniemi, J.A. Heikinen, A.G. Peeters. Test particle simulation of non-ambipolar ion diffusion in tokamaks. *Nuclear Fusion*, 40(9):1587–1596, 2000.
- [95] T.S. Hahm. Rotation shear induced fluctuation decorrelation in a toroidal plasma. *Physics of Plasmas*, 1:2940–2944, 1994.
- [96] W. Fundamenski. Scrape-off layer transport on JET. *Fusion Science and Technology*, 53, 2007.
- [97] W. Fundamenski et al. A new model of the L-H transition in tokamaks. *Nuclear Fusion*, 52(062003):1–8, 2012.
- [98] W. Guojiang, Z. Xiaodong. Calculations of the Ion Orbit Loss Region at the Plasma Edge of EAST. *Plasma Science and Technology*, 14(9):789–793, 2012.
- [99] W. Weymiens. *Bifurcation theory of the L-H transition in fusion plasmas*. PhD thesis, University of Technology Eindhoven.

BIBLIOGRAPHY

- [100] W. Weymiens et al. Bifurcation theory for the l-h transition in magnetically confined fusion plasmas. *Physics of Plasmas*, 19:072309(1–10), 2012.
- [101] W. Weymiens et al. Comparison of bifurcation dynamics of turbulent transport models for the L-H transition. *Physics of Plasmas*, 21:052302(1–10), 2014.
- [102] X. Garbet. Turbulence in fusion plasmas: key issues and impact on transport modelling. *Plasma Physics and Controlled Fusion*, 43:A251–A266, 2001.
- [103] Y. Andrew. Evolution of the radial electric field in a JET H-mode plasma. *Europhysics Letters*, 83(15003):1–6, 2008.
- [104] Y. Gribov et al. Chapter 8: Plasma operation and control. *Nuclear Fusion*, 47:S385–S403, 2007.
- [105] Z. Yan et al. Observation of the L-H Confinement Bifurcation Triggered by a Turbulence-Driven Shear Flow in a Tokamak Plasma. *Physical Review Letters*, 112(125002):1–5, 2014.